# Developing Transparent Polycrystalline Zinc Selenide (ZnSe) Pellets for Laser Applications

by

Sefa Öztulum

A Dissertation Submitted to the
Graduate School of Sciences and Engineering
in Partial Fulfillment of the Requirements for
the Degree of

Master of Science

in

Materials Science and Engineering


January 20, 2022

# Developing Transparent Polycrystalline Zinc Selenide (ZnSe) Pellets for Laser Applications

Koç University

Graduate School of Sciences and Engineering

This is to certify that I have examined this copy of a master's thesis by

**Sefa Öztulum**

and have found that it is complete and satisfactory in all respects,
and that any and all revisions required by the final
examining committee have been made.

Committee Members:

Asst. Prof. Umut Aydemir

Prof. Alphan Sennaroğlu

Prof. Hâldun Sevinçli

Date: 20.01.2022

*To my precious family Elif, İbrahim, Sena*

# ABSTRACT

**Developing Transparent Polycrystalline Zinc Selenide (ZnSe) Pellets for Laser Applications**

**Sefa Öztulum**

**Master of Science in Materials Science and Engineering**

**January 20, 2022**

Transparency in particular regions of the electromagnetic spectrum is well recognized and is utilized in many applications, including solid-state lasers, optical windows in optical spectroscopy instruments, and transparent armors. Improving the quality of transparency, mechanical endurance, thermal stability, and corrosion resistance in this material class has attracted academic and industrial interest.

Nowadays, numerous transparent ceramics are available in various compositions employed in different applications due to their physical, chemical, and optical characteristics. Among many functional transparent ceramics, ZnSe, in particular, exhibits a number of unique properties: (i) it does not oxidize at temperatures up to 300 °C in the ambient atmosphere, (ii) its refractive index doesn't vary to a large extent with temperature, (iii) it exhibits homogeneity in refractive index at different wavelengths, (iv) it is non-toxic, (v) it has low phonon energy, (vi) it exhibits isotropic properties because of its cubic crystal structure, and (vii) it exhibits transparency in a broad range of the electromagnetic spectrum (0.6–21μm). ZnSe is widely chosen as a host material for lasers that operate in a broad spectrum, particularly in the mid-infrared range.

Until now, the polycrystalline ZnSe materials having the highest light transmittance have been synthesized using chemical vapor deposition. However, this approach needs the use of very hazardous gases such as $H_2Se$ and has a relatively slow crystal growth rate and is an expensive process. Therefore, new synthesis methods should be developed to produce transparent ZnSe materials.

In this thesis, polycrystalline ZnSe materials have been prepared via solid-state synthesis, co-precipitation, and mechanical alloying (high-energy ball milling) methods. Furthermore, single-crystalline ZnSe was obtained via the chemical vapor transport method. The polycrystalline ZnSe materials synthesized by one of the aforementioned methods have been consolidated using the spark plasma sintering (SPS) process with a variety of sintering parameters. Chemical, structural, and optical analyses have been performed on all as-obtained ZnSe pellets. According to the characterization results, the formation of a trace amount of impurity in the powder material to be sintered, a broad particle size distribution, and small crystallite sizes considerably lower the optical transmittance of the ZnSe pellets obtained by SPS. Additionally, carbon diffusion to the sintered material has been detected from the graphite die after SPS process, evidenced by the material's black/gray color. By optimizing the SPS parameters, it has been possible to hinder carbon contamination of the material to be sintered. Besides, by applying a purification step (heat treatment either under Argon or vacuum atmosphere) for the powder to be sintered and by tuning the SPS parameters, pellets with large grain size and less porous structure have been obtained. In this way, the transparency of the pellets has been largely improved. The best sintered ZnSe sample has been obtained by using the ZnSe powder prepared by the solid-state method for 150 minutes at 1200 °C.

This sample provided a light transmittance of around 50% in the far-infrared range. To the best of our knowledge, to synthesize single-crystalline ZnSe materials, $ZnCl_2$ was used as a transport agent for the first time in this thesis. Single-crystalline ZnSe synthesis up to 2 mm in length has been accomplished using this method in trials conducted under various heat gradients and with varying concentrations of transport agents.

# ÖZETÇE


**Lazer Uygulamaları İçin Şeffaf Polikristal Formunda Çinko Selenit (ZnSe) Peletlerin Geliştirilmesi**

**Sefa Öztulum**

**Malzeme Bilimleri ve Mühendisliği, Yüksek Lisans**

**20 Ocak 2022**

Bilindiği üzere bir malzemenin elektromanyetik spektrumun belirli bölgelerinde şeffaf özellik göstermesi onun, lazerler, optik spektroskopi cihazları içersinde yer alan optik pencereler, daha çok askeri sanayide kullanılan şeffaf zırhlar gibi birçok konuda akla gelen ilk malzeme olmasına sebep olmaktadır. Kendisine oldukça geniş bir alanda kullanım imkanı bulma potensiyeli taşıyan şeffaflık özelliği ile seramiklerin mekanik dayanıklılığı, yüksek sıcaklık altındaki kararlılığı, korozyona karşı yüksek dirençli olmaları gibi özelliklerini bir araya getirme düşüncesi, hem akademinin hem de özel sektörün şeffaf seramiklere olan ilgisini oldukça artırmaktadır.

Günümüzde farklı kompozisyonlarda birçok şeffaf seramiğin üretimi mümkündür ve herbiri sahip oldukları fiziksel, kimyasal ve optik özelliklerine göre oldukça geniş bir yelpazede hali hazırda kullanılmaktadır. Bahsi geçen şeffaf seramikler arasında özellikle ZnSe kendine has bazı avantajlara sahiptir. Atmosfer ortamında 300 °C sıcaklığa kadar oksitlenmemesi, kırılma indisinin sıcaklığa bağlı değişiminin az olması, değişen dalga boylarında kırılma indisindeki homojenite, toksik olmaması, düşük fonon enerjisine sahip bir kristal olması, kübik kristal yapıda olması sebebi ile izotropik özellikler göstermesi ve elektromanyetik spekturumun geniş bir aralığında (0.6–21μm) şeffaf olması ile birçok şeffaf seramiğe karşı üstünlük kurmaktadır. Bahsi geçen avantajların hemen hepsi şeffaf ZnSe seramiklerinin lazer kristalleri olarak kullanılmasında büyük teşvik kaynağıdır. Özellikle orta-kızılaltı bölgede, farklı rejimlerde çalışabilen lazerlerde konak malzeme olarak sıkça ZnSe tercih edilmektedir.

Şimdiye kadar ışık geçirgenliği en yüksek polikristal ZnSe malzemeleri kimyasal buhar biriktirme yöntemi ile üretilmiştir. Fakat bu yöntemin $H_2S$, $H_2Se$ gibi çevre için oldukça toksik gazlar kullanılmasını zorunlu kılması, görece düşük kristal büyütme hızına sahip olması ve üretim sürecinin pahalı olması, şeffaf ZnSe malzemesinin üretiminde yeni yöntemlerin arayışının arkasında yatan en önemli nedenlerdir.

Bu tezde katı hal sentezi yöntemi, birlikte çöktürme yöntemi ve mekanik alaşımlama yöntemi kullanılarak elde edilen toz formdaki polikristal ZnSe malzemesinin ve kimyasal buhar taşınımı yöntemi kullanılarak elde edilen tek kristal ZnSe malzemelerinin kimyasal ve mikro yapısal analizleri yapılmıştır. Elde edilen toz polikristal ZnSe malzemeleri farklı sinterleme parametreleri kullanılarak kıvılcım plazma sinterleme yöntemi ile preslenmiştir. Bu işlem sonucunda elde edilen dairesel formda katı ZnSe malzemelerinin kimyasal, yapısal ve optik analizleri yapılmıştır. Yapılan analizlere göre sinterlenecek toz malzemenin içersindeki en küçük safsızlığın, geniş bir aralıkta parçacık boyutu dağılımına sahip olmasının ve küçük kristal boyutlarından meydan gelmesinin sinterleme sonucunda elde edilen ZnSe malzemesinin optik geçirgenliğini önemli miktarda azalttığı belirlenmiştir. Ayrıca kıvılcım plazma sinterleme metodunda kullanılan grafit kalıptan malzemeye karbon geçişi saptanmış ve

malzemedeki karbon safsızlığının malzemenin renginin siyah tonlarında olmasına ışık geçirgenliğin azalmasına sebep olduğu belirlenmiştir. Malzemenin karbon ile kontamine olmaması ve sinterlenen malzemenin büyük kristal boyutlarında ve daha az porlu yapıya sahip olması Ar veya vakum ortamında saflaştırma (ısıl işlem) uygulanarak ve kıvılcım plasma sinterleme parametreleri optimize edilerek sağlanmıştır. En iyi örnek katı hal yöntemi ile sentezlenen toz ZnSe malzemesinin 1200 °C sıcaklıkta 150 dk sinterlenmesi ile elde edilmiştir. Bu örnekler uzak kızıl ötesi bölgelerde yaklaşık %50 ışık geçirgenliğine ulaşabilmektedir. Kimyasal buhar taşınımı yöntemi ile tek kristal ZnSe sentezinde ise bilindiği kadarıyla $ZnCl_2$ ilk kez transfer ajanı olarak kullanılmıştır. Bu yöntem ile farklı ısı gradyantları altında ve farklı miktarlarda taşıma ajanı kullanılarak yapılan deneylerde 2 mm boyuna ulaşabilen tek kristal ZnSe sentezi başarıyla gerçekleştirilmiştir.

# ACKNOWLEDGMENTS

First and foremost, I want to express my gratitude to Asst. Prof. Dr. Umut Aydemir, my advisor, for all of his support, mentorship, and encouragement during my MSc studies. I am honored to be a part of Dr. Aydemir's research team.

Thanks to the Scientific and Technological Council of Turkey (TUBITAK) (Project Number: 120F324) for the financial assistance in carrying out this study. I thank Koç University Boron and Advanced Materials Application and Research Center (KUBAM) for supporting this research. Thanks to Koç University Surface Science and Technology Center (KUYTAM) and Koç University TÜPRAŞ Energy Center (KUTEM), and Max Planck Institute for Chemical Physics of Solids (MPI-CPfS) for enabling me to use their research facilities.

I want to express my sincere thanks to my thesis committee members Prof. Dr. Alphan Sennaroğlu and Prof. Dr. Hâldun Sevinçli. My special thanks go to Prof. Dr. Alphan Sennaroğlu for encouraging my interest in lasers and ultraviolet-visible spectroscopy measurements. I would like to thank Assoc. Prof. Dr. Alper Uzun for Fourier-transform infrared spectroscopy measurements. Special thanks to Assoc. Prof. Dr. Uğur Ünal, as his door was always open for any kind of query. Special thanks go to Dr. Barış Yağcı for providing help in SEM/EDX measurements and for being always motivating and joyful. I would like to thank Dr. Yurii Prots and Dr. Ulrich Burkhardt from MPI-CPfS for WDXS and EDX measurements.

I'd want to thank all my group members, with whom I was delighted to work at KUBAM, for creating a pleasant and enjoyable work environment and helping me become acquainted with the laboratory equipment. Special thanks to Müjde Yahyaoğlu, Kıvanç Sağlık, Büşra Mete, Kamil Kiraz, and Samet Aydın for their support in lab and for their friendship. Thanks to Minahil Khan for her support in UV-vis measurements and to Samira F. Kurtoğlu-Öztulum, Özce Durak, and Ezgi Demiröz for providing help in measurements in KUTEM.

I want to thank my parents, Elif and İbrahim Öztulum, and my sister Sena for their unlimited encouragement and unflagging love. I also want to thank Beatrice and Ertuğrul Kurtoğlu for their constant support and motivation. I am really fortunate to have a wonderful family.

I am eternally grateful to Samira, my closest friend, favorative human being, and wife, who has been at my side for most of my life

# TABLE OF CONTENTS

# LIST OF TABLES

# LIST OF FIGURES

# ABBREVIATIONS

| | |
|---|---|
| CVD | Chemical Vapor Deposition |
| PVT | Physical Vapor Deposition |
| HP | Hot Press |
| HIP | Hot Isostatic Press |
| SPS | Spark Plasma Sintering |
| LIDAR | Light Detection and Ranging |
| ZS | Zinc Shot |
| ZP | Zinc Powder |
| SS | Selenium Shot |
| SP | Selenium Powder |
| SPoZ | Small Pieces of Zinc |
| MoB | Mass of Balls |
| MoR | Mass of Reactants |
| WDXS | Wavelength-Dispersive X-Ray Spectroscopy |
| SEM | Scanning Electron Microscopy |
| EDX | Energy Dispersive X-Ray |
| FTIR | Fourier Transform Infrared Spectroscopy |
| XPS | X-Ray Photoelectron Spectroscopy |
| MoTA | Mass of Transport Agent |
| VoQ | Volume of Quartz Tube |

# Chapter 1:
# INTRODUCTION

Transparent materials are a rapidly developing class of materials because they have a wide range of utilization. Some of these usage areas, which vary according to which wavelengths are transmitted and the mechanical and chemical properties of the material, are computers, electronic devices that perform signal transmission and processing, radar systems, and lasers. It should be noted that what makes all these applications possible is the transmission of light through the material.

## *1.1 Mechanism Behind Transparency*

For a material to be transparent, light should be able to pass through the material without being absorbed or scattered as it travels through the material. When light interacts with any medium, it can undergo a number of changes along its path, resulting in a variety of optical phenomena. These optical phenomena are guided by the medium's electronic structure, surface properties, and microstructure.

The factors affecting the transparency of the material can be grouped under five main headings, these are reflection, refraction, absorption, luminescence, and scattering as shown in Figure 1.1 [1, 2].

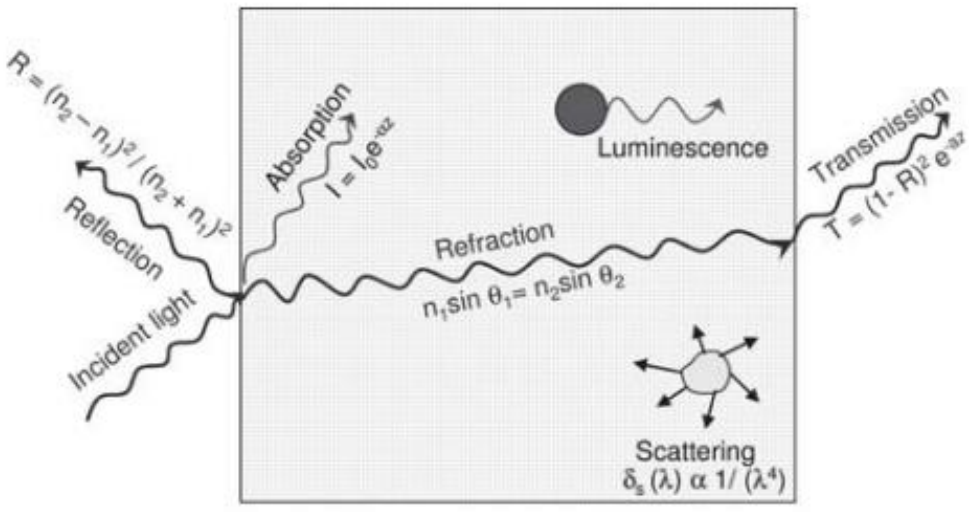


**Figure 1. 1.** Five phenomena affecting the transparency of a material [1].

Depending on the material's electronic properties and surface morphology, light is reflected from the surface. In this case, the number of photons that will transmit through the material changes.

Absorption takes place during transmission if the light's frequency matches the atoms' transition frequencies in the materials. The light beam will be weakened as it progresses in the matrix of material in this situation. Thus, the medium's transmission is clearly tied to its absorption. The coloring of many optical materials is caused by selective absorption.

This spontaneous emission of light occurs when excited atoms in a solid state material spontaneously emit light. Light absorption is one method of promoting atoms into excited states before they spontaneously emit energy. As a result, light propagation through an absorbent medium can be accompanied by luminescence.

Refraction has no effect on the light wave's intensity as it propagates. However, it can cause electromagnetic waves to propagate at a slower rate than they would in free space, resulting in the bending of light beams at surfaces. This phenomenon is explained by the well-known refraction law known as Snell's law.

In the scattering phenomenon in the material, the number of photons does not change, but the frequency and direction of the light might change. If the wavelength of the scatter beam does not change, if elastic scattering does, it is called inelastic scattering. The scattering phenomenon has an attenuating effect on transmittance of a material [1, 2].

How transparent a material will be is related to the factors mentioned above. The material becomes opaque or translucent when the light cannot penetrate the material.

## *1.2 A Brief Overview of Transparent Ceramics*

Optical ceramics research began in the 1950s. Coble R.L. proved for the first time that polycrystalline ceramics may be sintered to a visibly transparent/translucent state by fabricating a translucent alumina ceramics [3, 4]. Since then, a number of transparent/translucent oxide ceramics including MgO, $Y_2O$, $MgAl_2O$, Lanthanum Zirconate Titanate (PLZT), and Yttrium Aluminium Garnet (YAG) have been effectively made by sintering to high densities and therefore reducing/eliminating light scattering from residual porosity [5-8]. Simultaneously, numerous non-oxide optical

ceramics were produced, including fluoride ceramic $CaF_2$ [9], oxynitrogen ceramic AlON [9], nitride ceramic AlN [10], sulfide ceramic ZnS [11], and ceramic ZnSe [12]. ZnSe crystals are cubic and have a very wide transmittance range when compared to other cubic transparent ceramics. Table 1.1 lists some of the other materials in cubic structure with wide transmission range.

**Table 1. 1** Some transparent cubic structured materials.

| Cubic material | Transmission range (μm) |
|---|---|
| AgBr | 0.49–35 |
| AgCl | 0.42–28 |
| $BaF_2$ | 0.14–13 |
| $CaF_2$ | 0.12–10 |
| CsCl | 0.19–30 |
| GaAs | 0.9–17.3 |
| GaSb | 1.7–20 |
| KBr | 0.20–306 |
| KCl | 0.18–25 |
| NaI | 0.26–24 |
| MgO | 0.16–9 |
| PbS | 3–7 |
| CuCl | 0.4–19 |
| ZnSe | 0.5–20 |

There are many factors that determine which application areas the cubic crystals given in Table 1.1 are suitable for. Some of these are air sensitivity, mechanical properties, moisture sensitivities, toxicity and optical properties other than transmission. Considering all these factors, it can be inferred that ZnSe has advantages over most other crystals listed in Table 1.1 for infrared optical applications.

## *1.3 Infrared Region and Some Application Areas*

All of the materials listed in Table 1.1 are transparent in the infrared region. These materials can be named as infrared optical materials. As it is known, the infrared region refers to the region on the electromagnetic spectrum between the microwaves and the visible regions. Figure 1.2 shows the electromagnetic spectrum according to the wavelengths [13].

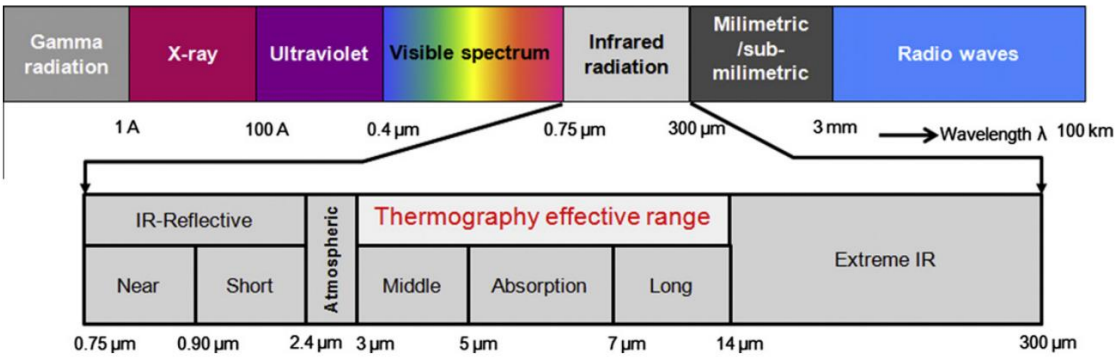


**Figure 1. 2** Infrared region in electromagnetic spectrum [13].

ZnSe windows have high transmission values for electromagnetic waves with wavelengths between 0.5 µm and 20 µm. A very large part of this range falls into the infrared region. This is the reason why materials with high transmission values in similar ranges are listed in Table 1.1. All of the aforementioned materials can be qualified in the class of infrared optical materials and they find a place for themselves in many infrared application areas. Some of these are infrared heating, diagnosis in medicine and imaging.

### *1.3.1 Infrared Heating*

Infrared heating is a way of heating a material without contact, noiselessly, and with high efficiency in short periods. The basic principle here is to convert the electric energy to electromagnetic waves in the infrared region. When this obtained radiation is coming in contact with a substance, some of the energy of the infrared light is absorbed by the molecules of the substance. Thus, the temperature of the substance is increased by the infrared light. Infrared heaters are widely used in the chemical industry, paint

industry, automobile industry and food industry. The important point here is that the bond energies of the molecules to be heated are suitable for absorbing infrared light. Table 1.2 provides the wavelengths absorbed by various molecules such as lipids, proteins, or sugars [14]. For example, when a food is exposed to a broad spectrum of infrared light, the region between 3.25 μm and 3.7 μm wavelengths is absorbed by ester bonds in lipids.

**Table 1. 2** Absorption ranges of the food compenents [14].

| Relevant Food Component | Absorption Wavelength (μm) | Chemical Group |
|---|---|---|
| Water, sugars | 2.7–3.3 | Hydroxyl group (O–H) |
| Lipids, sugars, proteins | 3.25–3.7 | Aliphatic carbon-hydrogen bond |
| Lipids | 5.71–5.76 | Carbonyl group (C=O) (ester) |
| Proteins | 5.92 | Carbonyl group (C=O) (amide) |
| Proteins | 2.83–3.33 | Nitrogen-hydrogen group (–NH–) |
| Unsaturated lipids | 4.44–4.76 | Carbon-carbon double bond (C=O) |

### *1.3.2 Diagnosis in Medicine*

Thermal changes are observed in areas of the human body where there are inflammations, abnormalities in blood flow, superficial or shallow tumors or intra-body biochemical reactions. Rapid detection of these zones of temperature change is critical for diagnosis. In these instances, infrared thermography can be highly effective [15, 16]. In particular, the use of thermographs in the diagnosis of breast cancers has become widespread. In Figure 1.3, it is shown after biopsy that the areas where temperature increase is observed are tumors.

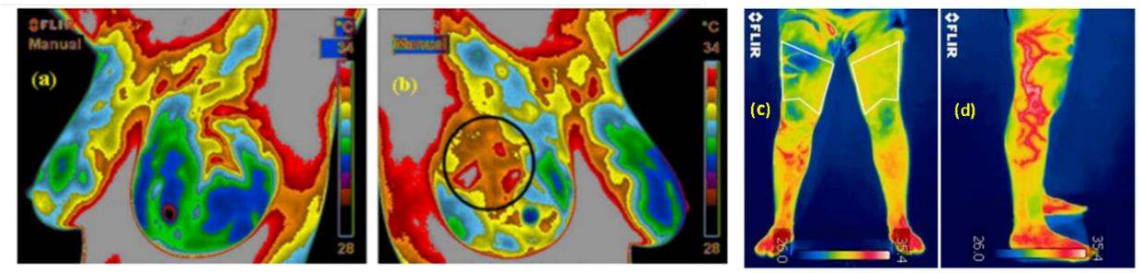


**Figure 1. 3** Data collection of (a) left breast, (b) right breast, (c) injured region of interest (right leg), (d) uninjured region of interest (left leg) [15, 16].

### *1.3.3 Thermal Imaging*

As is well known, every object with a temperature greater than 0 K emits radiation at a variety of intensities throughout a broad range. As illustrated in Figure 1.4, as the temperature decreases, the wavelength corresponding to the maximum intensity value of the radiation produced by the substances changes toward the lower energy, or bigger wavelength, parts of the electromagnetic spectrum.

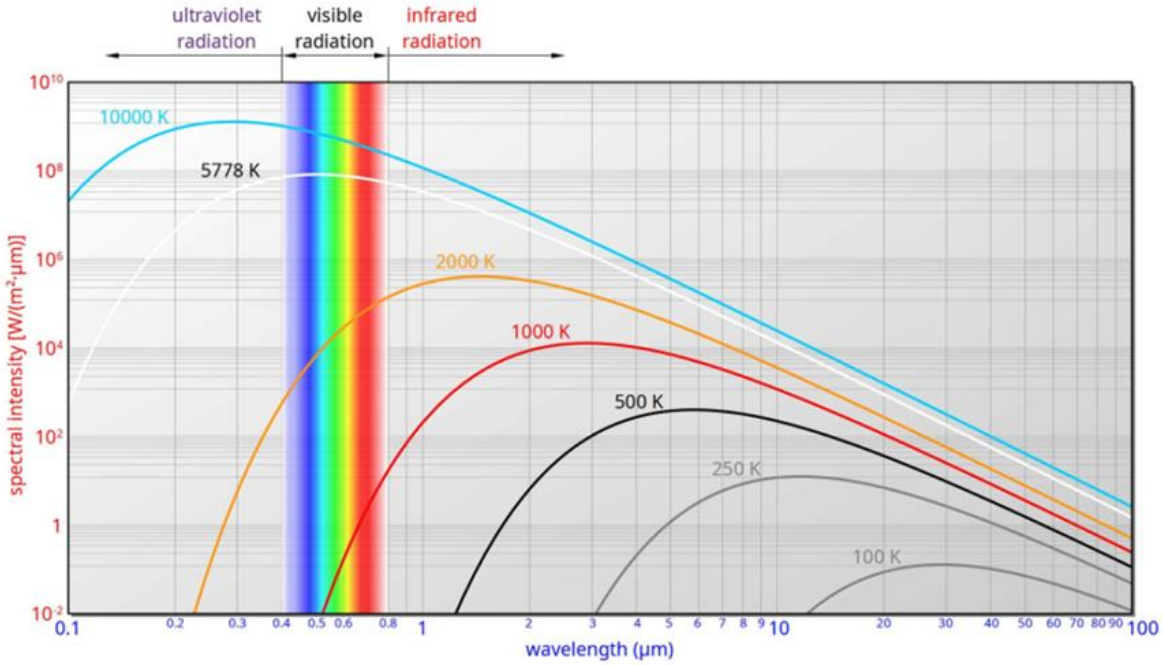


**Figure 1.4** Spectral distribution of the intensity of the radiation of a blackbody (Planck spectrum).

Amount of this shift can be calculated with Wien's Law in Equation 1 [17].

$$\lambda_{max} \times T = 2897.75\ (\mu m.K) \qquad \text{Eq 1}$$

Here, $\lambda_{max}$ denotes the wavelength at which the material emits the most intense radiation at a specified temperature value. As seen in Figure 1.4, the entire spectrum of radiation emitted by substances at temperatures experienced in daily life is contained within the infrared region. Use of thermal imaging is a word used to describe the work done by equipment that can detect this type of radiation. These devices enable detection of radiation in wavelengths that the human eye cannot detect. Thermal cameras, which

have been used in military fields for a long time, have recently been used for environmental feedback in self-driving cars.

## *1.4 ZnSe as infrared Optical Ceramic*

Zinc Selenide (ZnSe) is a semiconductor compound that consists of elements of the II-VI group. Studies on ZnSe have progressed rapidly, gaining more importance from the past to the present. At ambient temperature, ZnSe has a forbidden energy gap of 2.70 eV and at 10 K, it has a forbidden energy gap of 2.82 eV. Due to its broad transmission wavelength range of 21.5 μm to 0.45 μm, it is suitable for its use as an infrared optical material.

ZnSe is a yellow-colored compound in powder form and it has excellent optical and thermal characteristics. For example, the refractive index of ZnSe material variation with temperature is insignificant. As a result of these properties, it is a highly desirable host material for high-power $CO_2$ laser systems [18, 19].

ZnSe, which can be synthesized in single crystalline, polycrystalline, thin-film, and powder forms according to the application area, has a cubic crystal structure at low temperatures and has a crystal lattice parameter of 5.6687 Å. As shown in Figure 1.5, selenium atoms in ZnSe unit cell are packed as face-center cubic and Zinc atoms occupy half of tetrahedral sites.

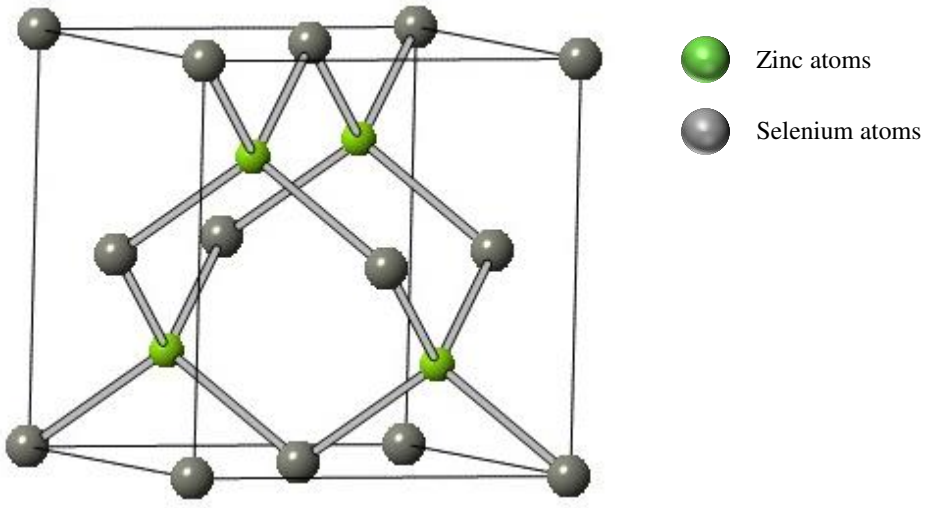


**Figure 1. 5** Zinc blende crystal structure of ZnSe.

Zinc blende and wurtzite are the two structural phases found in crystalline ZnSe. However, wurtzite phase of ZnSe is unstable under ambient conditions. There are several studies in literature to make wurtzite ZnSe thermodynamically stable under ambient conditions [20-23]. However, it still has not been made a preferable material for optical applications.

Transparent materials have a wide range of uses today. Some of these usage areas, which vary according to the wavelengths transmitted and the mechanical and chemical properties of the material, are computers, electronic devices that perform signal transmission and processing, radar systems, lasers. Among these materials, ZnSe is frequently used as an optical element, as protective windows, and IR lenses in spectral devices [24]. In addition, due to its relatively good mechanical properties, isotropic structure, and low phonon energy, it is frequently preferred as a host material for different ions such as $Fe^{2+}$, $Cr^{2+}$ and as a pump light source in different laser systems [25-27].

### *1.4.1 Synthesis Methods of ZnSe*

ZnSe compound can be synthesized in powder, thin film, polycrystalline, and single-crystal forms depending on the application area, and each has its own advantages. There are many ways to synthesize the ZnSe compound and to convert it into bulk form. Some of these are Chemical Vapor Deposition (CVD) [28], Phyisical Vapor Transport (PVT) [29], Bridgman-Stockbarger Process [30], Solid State Synthesis [31], Co-Precipitation Synthesis [32, 33], mechanical alloying via high energy ball milling [34], Hot Press (HP) [35], Hot Isostatic Press (HIP) [36] and Spark Plasma Sintering (SPS) [37].

The most preferred method to obtain laser crystals from ZnSe material is CVD. With this method, ZnSe thin films and bulk crystals can be produced successfully. CVD utilizes volatile gaseous precursors that are introduced into the chamber and allowed to react at ambient temperature. Thin films of the desired product are coated to the substrate's surface. By adjusting the temperature and pressure, the substrate, and the concentration of the gas mixture, it is possible to generate thin film materials ranging in size from nanometer to millimeter and holding a variety of chemical and physical

properties. CVD has a number of advantages, including the ability to produce homogeneous films with low porosity, high purity, and stability [38].

However, CVD technique has certain drawbacks, such as the high cost of equipment and the emission of harmful gaseous byproducts during the reaction. First, reactant species are transported to the substrate, then volatile molecules are diffused to the growth site and the precursor is adsorbed on the substrate, and then a chemical reaction occurs, by-products are desorptioned, and finally, the by-products are transported away from the substrate [39, 40]. The typical reaction that takes place in this synthesis is given in the Equation 2 [28].

$$Zn\ (g) + H_2Se\ (g) \rightarrow ZnSe\ (s) + H_2(g) \qquad \text{Eq. 2}$$

As mention earlier, the optical characteristics of bulk ZnSe materials synthesized using CVD are fairly good, and the method's parameters have been optimized. The characteristics of ZnSe produced using CVD technique are listed in Table 1.3 and its optical properties are shown in Figure 1.6.

**Table 1. 3** Properties of ZnSe synthesized by CVD (Table were retrieved from https://www.thorlabs.com).

| | |
|---|---|
| *Transmission Range*<br>0.6 to 21.0µm | *Specific Heat Capacity*<br>339 J $Kg^{-1}$ $K^{-1}$ |
| *Refractive Index*<br>2.4028 at 10.6µm | *Solubility*<br>0.001g/100g water |
| *Reflection Loss*<br>29.1% at 10.6µm | *Density*<br>5.27 g/cc |
| *Absorption Coefficient*<br>0.0005 $cm^{-1}$ at 10.6µm | *Specific Heat Capacity*<br>339 J $Kg^{-1}$ $K^{-1}$ |
| *Melting Point*<br>1525°C | *Youngs Modulus (E)*<br>67.2 GPa |
| *Thermal Conductivity*<br>18 W $m^{-1}$ $K^{-1}$ at 298K | *Molecular Weight*<br>144.33 g/mol |
| *Thermal Expansion*<br>7.1 x $10^{-6}$ $K^{-1}$ at 273K | *Class/Structure*<br>FCC Cubic, F43m (#216), Zinc Blende Structure (Polycrystalline) |

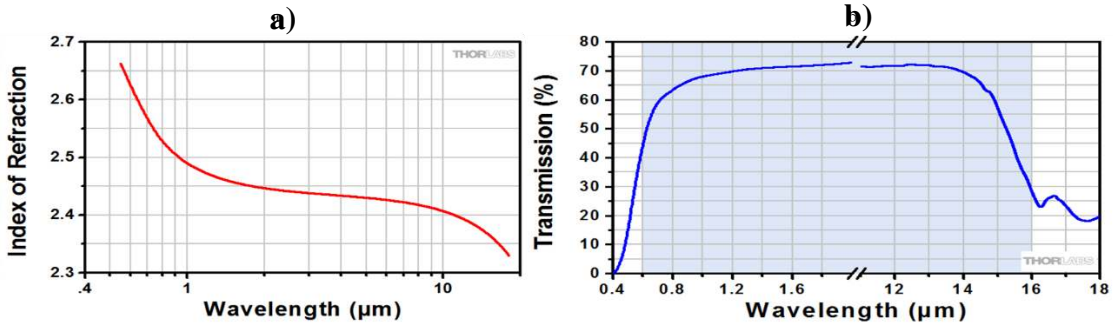


**Figure 1. 6** a) Refraction index of CVD ZnSe b) Transmission range of CVD ZnSe (Figures were retrieved from https://www.thorlabs.com).

Despite these outstanding optical properties, because the CVD method is extremely toxic, has a relatively slow growth rate in mass production, and is an expensive procedure, there has been a long-standing need for less expensive, simpler, and more environmentally friendly ways.

### *1.4.2 Bulk ZnSe Synthesis from Powder*

One of the methods of obtaining ZnSe laser host materials is to make polycrystalline ZnSe in powder form by pressure sintering methods such as hot-press, hot-isostatic press and Spark Plasma Sintering. Solid state synthesis, Co-precipitation synthesis, mechanical alloying via high energy ball milling methods have become popular in recent years in obtaining polycrystalline ZnSe in powder form. The fact that these methods are cheap, environmentally friendly, and easy to process compared to CVD has made them the center of attention. However, each has its own unique challenges.

The following requirements must be followed in order to get a material with excellent optical quality from powder material.

1) Very pure starting raw materials
2) A uniform size distribution
3) Single phase nature.
4) Large grain sizes (≈ 60–70 µm)
5) Low grain boundary density

The aforementioned requirements must be followed in order to create a bulk material with good optical characteristics from powdered ZnSe material. In solid state synthesis, ball milling synthesis, and co-precipitation syntheses, some problems may occur in order to meet the above 5 conditions.

After solid state synthesis, ZnSe material should be ground in a mortar or ball milling. While contamination is a possibility at these steps, it might be challenging to achieve an uniform size distribution. The optical characteristics of the bulk material obtained by sintering the powder ZnSe synthesized using this method is very process-dependent.

All of the issues stated above apply the same standard to ball milling synthesis. Metal contamination from the vial or balls, the formation of ZnSe powder particles with extremely small grain sizes, the formation of ZnSe powder with a very widespread size distribution, and the loss of Zn and Se stoichiometry are all quite probable during the ball milling synthesis. The synthesis of ZnSe bulk materials with high optical properties using ball milling and solid-state methods is significantly lacking in the literature. To overcome the difficulties discussed in this thesis, several methods were used, including purification of already-reacted samples and sieving already-reacted powder.

Other methods used in the synthesis of ZnSe powder are chemical methods such as sonochemical [41], co-precipitation [42], and hydrothermal [43]. The fact that the ZnSe powder material obtained by these methods has a uniform size distribution and a very precise stoichiometry are the factors that make wet chemistry methods advantageous. On the other hand, organic impurities, very small grain sizes, and synthesis conditions that are relatively difficult to optimize are disadvantages.

### *1.4.3 Sintering Techniques*

It is possible to make polycrystalline ZnSe in bulk from as a pellet from its analogous powder, which is synthesized by the methods mentioned in Section 1.4.2, specifically, by pressure sintering methods such as HP, HIP and SPS. In particular, SPS has become very popular over the years as it enables the production of rather dense materials in shorter times due to the abbreviation of high heating rate in sintering time. The SPS technique is based on the principle that a DC current is passed through the material placed in the graphite mold to heat it under pressure. Although ZnSe powder

has begun to be preferred for polycrystalline sintering in recent years, the primary disadvantage of this method is that carbon can diffuse from the graphite die to the sample during the sintering stage [44-47]. There are studies in the literature focusing on 3 ways to prevent the carbon diffusing phenomena.

1) Using protective sheets such as Tantalum (Ta), Titanium (Ti), Tungsten Carbide (WC) between punchers and the powder material
2) Using a die made from a material other than Carbon
3) Decreasing the heating rate

The first of the three solutions mentioned is based on the principle of isolating the sample from graphite die by using some materials, such as Tantalum, Titanium, Tungsten carbide and Molybdenum, which are very stable at high temperatures, as a protective sheet. Although it has been shown in the literature that this method protects the sintered material from carbon diffusing, the expensiveness of the aforementioned protective sheets prevents this technique from being sustainable [44, 48, 49].

The second solution is based on the principle of replacing all parts that can cause carbon contamination. This method has not been tried since this situation requires structural changes on the SPS device.

The third solution is based on the principle of making the sample as dense as possible before it reaches the temperature at which the carbon diffusing event will start. This method has been shown to prevent carbon diffusing [46]. In this thesis, SPS parameters have been adjusted considering this method, since it is both economical and significantly reduces carbon contamination.

Apart from sintering with SPS, sintering with HP and HIP, which has been preferred for a long time, is also used to obtain bulk crystal from ZnSe powder material in the literature [35, 50-52]. In particular, the HIP is highly preferred in the production of bulk materials with good optical properties, as it pressurizes the powder sample equally from all sides as isostatic.

### *1.4.4 Growth of Bulk ZnSe in Single-Crystal Form*

Undoubtedly, ZnSe crystals in single-crystal form have the best values in terms of optical properties. The three most common methods used to grow ZnSe single-crystals are CVD, CVT, and Bridgman-Stockbarger processes. The advantages and disadvantages of the CVD technique are previously mentioned in detail in Section 1.4.1.

The Bridgman-Stockbarger method takes its name from Percy Williams Bridgman and Donald C. Stockbarger and is successfully used in the synthesis of ZnSe single-crystal in bulk form with excellent optical properties [53-55]. In this method, the basic principle is to melt the polycrystalline ZnSe material above the melting point and slowly cool it in the seed crystal orientation on the seed crystal to grow a single-crystal [56]. Since it is a more expensive method than CVT, it has not been used in this present thesis.

The CVT method, whose mechanism is mentioned in the Section 3.1.5, is one of the methods successfully applied to grow ZnSe single-crystals [57-60]. Although using a seed crystal on which polycrystalline ZnSe material will grow in this method makes it easier to obtain larger single-crystals [60-62], it is possible to obtain large single-crystals without using seed crystals [57, 58]. As mentioned in Section 2.1.6, the transport of powder ZnSe material takes place with the help of a transport agent. $I_2$ has been preferred as the transport agent in most of the studies carried out so far, and the synthesis conditions have been optimized.

$ZnCl_2$, which can be used in the growth of ZnO single-crystals and the synthesis of ZnSe polycrystalline by solid state method, has not been used as a transport agent in the growth of ZnSe single-crystals before [31, 63]. Although optimization of the synthesis conditions is needed in this thesis, it has been shown that $ZnCl_2$ is a promising transport agent in the growth of ZnSe single-crystals by CVT method.

## *1.5 Lasers*

In this thesis, it is aimed to develop the optical properties and synthesis of ZnSe polycrystalline and single-crystals, which will be used as gain medium to obtain laser irradiation around the Mid-IR region. Since the aforementioned host crystals have low phonon energy, the possibility of electronic transitions to occur with the help of phonons decreases. Since this increases the radiation efficiency, it makes the proposed materials very promising for their use as a gain medium in high-efficiency lasers.

The low phonon energies of $Tm^{3+}$:$YLiF_4$, $Tm^{3+}$:$KY_3F_{10}$ and $Tm^{3+}$:$BaY_2F_8$ laser crystals operating around 2 μm is an important motivation for choosing ZnSe crystals as host material [64].

The advantage of using these materials is that the mechanical strength of ZnSe crystals is better (high hardness/low brittleness) than the above-mentioned crystals and that these properties change less depending on temperature. Other important reasons for choosing ZnSe crystals as host material are that they can be used independently of orientation without applying a special cutting process due to their cubic crystal structure and their relatively low cost.

### *1.5.1 History of Lasers*

Since the ruby laser, which was first developed 60 years ago, studies in this field continue with an increasing momentum [65]. The main reason for this increasing interest is that laser sources, which can operate at different wavelengths, different powers and different regimes, can find a wide range of applications for themselves and imaginable application areas are ahead of the action [66]. Despite the diversity of lasers, the fact that each can find its own application area is the most important indicator of how important they are for basic engineering and science.

Stimulated emission, which is the basis of the operation of lasers, was first predicted theoretically by Albert Einstein in 1917, and then lasers have continued to develop rapidly until today [67]. Developments that can be considered as milestones in the historical development of lasers are listed in Table 1.4.

**Table 1. 4** Milestones about the Lasers.

| Date | Name | Success |
|---|---|---|
| 1916 | Albert Einstein | Propagation theory of light. Stimulated radiation concept. |
| 1928 | Rudolph W Landenburg | Proving the existence of negative absorption and stimulated radiation |
| 1940 | Valentin A. Fabrikant | The probability of up-conversion population |
| 1947 | Wills E. Lamb<br>R.C. Retherford | First demonstration of excited radiation |
| 1951 | Charles H Townes<br>Alexander Prokhorov<br>Nikolai G Basov | Mazer (Microwave Amplification of Stimulated Emission of Radiation) discovery. 1964 Nobel prize. |
| 1960 | Arthur L Schawlow<br>Charles H Townes | Laser patent. |
| 1960 | Theodore Maiman<br>Ali Javan | The discovery of the ruby laser. |
| 1961 | William Bennet Jr.<br>Donald Herriot<br>J.E Geusic | Discovery of the Helium Neon laser. |
| 1964 | H.M. MArkos<br>L.G. Van Uiteit | Discovery of the Nd:YAG laser. |
| 1964 | Kumar N. Patel | Discovery of the $CO_2$ Laser |
| 1964 | William Bridges | Discovery of Argon Ion Laser. |
| 1965 | George Pimentel<br>J.V.V. Kasper | First chemical laser. |
| 1970 | Nikolai Basov | The first Excimer Laser made with Xenon. |
| 1977 | John M.J. Madey | First free electron laser. |
| 1984 | Arthur Schwlow<br>Nicolas Bloembergen | Nobel prize in Physics for work in nonlinear optics and spectroscopy. |

In solid state lasers, the optical gain medium is obtained by doping radiant ions to glass, ceramics, or crystals. Since optical gain media synthesized in this way are more

stable mechanically and chemically, they are less affected by environmental conditions. Therefore, their working life is much longer. In solid state lasers, ions of transition metals (Cr, Fe, etc.) or ions of rare earth elements (Gd, Er, Ho, Tm etc.) are used as doping elements. The wavelength of the radiation to be obtained can be changed by using different crystal-ion combinations, and lasers that provide the necessary properties can be produced according to the required area.

### *1.5.2 Working Principle of Lasers*

The bulk material obtained from ZnSe does not oxidize in the atmosphere up to a temperature of 300 °C, the refractive index changes depending on the temperature is low, the refractive index is homogeneous at varying wavelengths, it is not toxic, it is a crystal with low phonon energy, and it shows isotropic properties due to its cubic crystal structure. and its transparency in a wide range of the electromagnetic spectrum (0.6μm-21μm) makes it preferable over many transparent ceramics for use as a laser crystal.

As it is known, the word Laser is an acronym. It stands for Light Amplification by Stimulated Emission of Radiation. It has 3 main differences from normal light. These are;

1) Laser light is monochromatic, it contains only one wavelength.

2) Laser light is coherence, there is no phase difference between wave packets.

3) Laser light is linear, has very little dispersion, and can be considered unidirectional.

The absorption and emission of electromagnetic waves by an atom basically occurs in 3 ways;

1) Self-luminescence: An atom in the excited energy level reduces its energy by spontaneously emitting photons.

2) Absorption: Absorption of photons and increasing energy level of an atom in the basic energy level by being exposed to a light of appropriate wavelength.

3) Exciting radiation: An atom in the excited energy level emits a second photon in the same phase with the same wavelength as the excited photon, during the transition to a low energy level by being excited with a light of the appropriate wavelength.

The basic principle underlying the working mechanism of lasers is the 3rd way mentioned above (excited radiation).

One of the structures used as host material in solid state lasers is crystals. Ions of some elements (usually rare earth elements) capable of laser irradiation are doped into this crystal structure, and this crystal structure, which is called the gain medium, is placed between a mirror with a transmittance of 1% to 10% and another mirror with high optical reflectivity (Figure 1.7a). When the gain medium is excited with suitable pump wavelengths, the ions in the crystal radiate and thus the photons oscillating between the mirrors cause a chain radiation reaction (Figure 1.7c). As the number of photons produced in the gain medium increases, some loss mechanisms start to come into play, and after a while, the system reaches saturation and maximum power is obtained (Figure 1.7d).

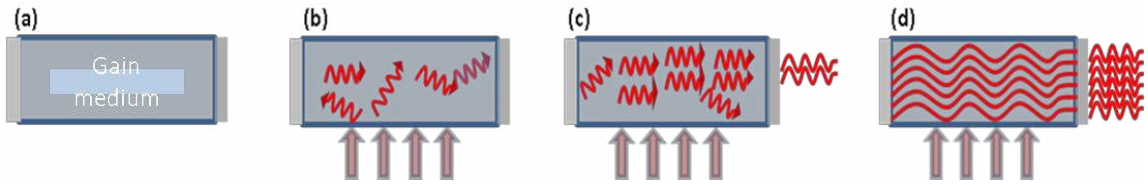


**Figure 1. 7** (a) Optical pump is not active, (b) Optical pump is active, (c) After a while, photons accumulated inside are output from optically transparent mirror, (d) Saturated gain medium.

The most important reason why the elements doped to the host material are generally rare earth elements is their electronic configurations. When lanthanide ions are doped into a crystal structure, its electronic configuration in the crystal structure is given as:

$$1s^2 2s^2 2p^6 3s^2 3p^6 4s^2 3d^{10} 4p^6 5s^2 4d^{10} 5p^6 6s^2 4f^p$$

Here, p varies from, 1 to 13 and hence atomic numbers vary from Z = 58 ($Ce^{3+}$) to Z = 70 ($Yb^{3+}$). All of these ions contain the partially filled 4f shell. Optical activities

consist of transitions between 4f levels. The abundance of transitions between the 4f levels of these ions and the possibility of obtaining radiation at many wavelengths are the most important reasons why lanthanide ions are preferred as doping elements for laser gain environments.

Another important reason is that the 4f electronic levels are significantly insulated from external influences. Namely; 4f electrons of rare earth elements settle to the lowest levels in their shell and are isolated from external influences with their outer $5p^6 6s^2$ shells, which are full. Thus, when rare earth elements are doped into a crystalline or amorphous structure, their energy levels perturb very little due to the crystal field. Therefore, regardless of which crystal it is doped with, the 4f energy levels of rare earth ions do not change significantly and have a very narrow energy band.

However, the radiative and non-radiative transition probabilities between these levels are affected by their environment. Research on suitable host materials for lasers is therefore ongoing.

### *1.5.3 Some Application Areas of Lasers Working in Infrared Regions*

Lasers can be used as supportive treatment in cancer diseases. For this, LED or laser light is used to stimulate light-sensitive agents such as $Fe_3O_4$, and it is used in photodynamic therapies based on killing cancerous cells by destroying their protein and lipid structures by causing toxicity [68].

The penetration depth in water of lasers operating in the 1.8-2.4 μm wavelength range varies between 100-1500 μm [69]. Since the most important parameter in the absorption of laser light in living tissue is the water it contains, the same damping depths are also valid in human tissue, with observations being constant. Especially for laser beams with a wavelength of 1.9-2.0 μm, the depth of extinction is minimized. This means that the energy of the laser beam produced by the laser source, which can operate at the mentioned wavelengths, will be absorbed by a smaller volume. This physical reality makes it possible to use these wavelengths in medical applications. For example, if we consider the human skin, almost all of the energy of a laser beam with a wavelength of around 2.0 μm is absorbed at the skin surface. In this way, very precise superficial cutting operations are possible without going deeper into the tissue, and

blood loss is prevented by accelerating coagulation. In addition, tissue fusion processes can be performed with adjustments in the power of laser systems [70].

Another important medical application of lasers that can operate in the infrared region is coherent optical cross-section imaging. Thanks to this method, high resolution, cellular size and real-time imaging can be obtained by utilizing the interference properties of light. The basic principle in this method is to divide a broad spectrum laser light into two, send it to the tissue desired to be imaged and a reference mirror, and then process the interference data of the rays reflected from these two different sources to form an image. The most important advantage of this method is that, due to the large spectral width of the light used, the interference acquisition length is very small, and thus real-time images can be obtained at the cellular level [71].

Another important medical application is two-multi-photon microscopy, which can only be possible by using laser light and by introducing some quantum mechanical phenomena. As it is known, in standard fluorescence microscopy, some special substances that can radiate when excited at certain wavelengths are loaded into the tissue and an image is formed by analyzing the light emitted by these substances. However, in this method, apart from the metal loaded on the tissue, which has the ability to produce fluorescent radiation, the tissue itself can also radiate, which causes noise in the output signal. This problem can only be solved by two-to-multi-photon excitation, which is possible only with lasers and can be explained quite clearly by the principles of quantum mechanics. In two-multiple photon excitation, the atom to be excited to upper energy levels with a light with a wavelength of $\lambda$ is excited to the same level using a light with a wavelength of $2\lambda$. But this time, the electron acts as if there is another energy level between the two energy levels, and rises to this level in two stages. In order for this phenomenon to occur in fluorescent materials, the intensity of the stimulating light must be very high. This is where the noise problem that arises in the standard fluorescence imaging technique is solved. Because two-multi-photon excitation takes place only in the region where the beam is focused. Therefore, when the tissue is irradiated at the mentioned intensities, two-multi-photon excitation occurs in the fluorescent material, while it does not occur in normal tissue. Thus, an image containing much less noise signal can be obtained [72].

Lasers that can operate at various wavelengths and regimes are also frequently used by dentists. For example, Diode lasers that can operate around 1 μm wavelength

are used for gingival shaping, stopping bleeding, teeth whitening [73], Ho:YAG lasers, which can operate around 2 μm wavelength, are used for ablation in skull and oral surgery as well as hard calcified tissues [74, 75] and Er:YAG lasers, which can operate around 3 μm, are used for removing carious tissue, increasing the adhesion of restorative materials with enamel surface modification, and bone removal [75-80].

### *1.5.4 Application Areas of Lasers Operating in the Mid-Infrared Region*

In addition to the medical application areas of lasers operating in the mid-infrared region, pumping lasers operating at higher wavelengths of the mid-infrared region [81], remote sensing [82], laser radar (LIDAR) [83] and coherent high harmonic generation in the X-Ray region [84].

Especially in the military field, mapping capability is very important. LIDAR, which stands for Light Detection and Ranging, is a type of remote sensing system that uses laser light for the measurement process and is highly effective in atmospheric measurements and surface mapping. Today, the importance of remote sensing systems is undoubtedly very great. The reason for this is that alternative methods are much more inefficient than remote sensing systems in terms of both cost and time. The biggest advantage of LIDAR, which is an active remote sensing method, over RADAR is that it uses laser light to collect data. As it is known, although the scattering of laser light varies according to the medium and wavelength, it is negligible compared to other light sources. In this way, much higher resolution imaging can be created with the data to be obtained from LIDAR systems. However, the question of which of the laser lights of different wavelengths will produce the best quality data for this application is very important. The laser light traveling in the atmosphere both expands due to diffraction and is scattered due to the interactions it enters with the molecules and atoms in the environment. These situations can suppress the desired signal in the collected data. For this reason, it is very important to choose the laser source that will produce the appropriate wavelength according to the conditions. In LIDAR applications, laser sources with wavelengths around ultraviolet are preferred in order to minimize diffraction-induced dispersion. As seen in Equation 3, the fact that the Rayleigh distance is inversely proportional to the wavelength of the light is the most important reason for the use of lasers operating around ultraviolet in LIDAR application [85].

$$z_R = \frac{n_0 \pi {w_0}^2}{\lambda} \quad \text{Eq. 3}$$

where $z_R$is the Rayleigh distance, $n_0$ is the refractive index, ${w_0}^2$ is the radius of the beam at focus, and λ is the wavelength. The environment in which LIDAR is used is mostly the atmosphere. Therefore, the scattering of light due to interactions with other molecules and atoms in the atmosphere is also a very important parameter. As stated in Equation 4, the Rayleigh scattering is the fourth-order power of λ. Therefore, the positive effect of working at large wavelengths on the Rayleigh scattering avoids the negative effect on the Rayleigh distance, which represents the dispersion. For this reason, lasers that can operate in the mid-infrared region promise much less scattering than ultraviolet lasers for LIDAR application.

$$\sigma_s = \frac{128\pi^5 a^6}{3\lambda^4} \left| \frac{\varepsilon_r - 1}{\varepsilon_r + 2} \right|^2 \quad \text{Eq. 4}$$

where $\sigma_s$ is Rayleigh scattering, a is the radius of the sphere formed by the scattering dipole, $\varepsilon_r$ is the electrical permittivity of the medium, λ is the wavelength.

# Chapter 2:
# EXPERIMENTAL METHODS & CHARACTERIZATION

## *2.1 Sample preparation methods*

### *2.1.1 Solid State Synthesis*

Zn powder (Sigma Aldrich 99.99%) and Se powder (Sigma Aldrich 99.99%), which are the starting materials in solid state synthesis, were loaded in a 1:1 stoichiometry into a quartz tube that has been previously washed with acetone in the glove box (Figure 2.1a). Then, it was sealed after vacuuming up to $10^{-2}$ Torr pressure for at least 30 min by using a Schlenk line (Figure 2.1b).

Finally, the sealed quartz tube was placed in a furnace and heated to 1000 $^{\circ}$C with a heating rate of 5 K/min. Synthesis duration was 21 days at 1000 $^{\circ}$C (Figure 2.1c). After synthesis the furnace was cooled at 5 K/min cooling rate. In Figure 2.1 the synthesis process was given briefly.

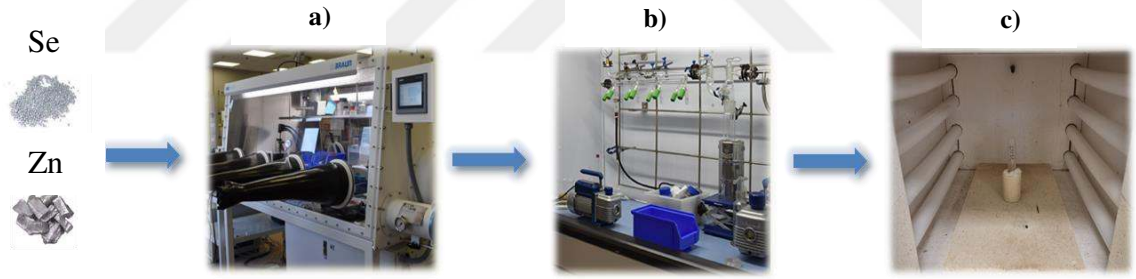


**Figure 2. 1** The route of solid state synthesis. a) Loading the quartz tube with starting material powder Zn and powder Se in glove box, b) Sealing the loaded quartz tube under vacuum, c) Reaction of polycrystalline ZnSe material in furnace at high temperatures.

There are two important points to consider at this stage. The first is that Se and Zn starting materials, which are in powder form, are dispersed as homogeneously as possible in the quartz tube in order to obtain a uniform structure at the end of the solid-state synthesis. When the bulk ZnSe obtained after the synthesis is not homogeneous, the powder ZnSe obtained from it is also not going to be in a homogeneous form. This situation affects the transparency negatively after sintering with SPS.

The second is to ensure that the quartz tube loaded in the Glove box does not leak when transporting it to the sealing station. Even if there is very little oxygen in the quartz tube, the $ZnO_2$ phase can be formed after synthesis in a case of a leak. Since the secondary phases work as scattering points, it negatively affects the transparency of optical materials.

### *2.1.2 Synthesis with high-energy ball milling*

High energy ball mill device (SpexSamplePrep 8000D) was used for ZnSe synthesis. Zinc shot (ZS), small pieces of zinc (SPoZ), zinc powder (ZP), shot Selenium (SS), and selenium powder (SP) were used in different combinations as the starting material in this synthesis method. Two grinding vials were clamped together and shaken back and forth with brief lateral movements. As a result, powders react with one another, resulting in mechanical alloying. Figure 2.2 illustrates the stainless steel vial, stainless steel balls, un-reacted powder mixture, and the high-energy ball mill device.

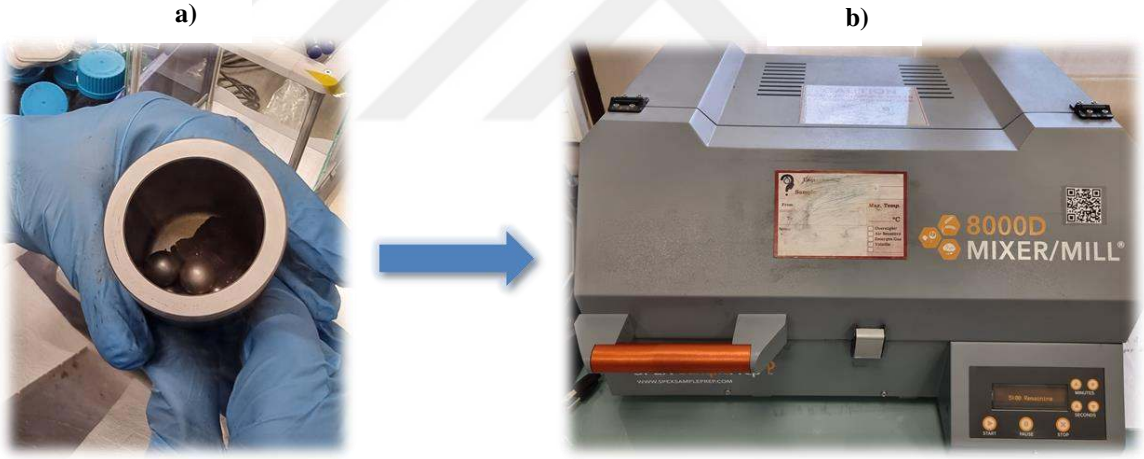


**Figure 2. 2** Ball milling synthesis. a) Loading the vial with stainless steel balls and raw material in glove box, b) ball milling synthesis with SpexSamplePrep 8000D.

There are two important factors affecting the reaction in ball milling synthesis. These are the size configurations and the number of stainless steel balls placed in the vial and the ratio of the mass of these balls (MoB) to the mass of the reactants (MoR). These parameters should be optimized in this synthesis. After the reactants were placed in a stainless steel vial in the glove box, they were reacted with a ball milling for varying durations from 60 minutes to 240 minutes. The ratio of the masses of the reactants to the masses of the stainless steel balls was 1:5, 1:8, and 1:20.

### *2.1.3 Co-precipitation Synthesis*

ZnSe nanopowders were synthesized via co-precipitation. To prepare the $Se^{2-}$ solution, a solution of $NaBH_4$ (96.0 percent, Sigma-Aldrich) was prepared by dissolving it in deionized water and then adding it to a stoichiometric amount of Se (99.99 percent, Sigma-Aldrich) stored in an Ar-flushed flask to obtain a 0.1 mol/L solution.

After a substantial amount of redox interaction between Se and $NaBH_4$ took place, a clear and transparent NaHSe solution was formed as a source of $Se^{2-}$. Then, stoichiometric amounts of $ZnCl_2$ (99.9 percent, Sigma-Aldrich) was dissolved in deionized water to form a solution with an overall cation concentration of 0.15 mol/L, and the pH of the solution was adjusted to between 3-5 by adding 69 percent $HNO_3$ solution (Sigma-Aldrich). Finally, a dropwise addition of the $Zn^{2+}$ cation solution to the NaHSe solution produced an orange precipitate. Then, the precipitant solution was left for aging for 24 h. Figure 2.3 shows the color change of the solution by time during this aging step. After this 24 h period, the precipitate was centrifuged, washed multiple times with 100% ethyl alcohol, and dried for 24 hours in argon at 80°C. The dried precipitate was crushed in an agate mortar and calcined for 6 hours at 400°C in argon. In Figure 2.3, the color change occurring during the synthesis is given depending on time [37].

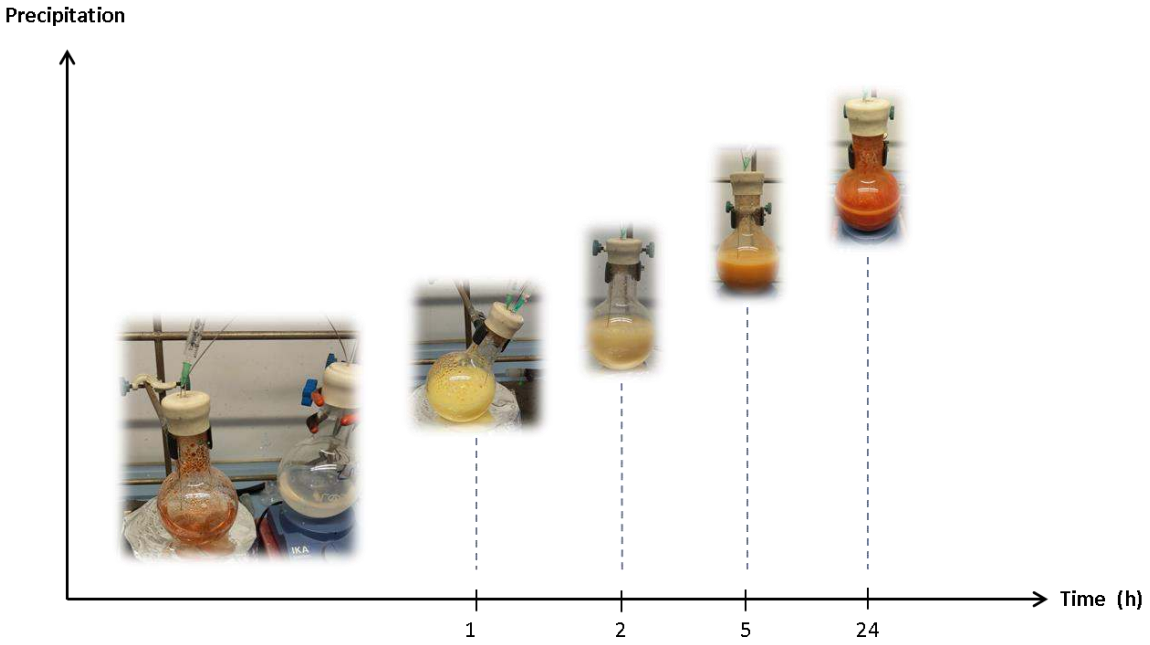


**Figure 2. 3** Color change by time during Co-precipitation synthesis of ZnSe.

### *2.1.4 Spark Plasma Sintering*

SPS method is the most remarkable and frequently used method especially in the last 20 years. The SPS method can be considerd as a modified hot-pressing system such that the electic current is passed through the material which is placed into a graphite die.

This technology is characterized by a faster heating rate, a reduced sintering temperature and duration, and densification of difficult-to-sinter powders. Compared with other traditional sintering techniques such as HP and HIP, SPS has great advantages both economically and technologically.

SPS systems, which are mainly uniaxial pressure application systems, include water-cooled lower and upper electrodes, a water-cooled vacuum unit, a vacuum/air/ atmosphere control unit, a pulsed direct current generator, and a cooling water unit. Dispalcement of the electrodes during sintering process can be determined very precisely (± 1 μm). By controlling this displacement, it can be determined manually at which temperature and pressure values the sample becomes denser.

SPS parameters should be optimized according to the usage areas of the sintered materials. These parameters are heating rate, annealing temperature, sintering time at maximum temperature, cooling rate, pressure to be applied on the sample, and chamber atmosphere.

Despite all these advantages, there are some difficulties in sintering materials with high quality optical properties with SPS technique. The most important one of these is carbon diffusion. Since the sample is sintered in the graphite mold in the SPS device, there is a risk of carbon diffuse to the material from the graphite die at high temperatures [44-47].

Spark Plasma Sintering device used in this work and a picture of sintering process of ZnSe powder material can be seen in Figure 2.4.

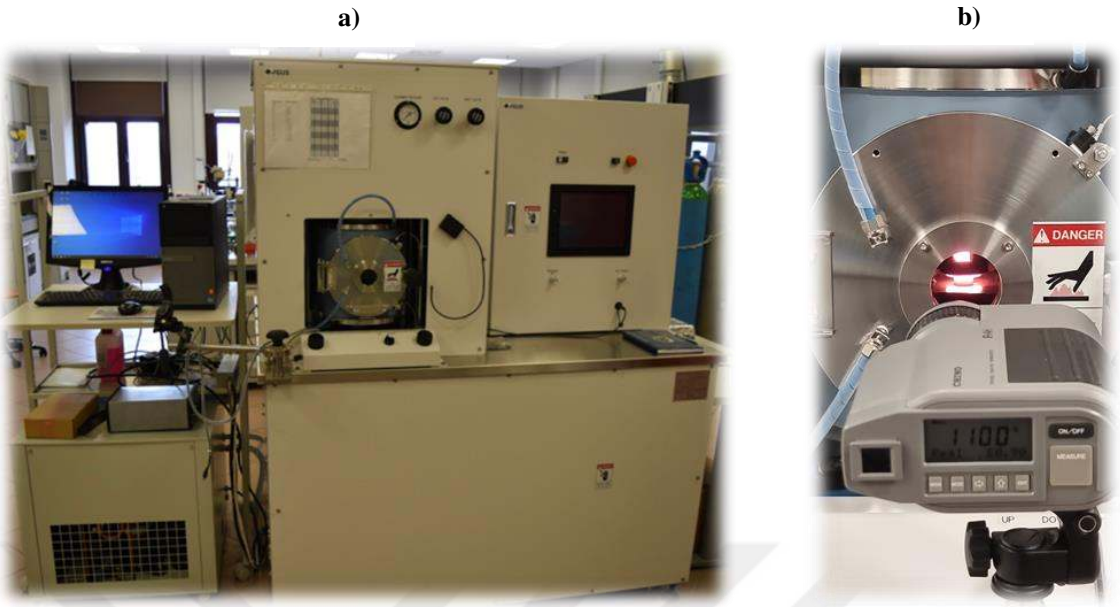


**Figure 2. 4** a) Spark Plasma Sintering device used in this work, b) a picture of sintering process of ZnSe powder material.

### *2.1.5 Polishing*

One of the factors affecting the transparency of optical materials is the reflection on the surface of the material. In order to reduce superficial reflection, the surfaces of the material should be as smooth as possible. Within the scope of this thesis, the polishing sample platform and the polishing device (EQ-UNIPOL-802) given in Figure 2.5 is used for polishing.

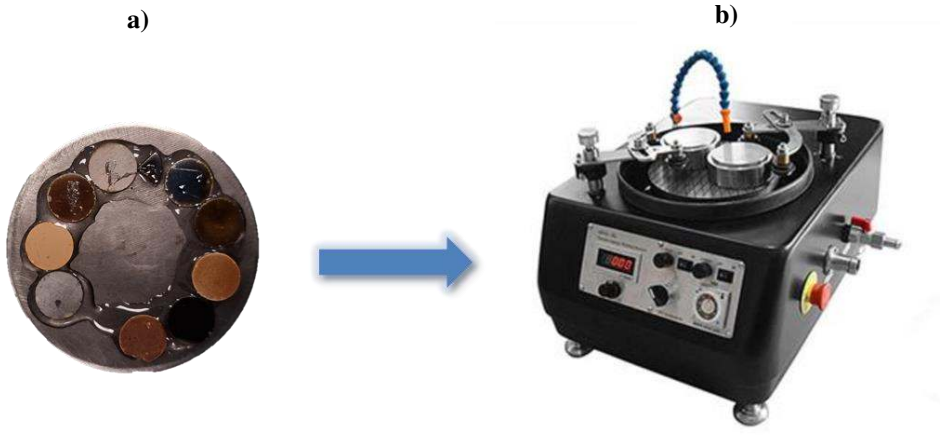


**Figure 2. 5** a) The sintered ZnSe pellets prepared for polishing and thickness tuning to 1 mm, b) The polishing device used in thesis work.

During the polishing process, sandpaper with grid sizes of 800, 1000, 1200, 2500 was used, followed by polishing liquid such as 100 nm Alumina suspension.

On the other hand, since transparency is a function of sample thickness, all samples must be of the same thickness. Thanks to the polishing device, all samples were ground to a thickness of 1 mm. Within the scope of this thesis, all optical measurements were made on 1 mm thick samples.

### *2.1.6 Chemical Vapor Transport*

Schäfer defines CVT as "solid solubility in the gas phase" [86]. As described by Schäfer, this method is based on the chemical interaction between a liquid or solid and a gaseous phase in a transport medium reversibly. A trace amount of a transport agent, such as $I_2$, $Cl_2$, $ZnCl_2$ , or $CdCl_2$, is used to generate volatile compounds of the constituent elements in order to facilitate transport and vapor phase mixing in preparation for crystal condensation. The transport agent acts as a catalyst in CVT and is released following the condensation of gaseous species.

To perform CVT reactions, ampoules which are sealed under vacuum with two temperature-separated ends are used. The driving force for this process, in other words for the material transport, is the chemical potential gradient. The reaction conditions can be optimized in terms of the total amount of sample to be transported, the type and amount of transport agent used, the volume of the container material, the system's temperature, and the partial pressures of the gaseous species present during the vapor transport reaction. Figure 2.6 shows the quartz tube prepared before and after the reaction, represented by the light yellow and orange powders, respectively.

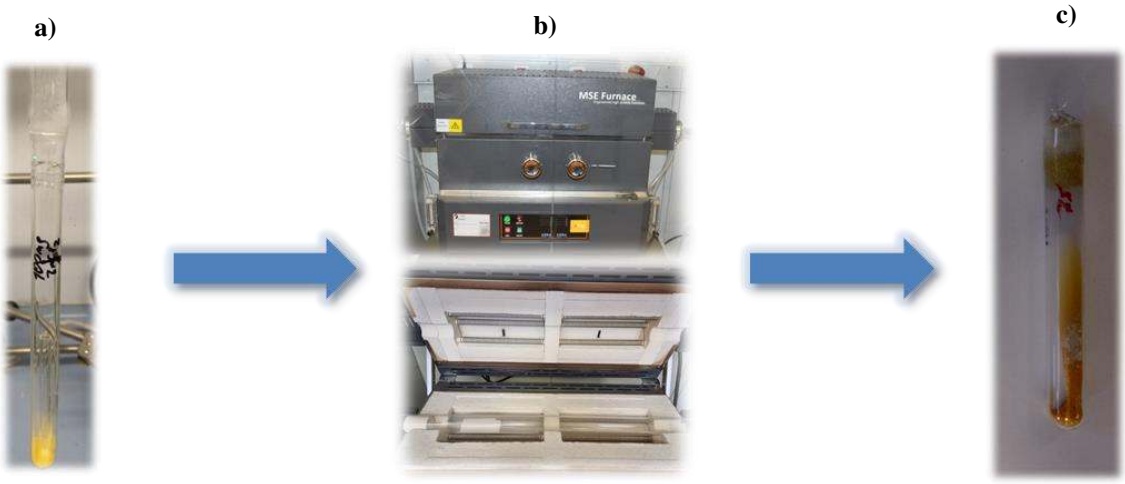


**Figure 2. 6** a) Sealed quartz tube with prereacted ZnSe polycrystalline powder and $ZnCl_2$ transport agent, b) the two-zone furnace used in this thesis work, and c) growth ZnSe single-crystals at the end of 7 days.

In this thesis, $ZnCl_2$ was used as a transport agent while growing ZnSe crystals by CVT method. Single-crystal growth conditions were optimized by using different amounts of $ZnCl_2$ and changing the heat gradient.

### *2.1.7 Density Calculation*

Density measurement of materials sintered with SPS was measured with the help of Archimedes' Principle. In this method, the basic principle is based on measuring the own weight ($w_s$) of the sample whose density is to be measured and its weight ($w_L$) in a liquid with a known density. By using the Equation 5, the density of the material can be calculated regardless of what shape it is.

$$d_{solid} = d_{liquid} \left(\frac{w_s}{w_s - w_L}\right) \quad \text{Eq. 5}$$

In the density measurements made within the scope of this thesis, pure ethanol was used as a liquid. The weighing system used for density measurement was built on a regular laboratory weight.

## *2.2 Charactrazition Methods*

### *2.2.1 X-ray Diffraction and Wavelength-Dispersive Spectrometer*

Much of the knowledge gained about crystals so far is thanks to the X-ray diffraction technique which is used for qualitative identification of the crystal structure of a crystal material. The basic principle in this technique is that the charged particles, which are accelerated linearly inside the X-ray tube, are suddenly stopped by hitting a taget and emit X-rays. Metal targets such as Fe, Co, Cr, Ag, Mo are generally used to stop these accelerated electrons. When the generated X-rays are sent to a structure whose atoms are arranged in a certain order, the electric field components of the X-rays are reflected from the surfaces of the crystals and create constructive and destructive interference. These diffraction patterns serve as a kind of fingerprint for each distinct crystalline phase. The X-ray diffraction analysis method is non-destructive to the sample and enables the study of extremely tiny samples. Samples can be in the form of liquid, powder, crystal, and thin film. Bragg's law (Equation 6), where θ is angle between crystal surface and X-ray beam, d is inter-planer distance of the crystal, n is an integer and λ is wavelength of the X-ray radiation determines whether the interference will be constructive or destructive [87].

$$2d\sin\theta = n\lambda \qquad \text{Eq. 6}$$

When the conditions mentioned above are satisfied, constructive interference occurs which is recorded by a detector. These recorded intensity data are plotted with the help of a software according to 2θ. The sample is characterized by examining the peaks corresponding to certain 2θ angles. A Rigaku Miniflex XRD device with a Cu *Kα* (λ = 1.540598 Å) radiation, a 40 kV voltage, and a 15 mA current was used for the measurements.

To conduct single-crystal X-ray studies, appropriately sized single-crystals were selected and properly mounted on top of pointed glass capillary ends. Measurements on single-crystals were carried out using the STOE IPDS automatic diffractometer equipped with an open nitrogen gas stream as cooling.

A wavelength-dispersive X-Ray spectrometer (WDXS) makes advantage of the unique X-rays emitted by specific elements to perform quantitative analysis (down to trace element levels) on spots as small as a few micrometers in diameter. Additionally, by rastering the beam, WDXS can be utilized to build element X-ray compositional maps across a larger area. These capabilities, when combined, provide fundamental quantitative compositional information on a wide variety of solid materials.

The bulk samples were prepared for WDXS studies by grinding them with silicon carbide papers of various grit sizes in the presence of either alcohol with lubrication or water. As a standard for WDXS analysis, we chose either elements or their binaries with precisely specified compositions. Cameca Peak Sight software was used to accomplish the quantitative analysis. WDXS measurements were performed at Max Planck Institute for Chemical Physics of Solids (MPI-CPfS).

### *2.2.2 Scanning Electron Microscopy Coupled with Energy Dispersive X-ray Spectroscopy (SEM/EDX)*

Scanning electron microscopy is used to collect precise information about a surface's physical nature as well as exterior morphological data. In the Scanning Electron Microscope (SEM), electrons accelerated by high voltage are focused on the sample and the sample is scanned with this focused electron beam. During scanning, the effects that occur as a result of various interferences between the electron beam and the sample atoms are collected in appropriate sensors. These collected signals are processed and reflected on the monitor after passing through signal amplifiers.

Secondary electrons, backscattered electrons, diffracted backscattered electrons, photons, and heat are all created when this beam collides with the material. Secondary electrons and back scattered electrons, on the other hand, are the most often employed electrons for SEM imaging. Apart from these signals, incoming electrons collide with electrons in the atoms' shells, resulting in the creation of inelastic X-rays. Similar to previous X-ray spectroscopy techniques, the X-ray created by the excited electron's return to a lower energy state creates an X-ray with a unique wavelength for each element. This method is carried out by EDX systems attached to the SEM equipment. In addition to element identification, EDX analysis enables quantitative analysis [88].

In this thesis, two different SEM instruments were used to analyze the microstructure of the samples. These microscopes were the Philips XL 30 Scanning Electron Microscope (SEM, LaB6 cathode) coupled with an EDAX Si(Li) detector at MPI-CPfS facilities for EDX measurements and the Zeiss Ultra Plus Field Emission Scanning Electron Microscope coupled with an Bruker XFlash 5010 EDX detector at KUYTAM facilities. Bulk samples were polished with different grit sizes of SiC sandpapers before each examination. A polishing apparatus with diamond solution was employed to make the surface smoother and shinier. Following the pretreatments, the samples to be examined were placed on the sample holder's carbon tape, and the analysis was performed satisfactorily

### *2.2.3 Fourier Transform Infrared (FTIR) Spectroscopy*

FTIR is used to determine the qualitative and quantitative characteristics of molecular species of various types. It is plausible to assume that all energy changes associated with the transition from one vibrational or rotational energy state to another are due to a molecular specie's infrared absorption, emission, and reflection spectra. In other words, a molecule must have a net change in dipole moment as it vibrates or spins in order to absorb infrared light. Dispersive instruments, nondispersive instruments, and Fourier transform spectrometers are the three categories of IR absorption equipment. Using Fourier transform instruments provides a number of benefits, including speed, dependability, improved signal-to-noise ratio, and ease. A source emits IR energy into an interferometer in an IR spectrometer. Michelson interferometers are used in the majority of the instrumentation. An interferogram signal is produced by the interferometer, which produces a single type of signal. This beam is focused at the sample, and some of the sample's unique frequencies of energy are absorbed while others pass through. The signal from the detector's beam is a spectrum of transmittance or absorbance at specified wavenumbers. FTIR spectroscopy can identify the vibrational frequencies of atoms in a molecule. In other words, it reveals the binding structure. So FTIR is commonly employed to identify organic materials [89].

For the measurements, a Bruker Vertex 80v transmission spectrometer with spectral resolution of 2 $cm^{-1}$ was used. ZnSe pellets were pressed between two KBr windows. The sample holder containing the ZnSe pellet was then placed into the instrument's

vacuum sample chamber. Then, the sample compartment was evacuated to exclude air and moisture, and 64 scans were collected and averaged. Before each measurement, 32 scans were obtained for background signal.

### *2.2.4 X-Ray Photoelectron Spectroscopy (XPS)*

The XPS technique is used to determine the chemical, physical, and electrical properties of surface structures. It provides information on the chemical state of the surface by measuring the binding energies of electrons emitted from various elements. For instance, XPS enables us to manage the charging of the surfaces, which enables us to determine their electrical potential, such as their capacitance values.

The photons from the X-ray source interact with the atoms on the surface, removing electrons from the sample through a photoelectric process. An electron energy analyzer determines the kinetic energies of photoelectrons released from the surface, which are provided by the formula:

$$KE = hv - BE - \varphi \qquad \text{Eq. 7}$$

KE denotes the kinetic energy of electrons extracted from the surface; BE denotes the binding energy; hv denotes the energy of photons emitted by the X-ray source; and denotes a work function [90].

XPS measurements were carried out on an aluminum anode (Al K 14 1468.3 eV) using a Thermo Scientific K-Alpha spectrometer. The electron take-off angle was 90 degrees between the sample surface and the axis of the analyzer lens. Calibration of the instrument was performed in relation to vacuum levels in order to identify the instrument's work function. Data fitting was performed using the Avantage 5.9 program. The binding energy was calibrated using the C 1 s signal at 284.8 eV emitted by carbon impurities.

### *2.2.5 Optic microscope*

When it comes to seeing objects that are too small to see with the human eye, optical microscopy is a very useful tool. In its simplest form, an optical microscope is a pair of lenses that magnifies the picture of an object. Although we are limited by the

wavelength of light, optical microscopy continues to play an important role in scientific research.

Infinity corrected lenses are frequently used as the objective lens. Due to the fact that the image is focussed on the infinity plane, it should be recollected and refocused on a plane. This is accomplished through the use of a tube lens system. The focused picture can be sent to another lens system, such as an eyepiece, for direct viewing, or it can be sent to a CCD camera.

In this study, the crystal sizes of single-crystal ZnSe and sintered polycrystalline ZnSe pellet's grain sizes were determined by optical microscope and the surface morphologies of ZnSe materials sintered with SPS were examined.

# Chapter 3:
# RESULTS & DISCUSSION

## *3.1 Synthesis with Ball Milling*

Although the ball milling process can produce high purity ZnSe powder, it may be challenging to acquire good optical characteristics in the ZnSe pellet material that results after sintering. [91]. The major reasons for this are that the powder produced in a ball milling does not have a uniform size distribution, it lacks precise stoichiometry, and there are contaminants formed during ball milling synthesis from stainless steel balls and stainless steel vials. In this section, the synthesis conditions of ZnSe polycrystalline materials prepared by ball milling method, the problems encountered during the process and their solutions, and finally, the chemical and morphological analysis of the synthesized powder materials are discussed.

### *3.1.1 Preparation and XRD Analysis of ZnSe Powder Synthesized via Ball Milling Method*

The main problem that arose in the ball milling synthesis of ZnSe polycrystalline powder during the experiments was the observation of excess Zn or ZnO phase in the synthesized ZnSe powder. Therefore, the ZnSe stoichiometry and ball milling duration were optimized first. In this method, when the Zn starting material was in spherical shots form, the synthesis was not successful because it was a soft material (SO1). The Zn shots were then pressed in the glove box and cut into small pieces (SPoZ). ZnSe polycrystalline material was successfully synthesized using SPoZ as the starting material. SPoZ and Zn in powder form are given in Fig 3.1.

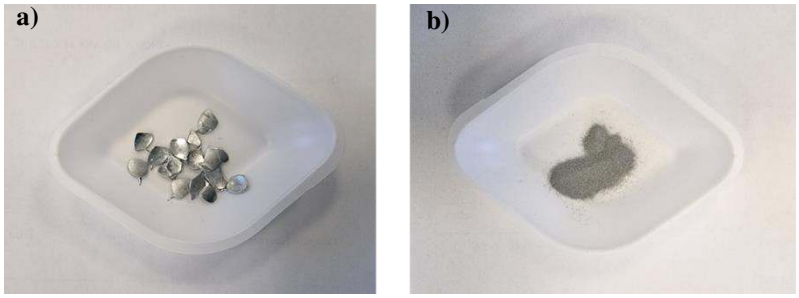


**Figure 3. 1** a) Small pieces of Zn (SPoZ), b) Zn powder.

In trials using Zn and Se in powder form as the starting material, it was possible to obtain ZnSe powder, which does not contain excess Zn, with a much shorter ball milling synthesis time. The most optimized results were obtained when one of the starting materials, Zn, was chosen in powder form. Optimization conditions and the abbrevitions of the samples formed by ball milling synthesis are given in Table 3.1.

**Table 3. 1** Synthesis conditions of ball milling method.

| Zn Form | Se Form | Duration (min) | Stochiometry Se:Zn | Ratio (MoR/MoB) | Excess material | Crytallite size (nm) | Sample name |
|---|---|---|---|---|---|---|---|
| Shots | Granular | 90 | 1:1 | 1:8 | - | - | SO1 |
| SPoZ | Granular | 150 | 1:1 | 1:8 | Zn | 9.22 | SO2 |
| SPoZ | Granular | 90 | 1:0.975 | 1:8 | Zn | 9.20 | SO7 |
| SPoZ | Granular | 120 | 1:0.950 | 1:8 | Zn | 8.72 | SO9 |
| SPoZ | Granular | 150 | 1:0.925 | 1:8 | - | 8.46 | SO12 |
| SPoZ | Granular | 210 | 1:0.950 | 1:5 | - | 8.12 | SO14 |
| Powder | Powder | 90 | 1:0.950 | 1:5 | Zn | 10.7 | SO28 |
| Powder | Powder | 150 | 1:0.950 | 1:5 | Zn | 9.92 | SO30 |
| Powder | Powder | 210 | 1:0.950 | 1:5 | Zn | 9.01 | SO31 |
| Powder | Powder | 270 | 1:0.950 | 1:5 | - | 9.12 | SO32 |
| Powder | Powder | 90 | 1:0.950 | 1:8 | Zn | 9.33 | SO46 at |
| Powder | Powder | 90 | 1:0.950 | 1:20 | - | 10.4 | SO46 ct |
| Powder | Powder | 60 | 1:0.950 | 1:8 | Zn | 8.61 | 2SO1 |
| Powder | Powder | 120 | 1:0.950 | 1:8 | - | 8.26 | 2SO2 |

It was observed that the Zn shots used as the starting material in the SO1 sample remained in bulk form at the end of the synthesis. The Se element has a somewhat brittle structure compared to the Zn. Therefore, there is no harm in using Se in granular form. However, it is not suitable to use Zn in the shot form for ball milling synthesis due to its soft structure. This is the reason why the Zn element is used in the SPoZ form.

As can be seen from Table 3.1, polycrystalline ZnSe obtained in powder form by ball milling synthesis has a crystallite size in the range of 8-11 nm. Se element is more volatile compared to Zn element and the melting point of Zn (419.5 °C) is higher than the melting point of Se (221 °C). For this reason, Se loss occurs during the synthesis. As can be seen from Table 3.1, excess Zn was observed in the synthesis performed at 1:1 stoichiometry.

In addition, ball milling time is an important factor for synthesizing ZnSe without excess Zn. At least 90 min is required for all the Zn element used in the synthesis to react with Se. Mass of reactants (MoR) / mass of balls ratio (MoB) is directly proportional to ball milling time in the synthesis of ZnSe that does not contain any excess element. Although reducing the MoR/MoB ratio significantly reduces the synthesis time, it does not make a significant contribution to the synthesis efficiency. Because reducing the MoR/MoB ratio also causes a decrease in the mass of ZnSe that can be synthesized in one trial.

Figure 3.2 shows the XRD patterns of ZnSe powder samples with synthesis conditions that are listed in Table 3.1.

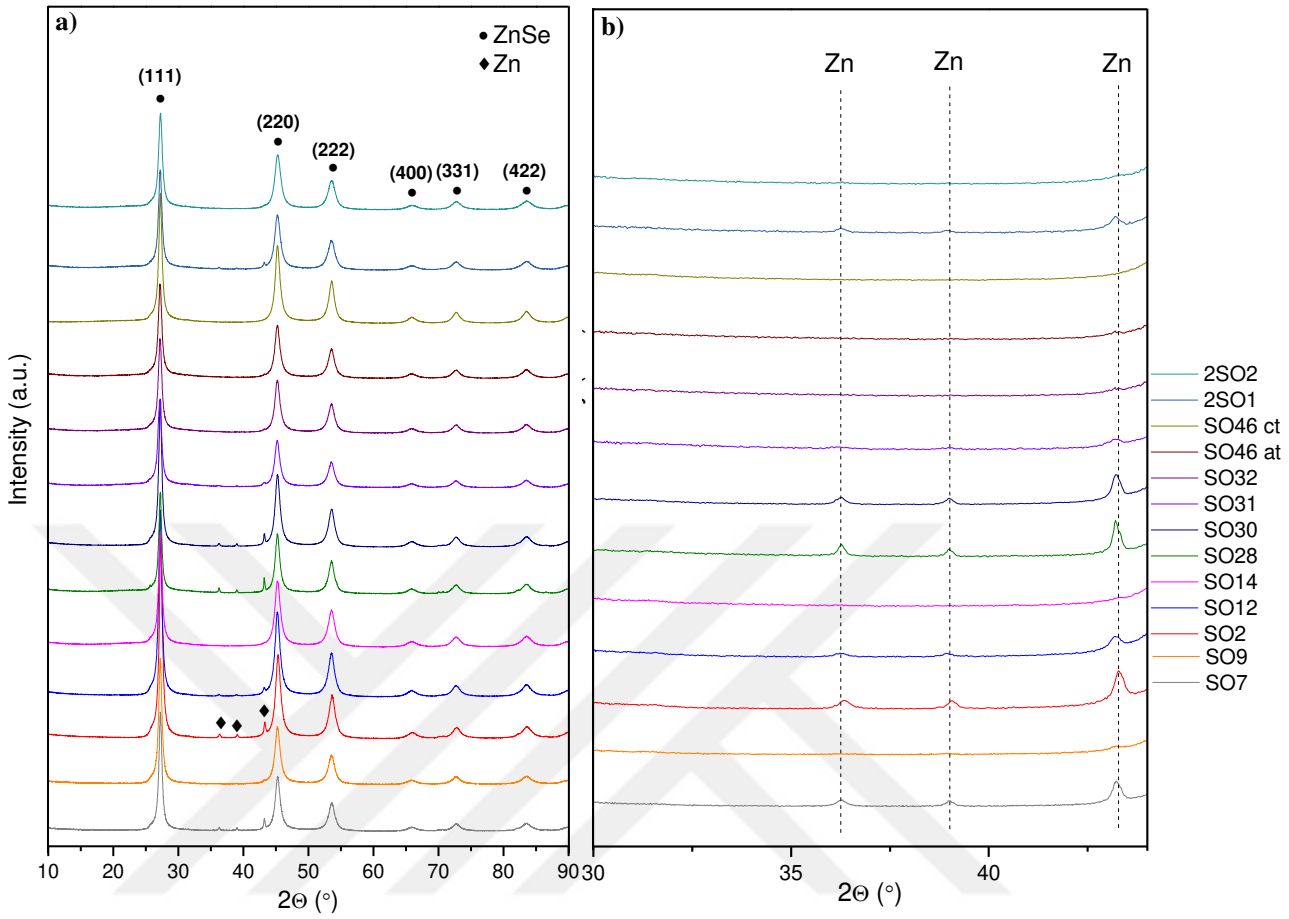


**Figure 3. 2** XRD graphs of the samples listed in Table 3.1 in the two-theta range of a) 10–90° and b) 30–48°.

The ZnSe peaks given in Figure 3.2 are indexed with PDXL software (COD ID: 1539324, space group $F\bar{4}3m$) and belong to the cubic crystal system of ZnSe ($a = b = c$ =5.65Å). Zn peaks are indexed with PDXL software (COD ID: 90112435, space group P63/mmc) and belong to the hexagonal close packed crystal system of Zn (a=b=2.46Å, c=4.93Å). According to Figure 3.2 and Table 3.1, the peaks located at 2θ=36.3°, 2θ =39.06°, and 2θ=43.2° angles confirm the presence of excess Zn in some samples. The crystallite sizes of the synthesized powder ZnSe materials were calculated with the Scherrer formula (Equation 8).

$$D_p = K\lambda/(B cos\theta) \qquad \text{Eq. 8}$$

Dp is the mean crystallite size in nanometers (nm), K denotes the Scherrer constant, λ is the X-ray wavelength, B denotes the Full Width at Half Maximum (FWHM), and is the peak location. Using the Scherrer formula, polycrystalline ZnSe synthesized by the ball milling method has a crystallite size of 8-11 nm.

For optical materials with high transmission values, the purity of the synthesized powder and its large grains are critical, as discussed in Section 1.4.2. The problem of excess Zn in already reacted ZnSe powder material has been handled by improving the ball milling synthesis conditions, as shown in Table 3.1.

- ***Purification process of the ZnSe powder***

When it comes to synthesizing bulk materials with high optical properties, one of the conditions that must be ensured is that the powder material to be sintered must be of very high purity. Therefore, the purity determined according to XRD measurements is not sensitive enough for optical materials. There are basically 2 reasons for this. The first is that the XRD technique cannot detect the amorphous structures in the matrix, and the second is that it cannot detect the inpurities in the material below about 2%. For this reason, heat treatment was applied to the samples synthesized by ball milling, regardless of whether they contain excess elements or not, both to eliminate elemental Se or elemental Zn impurities and to grow the grains before spark plasma sintering (SPS).

For the purification process, the powder ZnSe material obtained from the ball milling synthesis was loaded into a quartz tube in the glove box. Then, several heat treatment trials were carried out, either under Argon flow or under vacuum with the help of a tube furnace at 750 °C for 24 hours.

The reason for choosing the purification temperature of 750 °C is that this temperature remains above the melting point of both Se and Zn. However, this temperature is also above the boiling point of Se. For this reason, samples containing large amounts of elemental excess Se boil during the purification process. The viscosity of Se is high enough to burst the boiling bubbler. The small-scale explosion of the Se bubbles causes the ZnSe in powder form in the quartz tube to splash around. Therefore, one should be considered that during this process is that the amount of excess Se in the sample to be purified should not be too high.

In the samples purified under vacuum, excess Zn was oxidized even though the quartz was sealed under argon in glovebox. The XRD data of ZnSe samples containing ZnO phase after purification under vacuum are given in Figure 3.3.

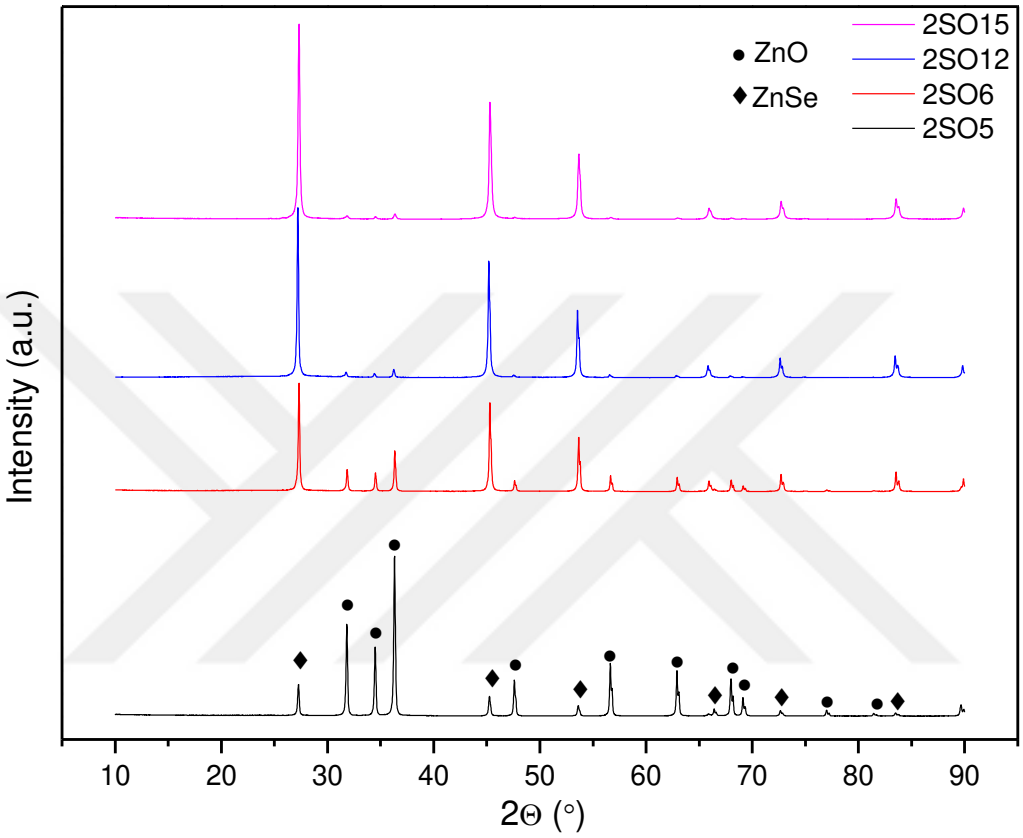


**Figure 3. 3** XRD patterns of the ZnSe powders that purified under vacuum

Since the oxidation temperature of the Zn element is at around 350 °C, it was observed that the excess Zn element was oxidized before the furnace temperature reached the purification temperature of 750 °C. The ZnO peaks given in Figure 3.3 are indexed with PDXL software (COD ID: 9008877, space group P6_3mc) and belong to the hexagonal crystal system of ZnO (a=b=3.24Å, c=5.20Å). As can be seen in Figure 3.3, the intensity of ZnO peaks changes according to the amount of excess Zn element contained in the purified ZnSe powder.

The appearance of the ZnO phase, as indicated above, shows that even a minor vacuum system leak will prevent the purification process from being used. As a result, the technique was repeated under argon flow.

Excess Zn in ZnSe was removed with an argon flowing system at a flow rate of about five bubbles/second. Figure 3.4 gives a picture of the quartz inside the tube furnace and the ZnSe powder that was synthesized by the ball milling method before and after purification.

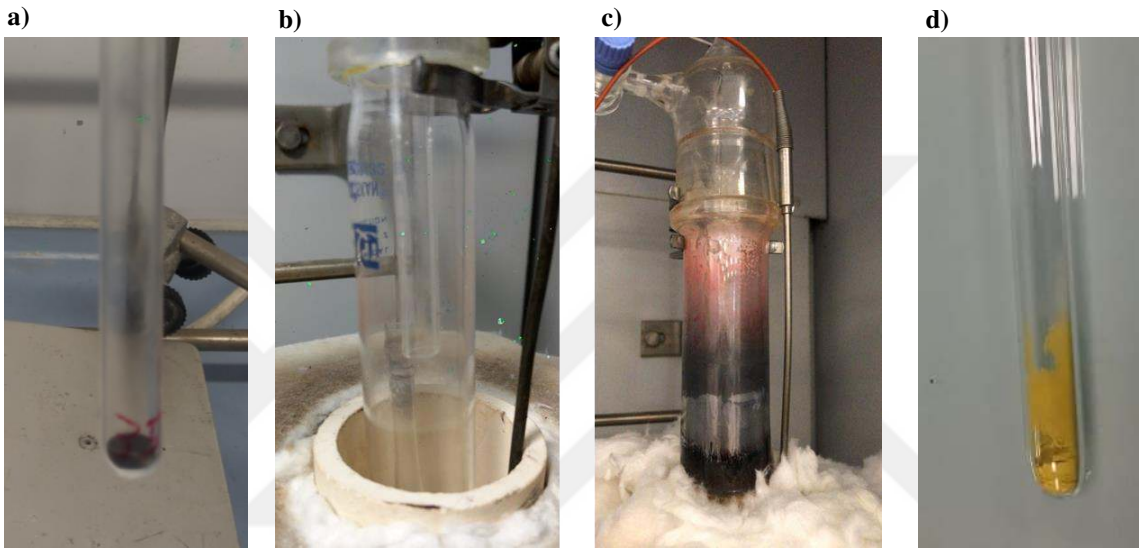


**Figure 3. 4** a) a picture of unpurified ZnSe powder synthesis via ball milling in quartz tube, b) a picture of quartz tube before heat treatment, c) a picture of quartz tube after heat treatment, and d) a picture of ZnSe powder in the picture a after purification process.

Figure 3.4c clearly shows that the excess elements evaporating from the ZnSe powder material synthesized by ball milling during heat treatment cover the surface of the quartz in the regions where the furnace temperature decreases. This situation turns the color of the sample illustrated in Figure 3.4a, which has a color in black tones, to yellow after purification as it should be (Figure 3.4d). However, the only factor that causes color change here is not the fact that the excess Se and Zn elements in the powder are evaporated. It is important to note that the color change is also influenced by the growth of grains in the powder ZnSe material during heat treatment.

In Figure 3.5, the XRD data measured before the purification process (bp) and after the purification process (ap) of SO2, SO28, SO30 samples synthesized with ball milling are given.

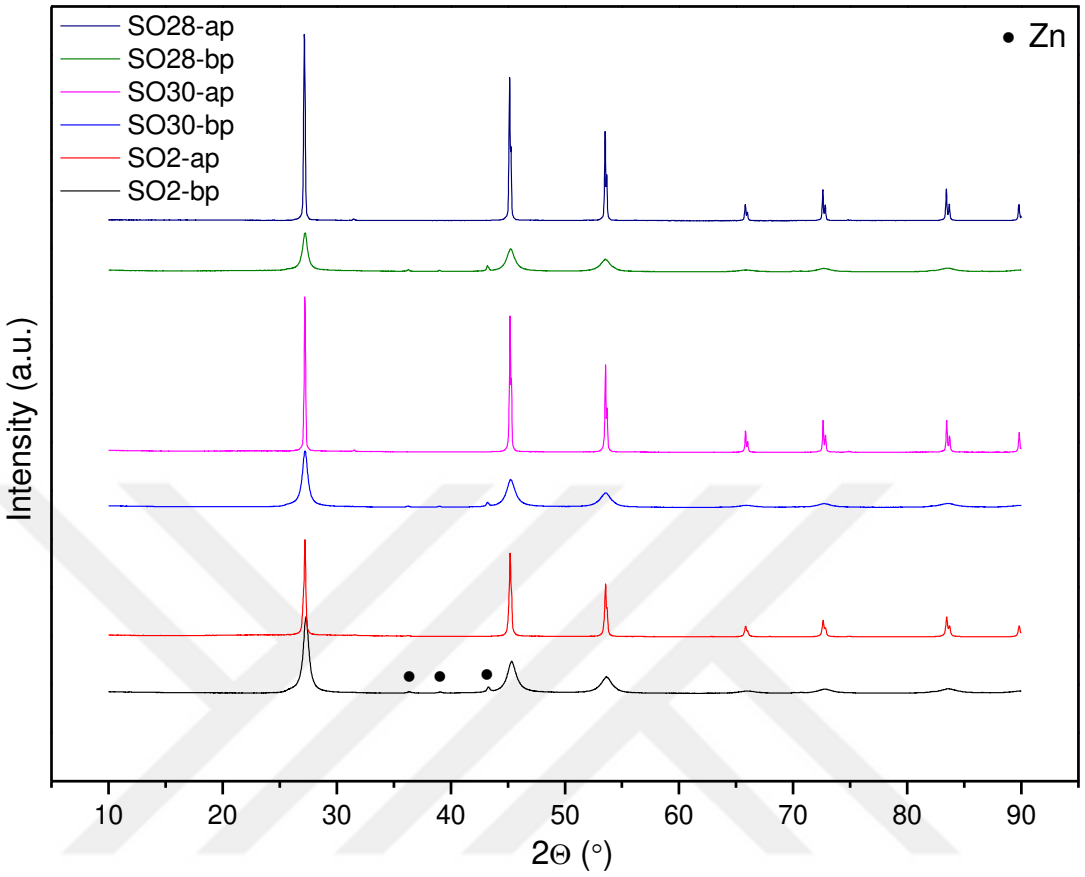


**Figure 3. 5** Before-after XRD patterns of the powder ZnSe via ball milling method.

In Figure 3.5, it is seen that the elemental Zn peaks disappeared after purification. It can be thought that the Zn peaks removed here are already very small, so there is no need for purification. However, it should be noted that in materials with excellent optical properties, the smallest impurity is a source of great loss for the light transmitting into the material.

The bulk material obtained by sintering ZnSe powder must have a large grain structure to have good optical properties. In fact, many optical materials fall into this category. For this, it is an advantage that the powder material to be sintered has large grains at the beginning. The purification process not only purifies the material but also ensures the growth of grains. SEM images of SO2, SO28 and SO30 samples purified under argon for 24 hours at 750 °C are given in Figure 3.6.

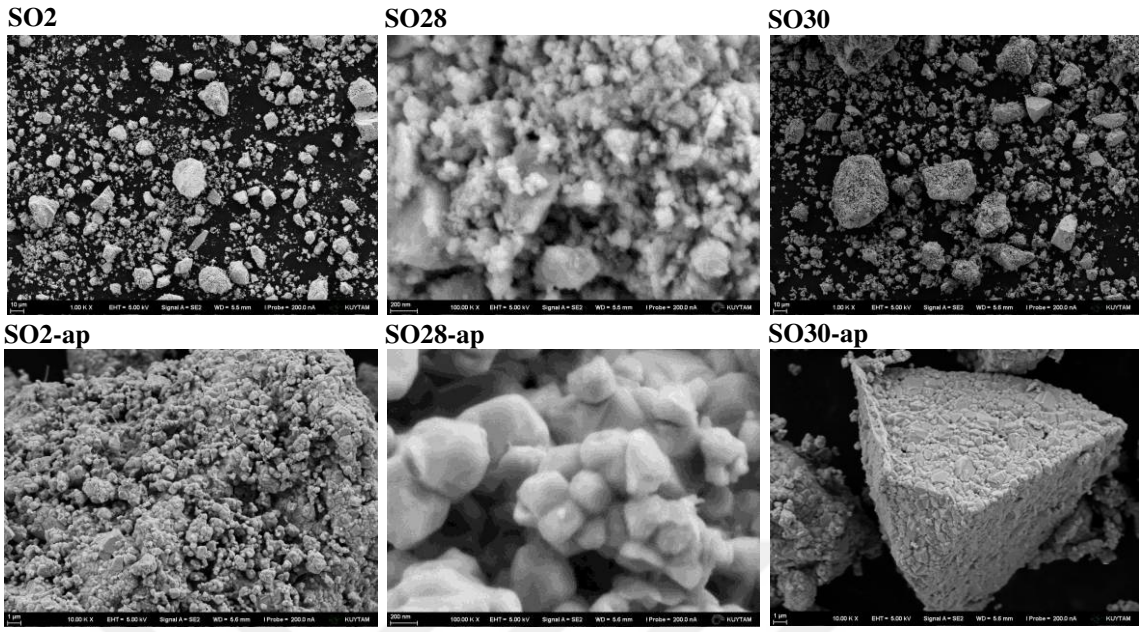


**Figure 3. 6** SEM images of the ZnSe powders synthesized via ball milling before-after purification process (ap indicates the sample after purification).

The ZnSe powder material synthesized by ball milling exhibits a wide range of distribution, as shown in Figure 3.6. The presence of powder particles ranging in size from 0.5 to 15 microns weakens the material's optical properties during the sintering stage. Although the sintered powder has a certain size distribution, which helps in uniform shrinkage and densification during sintering, a large range of dispersions, such as 0.5 μm and 15 μm, fall well short of providing this advantage. During sintering, powder with a wide particle size distribution has a lower relative density than powder with a narrow particle size distribution, according to studies [92, 93]. The mentioned wide-size distribution is one of the reasons why the ball milling process is not commonly used in the synthesis of materials with excellent optical properties.

When SEM images of SO28 and SO28-ap samples are compared in Figure 3.6, it is observed that purification process is very effective in grain size growth. In SO28 sample, this growth of grains from about 10 nm to 300 nm is about 30 times.

## *3.2 Co-precipitation Synthesis*

Co-precipitation method, which is a chemical synthesis method, is currently used in the synthesis of nano polycrystalline ZnSe material and in the synthesis of nano polycrystalline ZnSe doped with elements such as Ni, Cr, Fe, Co, Ti [94].

Although the number of studies on the sintering of polycrystalline ZnSe material, which is synthesized in powder form by the co-precipitation method, with SPS for optical applications is not very large, ZnSe windows with optical properties that can be considered good for laser applications have been successfully synthesized in several previous reports [33, 37, 95].

In this thesis study, nanocrystalline ZnSe powder was successfully synthesized using the synthesis conditions in the publications mentioned above. However, the ZnSe bulk material obtained after SPS is not transparent. The analyzes of the powder ZnSe material synthesized by the Co precipitation method and the pellet ZnSe material after sintering with SPS will be discussed in Section 3.4.2.

## *3.3 Solid State Synthesis*

Powder Zn (Sigma-Aldrich %99.99) and Se (Sigma-Aldrich %99.99) starting materials were mixed homogeneously with the help of mortar at 1:1 stoichiometry in the glove box, and then sealed in a quartz tube under $10^{-2}$ Torr vacuum. The sealed quartz tube was kept in the oven at 1000 °C for 21 days. The heating rate of the furnace was set to 10 °C/min and the cooling rate was set to 5 °C/min.

The advantage of the solid state method is that it is very simple and large amounts of samples can be synthesized in one batch. The disadvantages are the necessity of grinding the bulk sample obtained after synthesis to powder form, and the heterogeneous structure of the synthesized material when the starting materials Zn and Se powders are not prepared in a precise stoichiometry before the synthesis and the powder mixture cannot be ensured to be homogeneous enough. During the grinding process, there are risks of impurity and not having uniform size distribution of the powder material obtained. On the other hand, the reason for the heterogeneous structure observed in the synthesized bulk material is that the synthesis temperature is below the melting temperature of ZnSe. When Zn and Se, which are starting powder materials, are not mixed homogeneously before synthesis, thin ZnSe shell is formed at the boundaries

separating Se-rich and Zn-rich regions. Since this shell maintains its existence throughout the synthesis period, regions consisting of different phases may occur in the bulk ZnSe sample obtained after the synthesis. In Figure 3.7a, the heterogeneous structure that occurs when starting powder cannot be mixed homogeneously is given.

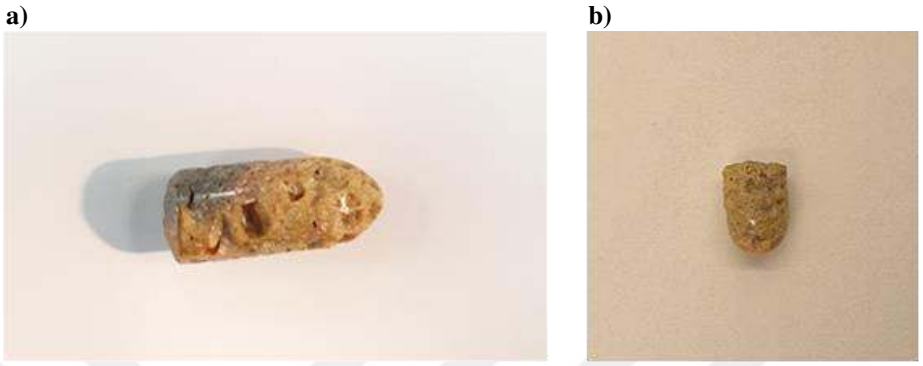


**Figure 3. 7** a) Heterogeneous structure of ZnSe bulk material and b) homogeneous structure of ZnSe bulk material after solid state synthesis.

As seen in Figure 3.7a, the black parts are the Se-rich region and the yellow parts are pure ZnSe. The formation of the aforementioned heterogeneous structure can be prevented by grinding Zn and Se starting powders very well in the glove box (Figure 3.7b). According to the experience gained as a result of the trials, the hand grinding time should be at least 20 min.

Samples synthesized by solid state method are given in Table 3.2.

**Table 3. 2** ZnSe samples synthesized via solid state method.

| Starting form[a] | Grinding time (min) | Structure | Crystallite size (nm) | Sample name |
|---|---|---|---|---|
| ZS, SS | - | - | - | SO1 |
| ZP, SP | 5 | heterogeneous | 84 | SO45-bp |
| ZP, SP | 10 | heterogeneous | 73 | 2SO24 (a, b, c) |
| ZP, SP | 20 | homogeneous | 75 | 2SO19 |
| ZP, SP | 20 | homogeneous | 65 | 2SO22 |
| ZP, SP | 20 | homogeneous | 79 | 2SO29 |
| ZP, SP | 20 | homogeneous | 81 | 2SO41 |

[a] The following abbreviations are used: Zn Shot (ZS), Se shot (SS), Zn powder (ZP), and Se powder (SP).

While preparing the SO1 sample, shot Zn (ZS) was used as the starting material. At the end of 21 days, it was observed that the ZS pieces retained their spherical form and the yellow ZnSe shell, which was mentioned before, was formed on their surfaces. For solid state synthesis, Zn element should be preferred in powder form.

While preparing the SO45-bp sample, Zn powder (ZP) and Se powder (SP) were used as starting materials. In the glove box, starting materials were mixed by grinding with the help of mortar for 5 minutes. It was observed that the sample, which was taken out of the furnace after 21 days, had a heterogeneous structure containing two colors, black and yellow. It is thought that 5 minutes of hand grinding carried out in the glove box is not sufficient for homogeneity.

In the 2SO24 sample, ZP and SP were used as starting materials. A heterogeneous structure including 3 different colors as yellow (2SO24-a), orange (2SO24-b) and slightly dark (2SO24-c) was observed as a result of 21 days of synthesis of the sample, which was mixed with the help of mortar for 10 minutes in the glove box. As in the SO45-bp sample, the grinding time of 10 minutes is not sufficient for homogeneity.

While preparing the 2SO19 and 2SO22 samples, the starting materials ZP and SP were mixed in the glove box for 20 minutes with the help of mortar. It was observed that 2SO19 and 2SO22 samples taken out of the furnace at the end of 21 days had a homogeneous structure. It seems that the crystallite size calculated using the Scherer formula is approximately 8 times larger when compared to the ball milling samples. This makes it easier to obtain bulk material with large grain size after SPS.

The color of the samples with different phases described above can be gathered under 3 main colors. These are black, orange, and yellow regions. Determining the source of these colors is important in terms of interpreting the optical properties of the bulk material to be obtained after SPS. This will be discussed in Section 3.3.2. Black, orange, and yellow samples are given in Figure 3.8.


**Figure 3. 8** Representative samples with different colors and phases.

### *3.3.1 XRD analysis of polycrystalline ZnSe synthesized via solid state method*

The samples taken out of the furnace in bulk form were ground in the glove box with the help of a mortar. XRD data were obtained for the structural characterization of the powders obtained as a result of this process. XRD measurements of ZnSe polycrystalline materials synthesized by solid state method are given in Figure 3.9.

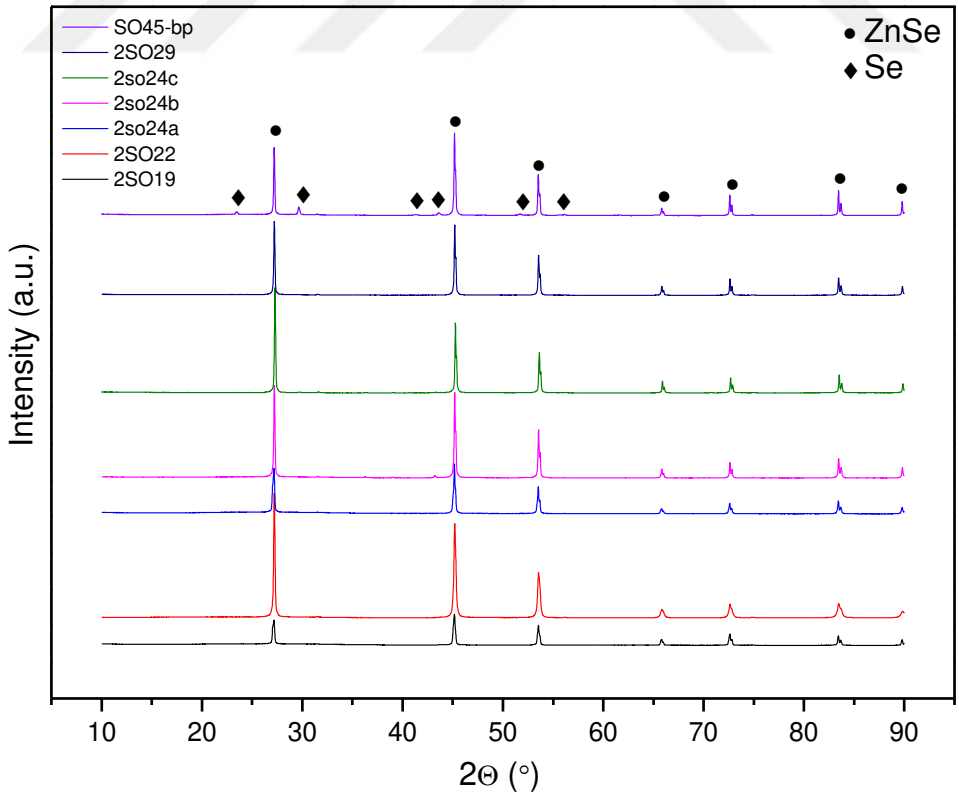


**Figure 3. 9** XRD graphs of ZnSe synthesized via solid state method.

According to Figure 3.9, it has been determined that the SO45-bp sample contains excess Se. This sample contained black parts like the sample given in Figure 3.7a. While a part of this black region and the orange part were ground together, XRD data was taken without applying the purification process. The presence of excess Se in the XRD data of the 2SO45-bp sample suggests that the cause of the heterogeneous black part is Se.

Slightly excess Se and excess Zn were found in the 2SO24b and 2SO24c samples. Because these samples have a heterogeneous structure incorporating various colors, it is reasonable to observe the elemental impurities of Se and Zn. The samples of 2SO19 and 2SO22 are homogenous and yellow in color. According to XRD data, they don't have any other phases than ZnSe.

### *3.3.2 SEM/EDX analysis of ZnSe polycrystallines synthesized by solid state method*

When it comes to synthesizing bulk materials with high optical characteristics, one of the parameters that must be achieved is the use of a very high purity starting powder material. As a result, the purity measured by XRD measurements is insufficiently precise for optical materials. This is due to two key factors. The first is that the XRD technique is unable to detect amorphous structures in the matrix, and the second is that it is incapable of detecting impurities below a certain percentage.

In the experiments, three different colors are observed in the heterogeneous structure, namely orange, yellow and black. The color of ZnSe material is yellow. In addition, XRD data of the yellow regions as a result of solid state synthesis gives pure ZnSe peaks. However, due to the limitations of the XRD technique mentioned above, it is crucial to confirm the presence or absence of excess Zn or Se by means of SEM/EDX. For this reason, EDX examinations of polycrystalline ZnSe materials synthesized by solid state method were carried out for more sensitive composition measurements. These studies were carried out on the crystals taken from the black, orange and yellow parts of the ZnSe material in bulk form. Composition analyses and EDX images of the crystals collected from the orange and black regions of the SO46 bp sample are given in Table 3.3 and Figure 3.10.

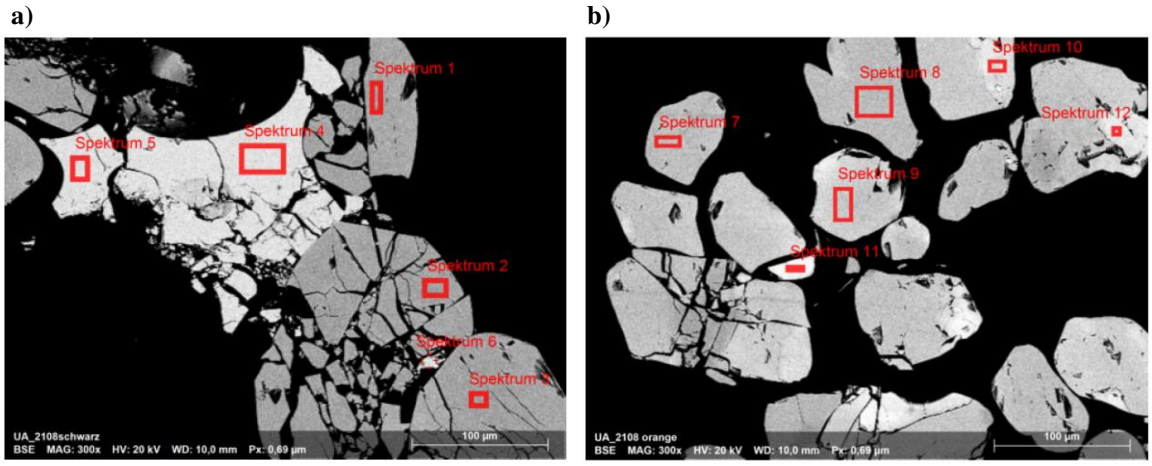


**Figure 3. 10** EDX regions for the crystals collected from a) black part and b) orange part of SO46-bp

**Table 3. 3** Atomic concentrations of black part of SO46-bp.

| Spectrum | C (at.%) | O (at.%) | Zn (at.%) | Se (at.%) |
|---|---|---|---|---|
| Spectrum 1 | 0.00 | 0.00 | 49.69 | 50.31 |
| Spectrum 2 | 0.00 | 0.00 | 50.05 | 49.95 |
| Spectrum 3 | 0.00 | 0.00 | 49.93 | 50.07 |
| Spectrum 4 | 0.00 | 0.00 | 1.09 | 98.91 |
| Spectrum 5 | 0.00 | 0.00 | 2.32 | 97.68 |
| Spectrum 6 | 0.00 | 0.00 | 5.11 | 94.89 |
| Mean | 0.00 | 0.00 | 26.37 | 73.63 |
| Sigma | 0.00 | 0.00 | 25.81 | 25.81 |
| SigmaMean | 0.00 | 0.00 | 10.53 | 10.53 |

In the SEM image given in Figure 3.10a, the EDX data from the bright regions represent Spectrum 4, 5, and 6 and data from darker regions represent Spectrum 1, 2, and 3. When Spectrum 4, 5, and 6 are examined in Table 3.3, it is observed that the region from which EDX data is taken consists of almost only Se atoms. According to the data from the other regions, the stochiometry of Zn and Se is 1:1. Considering that the color of the sample examined in Figure 3.10a is black, it is understood that a 25% shift of the stoichiometry to the Se side is enough to make the color of the sample black. Thanks to EDX analysis, it was confirmed that the reason for the black coloration that may occur in solid state synthesis is presence of Se.

In Figure 3.10b, the orange region taken from the SO46-bp sample was examined with EDX data from 6 different regions. The average of the concentration data taken from 6 different regions is given in Table 3.4. Since the standard deviation is relatively low in Table 3.4, it was not necessary to give the atomic concentration data of each spectrum. The EDX data of the orange crystal from the SO46-bp sample shows that it is in a highly precise stoichiometry.

**Table 3. 4** Atomic concentrations of the orange part of SO46-bp.

| | C (at.%) | O (at.%) | Zn (at.%) | Se (at.%) |
|---|---|---|---|---|
| Mean | 0.00 | 0.00 | 50.09 | 49.91 |
| Sigma | 0.00 | 0.00 | 0.66 | 0.66 |
| SigmaMean | 0.00 | 0.00 | 0.27 | 0.27 |

After identifying the composition of the orange and black colors by examining the EDX data of SO46-bp, the next step was to understand the composition of the yellow parts. For this purpose, the EDX and EDX-mapping measurements of 2SO22, which has a very homogeneous microstructure as shown in Figure 3.8, were made (Figure 3.11).

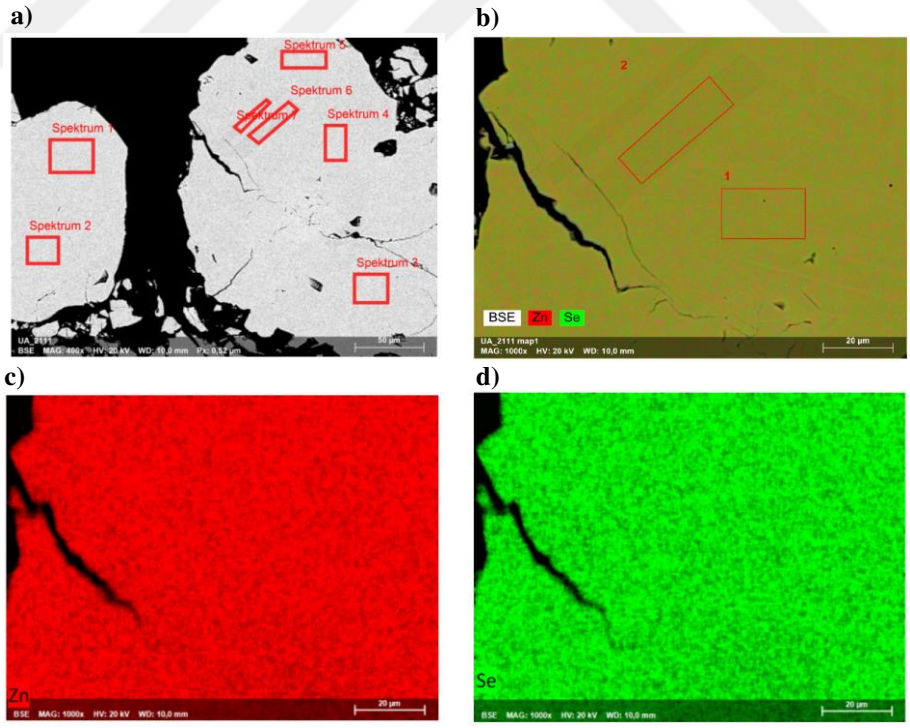


**Figure 3. 11 a)** EDX measurement regions, b) EDX-mapping regions of 2SO22, c) EDX map of (b) showing Zn, d) EDX map of (b) showing Se.

**Table 3. 5** EDX and EDX-mapping results of 2SO22.

| | C (at.%) | O (at.%) | Zn (at.%) | Se (at.%) |
|---|---|---|---|---|
| Map 1 | 0.00 | 0.00 | 49.75 | 50.25 |
| Map 2 | 0.00 | 0.00 | 50.03 | 49.97 |
| Mean value for 7 Spectrums | 0.00 | 0.00 | 50.16 | 49.84 |
| Sigma for the spectrums | 0.00 | 0.00 | 0.35 | 0.35 |
| SigmaMean for the spectrums | 0.00 | 0.00 | 0.13 | 0.13 |

When the concatration values given in Table 3.5 were examined, it was observed that the 2SO22 sample was as precise in terms of the Zn and Se stoichiometry as the orange crystals taken from the SO46-bp sample. As in the orange parts of 2SO22, SO46-bp provides a perfect stoichiometry of 1:1 for Zn:Se, as well. It suggests that the difference between yellow and orange color in the image given in Figure 3.8 may not be due to stoichiometry. Another option may be that there was a very small deterioration in the stoichiometry and we did not take measurements from these regions in the EDX measurements. In any case, it has been determined that the yellow and light orange samples obtained from solid state synthesis are good candidates for the SPS procedure.

## *3.4 SPS of Synthesized Polycrystalline ZnSe Powders Prepared by Various Methods*

In this section, the status of polycrystalline ZnSe samples synthesized by ball milling, co-precipitation, and solid state methods after SPS was discussed.

### *3.4.1 SPS of Ball-Milled Samples*

The samples synthesized by the ball milling method consist of two groups as purified and unpurified as described in Section 3.1.1. Regardless of whether unpurified ZnSe samples contain excess zinc, none of the bulk samples obtained after sintering with SPS show optical transmittance neither in the visible region nor in the infrared region.

Polycrystalline ZnSe in powder form synthesized by the ball milling method was loaded into a graphite die in a glove box. The powder loaded into the graphite die was insulated from the punchers and the graphite die body tby using 0.1 mm thick graphite sheets. All samples were sintered under 1 Pa vacuum.

The color of the sintered samples produced by ball milling becomes dark-gray or black at the end of the SPS process, as illustrated for the pellets in Figure 3.12. As a result of the sintering of the unpurified samples at high temperatures, the surface of the vacuum chamber of the SPS device was covered and contaminated with a dark-colored material. This contamination of the SPS chamber is attributed to the excess Zn in the material evaporating at high temperatures (above 750°C).

The relative densities of the bulk materials obtained as a result of the SPS process of unpurified samples were found to be low. This is because the elemental Zn evaporated from the material leaves a hollow structure behind. In Figure 3.12, images of powders before SPS and pellets after SPS are given.


**Figure 3. 12** Images of the unpurified powder ZnSe samples synthesized with ball milling method and their corresponding pellets obtained afterwards via SPS.

None of the sintered ZnSe pellet materials given in Figure 3.12 transmit white light and infrared light according to UV-vis and FTIR measurements, thus their data is not presented herein. The main reasons the pellets obtained were opaque were their low

density and their porous structure. Furthermore, the starting powder particles had very small grains (10 nm) and large size distribution. Here, the presence of excess Zn and wide size distribution of grain cause the sintered materials to be quite porous. Studies have shown that powder with wide particle size distribution has a lower relative density during sintering than powder with narrow particle size distribution [87, 88], which results in a decreased light transmission.

Excess Zn evaporates through the material during sintering and causes the material to have a porous structure, which is also believed to contaminate the surface of the SPS chamber in black. Finally, when the grain size is small, keeping the dwelling time very long is necessary to sinter a bulk material in the desired grain size. It is not possible for the grains to grow from 10-20 nm to 30-40 micrometers required for transparency at typical SPS periods such as 30 min, 60 min.

Purified and unpurified samples were sintered in different SPS conditions. Here, the most studied sintering parameter was the temperature. The SPS conditions of the sintered samples are given in the Table 3.6.

**Table 3. 6** Sintering conditions of SPS for unpurified and purified samples synthesized by ball milling method.

| Sample name | Heating rate (°C/min) | Cooling rate (°C/min) | Sintering Temperature (°C) | Dwelling Time (min) | Pressure (MPa) | Transmittance of white light |
|---|---|---|---|---|---|---|
| SO2-SPS | 30 | 50 | 650 | 30 | 60 | - |
| SO28-SPS | 30 | 50 | 1000 | 30 | 60 | - |
| SO30-SPS | 30 | 50 | 900 | 30 | 60 | - |
| SO2-ap-SPS | 30 | 50 | 650 | 30 | 60 | - |
| SO28-ap-SPS | 30 | 50 | 1000 | 30 | 60 | + |
| SO30-ap-SPS | 30 | 50 | 900 | 30 | 60 | - |

Among the samples given in Table 3.6, only the SO28-ap-SPS sample shows transmittance in both the visible and infrared regions. The only difference of SO28-ap-SPS sample, whose powder was purified prior to SPS, is its high sintering temperature. Specifically, it was sintered at 1000°C for 30 min. Although the SO28 and SO28-ap samples were sintered under exactly the same conditions, the SO28 sample shows no

transmittance either in the visible or IR regions. Therefore, the FTIR data of the SO28 sample is not given.

While the SO28-SPS sample sintered under exactly the same conditions does not transmit light, the transperant property of the purified SO28-ap-SPS sample proves the success of the purification process. As a result of the purification process, the main difference between these two samples is that the SO28-ap sample is a more pure powder and has larger grains, as it was shown in Figure 3.5 and Figure 3.6, respectively. Figure 3.13 shows the images of SO28 before purification (Figure 3.13a), after a purification for 24 h at 750°C under argon flow (Figure 3.13b) and after sintering by SPS (Figure 3.13c). Figure 3.13d further shows that the pellet obtained by purified SO28 transmits white light.

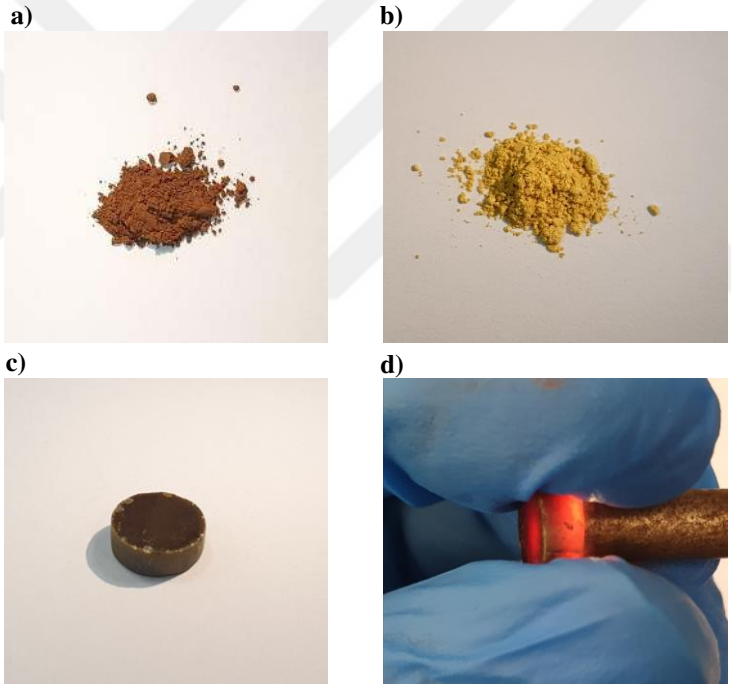


**Figure 3. 13** Images of SO28 a) before purification, b) after purification under argon (SO28-ap), c) after sintering of (b) via SPS, and d) transmission of white light through the SO28-ap-SPS.

As can be seen in Figure 3.13a and Figure 3.13b, the color of the SO28 sample changed from brown to yellow after purification. The most important reason for this is the growth of grains and the disappearance of impurities in ZnSe powder. It can also be seen in Figure 3.13d that SO28-ap sample transmits white light after sintering with SPS.

It is given in Figure 3.5 that SO2, SO28 and SO30 samples all contain excess Zn. Since SPS was made without removing the excess Zn contained in these samples with heat treatment, contaminations were detected in the vacuum chamber of the SPS device at the end of the sintering process of SO28 and SO30 samples. The reason for these contaminations, as mentioned before, is that the excess Zn element in the material evaporates and covers the surface of the vacuum chamber. In the SO2 sample, however, no Zn contamination was observed in the vacuum chamber. The reason for this is that SO2 is sintered at 650°C and this temperature is not sufficient for the evaporation of the excess Zn element in SO2.

Figure 3.14 provides the XRD spectra of the ball milled samples after sintering by SPS. Data shows that the crsytalline phases in all samples a pure ZnSe.

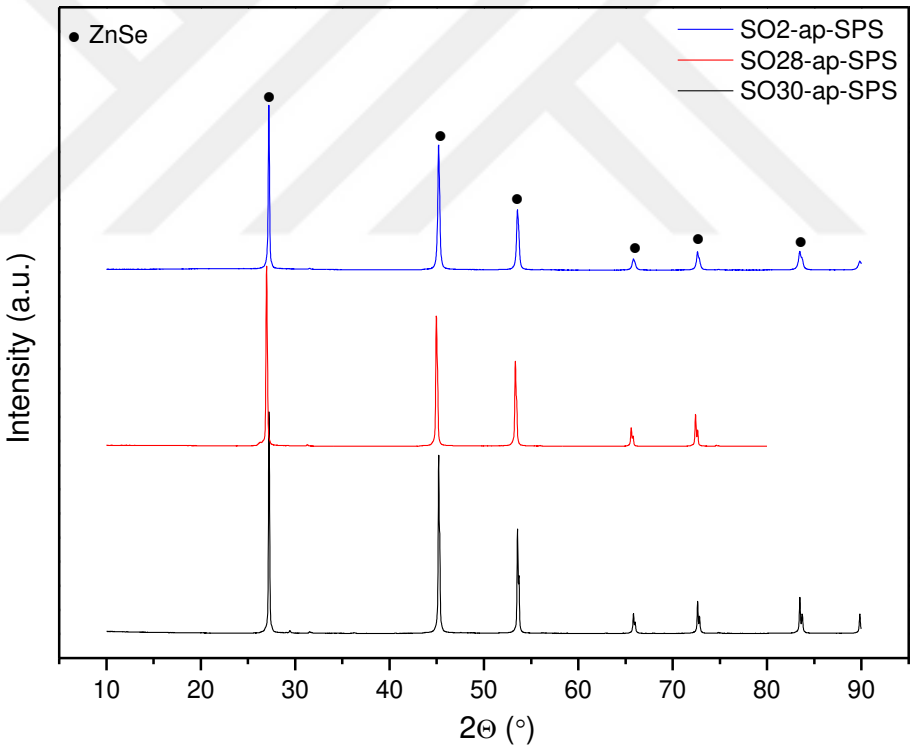


**Figure 3. 14** XRD graphs of purified samples measured after SPS.

As seen in Figure 3.13d among the samples in the after purification (ap) group, only the SO28 sample sintered at 1000 °C transmits light. The reason for this situation is that SO2 and SO30 samples were sintered at lower temperatures. SEM images of the

samples in the (ap-SPS) group were taken in order to examine the effect of sintering temperature on the microstructure. These images were taken from the cross-sections of the samples after they were crushed.

**a) SO2-ap-SPS** **b) SO30-ap-SPS**

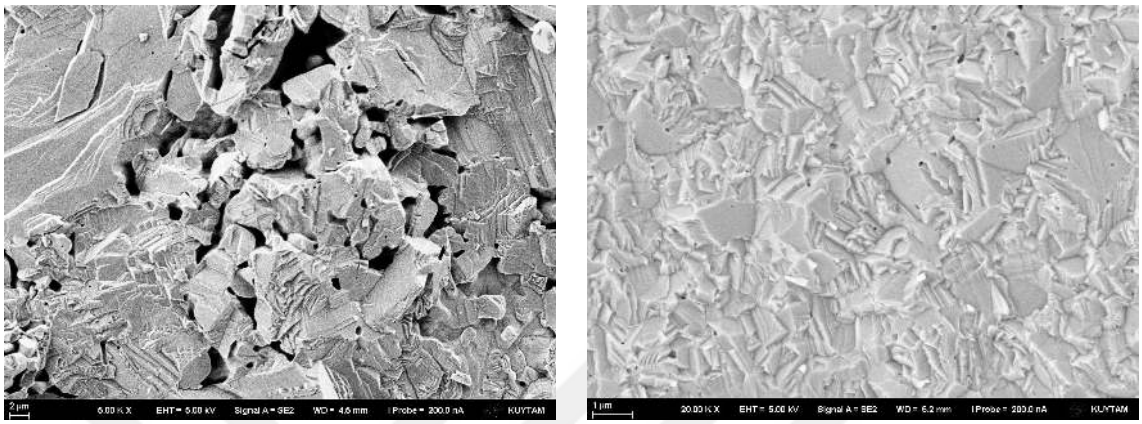

**c) SO30-ap-SPS** **d) SO28-ap-SPS**

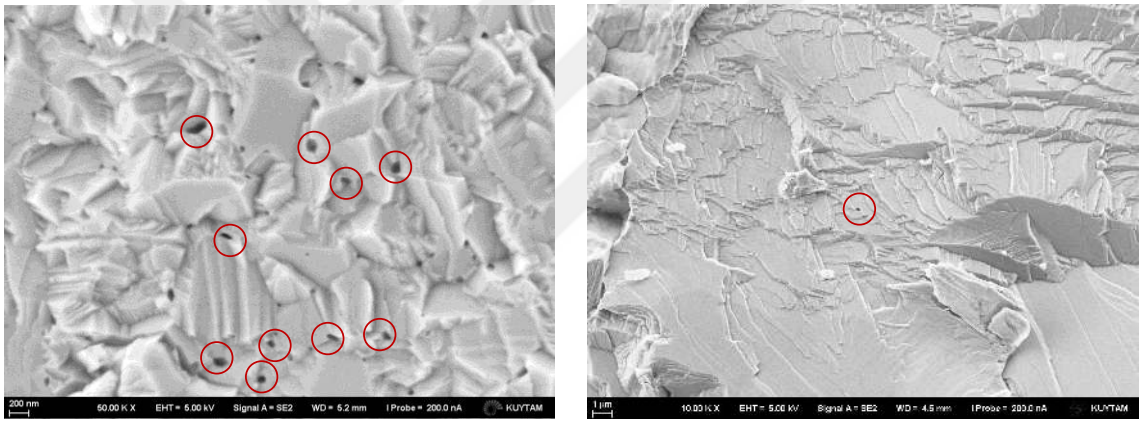

**Figure 3. 15** Fracture SEM images of samples a) SO2-ap-SPS, b)SO30-ap-SPS, c)SO30-ap-SPS, and d)SO28-ap-SPS.

As can be seen in Figure 3.15a, the sintering temperature of 650 °C applied in the SO2-ap-SPS sample was not sufficient for the grains to fuse and densification could not be achieved. Considering that grain fusing is one of the most important conditions for obtaining transparency in bulk ZnSe material, it is an expected result that this sample does not transmit light. Because the fact that it does not fuse grains results in a porous structure.

Grain fusing was provided in SO30-ap-SPS and SO28-ap-SPS samples (Figure 3.15b, c, and d). The SO30-ap-SPS sample sintered at 900 °C has a highly porous structure (Figure 3.15b, c). Since these pores cause high scattering of the light and decrease the relative density of the material, it significantly affects the transparency.

SO30-ap-SPS also does not exhibit transmission neither in the visible nor in the infrared regions.

SO28-ap-SPS was sintered at 1000 °C to obtain a material with both larger grain size and fewer pores, as illustrated in Figure 3.15d. The relative density values of these three samples are given in the Table 3.7.

**Table 3. 7** Densities of the ap-SPS group samples.

| Sample name | Density (g/cm$^3$) | Relative density |
|---|---|---|
| SO2-ap-SPS | 4.97 | %94,3 |
| So30-ap-SPS | 5.11 | %96.9 |
| SO28-ap-SPS | 5.18 | %98.2 |

As seen in Table 3.7, the sample with the highest density value is SO28-ap-SPS. SO28-ap-SPS sample is transparent both in the visible and infrared regions. It should be noted that this sample exhibits one of the best transparency among the pellets obtained from powders synthesized by ball milling in the literature.

FTIR measurements were performed to measure the wavelength-dependent transparency values of the SO28-ap-SPS sample (Figure 3.16).

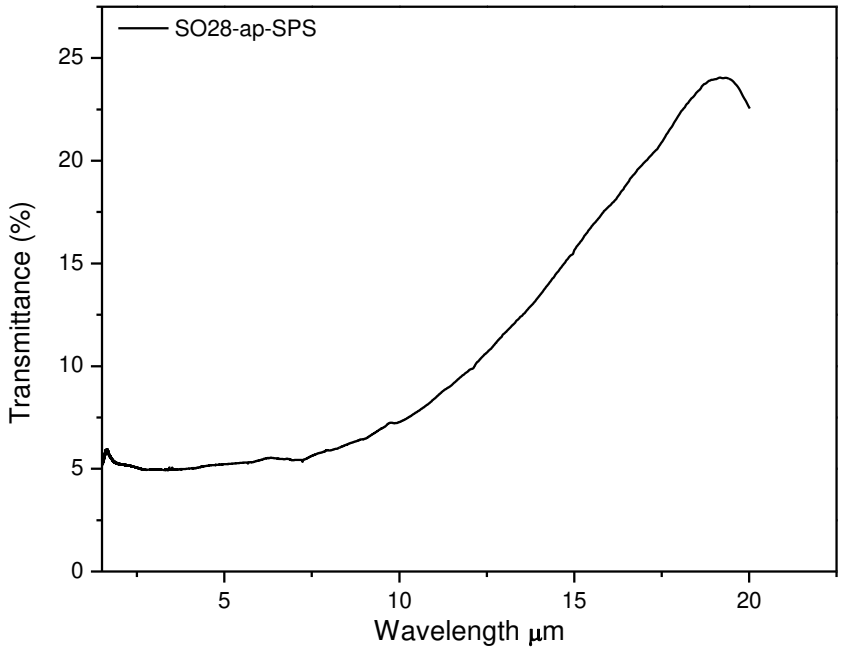


**Figure 3. 16** FTIR measurement of SO28-ap-SPS.

As seen in Figure 3.16, the SO28-ap-SPS sample has a transmittance value of 5% between 1.5-8 μm, and this value reaches up to 25% with increasing wavelength. The linear increase in transmittance value with increasing wavelength is characteristic for porous materials. Although these transmittance values are not sufficient for laser applications, they are among the highest values achieved among ZnSe materials synthesized by the ball milling method in the literature.

### *3.4.2 SPS of the ZnSe Powder Synthesized via Co-Precipitation*

The ZnSe powder obtained by co-precipitation method and after calcination (as explained in detail in Section 3.2) was loaded into the graphite die in the glovebox to be sintered with SPS. SO11-ac (after calcination) sample was isolated from graphite die and punchers with 0.1 mm graphite sheets.

The sample was sintered at a pressure of 60 MPa, at 1000 °C, at 2 Pa vacuum for 30 minutes. Heating rate was applied as 30 °C /min, cooling rate as 50 °C /min. After the process, the sample, which was removed from the graphite die, was sanded with 800 grid $SiO_2$ sandpaper. The density of the sample was calculated by using Archimeds methods as 5.26g/cm$^3$.

As seen in Figure 3.17, the color of SO11-ad sample is similar to the ZnSe colors obtained after ball milling synthesis. ZnSe in brown tones is characteristic of small grain microstructure. After SO11-ad sample was calcined at 400 °C for 6 hours, its color turned yellow as it should be (SO11-ac). After SPS, the color of the sample is dark gray, but it does not show transparency neither in the visible region nor in the infrared region.

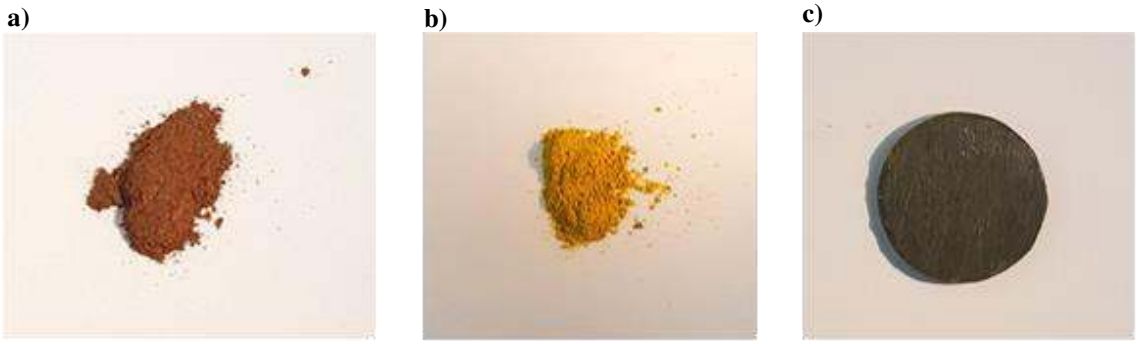


**Figure 3. 17** SO11 sample a) after drying in tube furnace (SO11-ad), b) after annealing in tube furnace (SO11-ac), c) after sintering (b) with SPS (SO11-aSPS).

The XRD data of the dried powder ZnSe (SO11-ad), calcined ZnSe powder (SO11-ac) and SPS sintered pellet ZnSe (SO11-aSPS) are given in Figure 3.18.

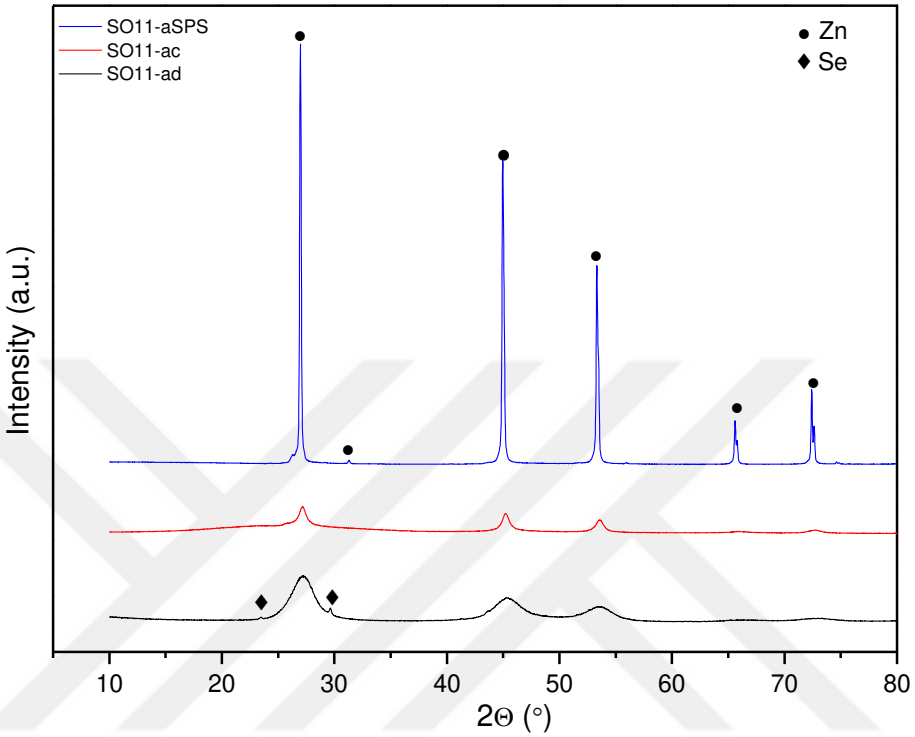


**Figure 3. 18** XRD graphs of SO11-aSPS, SO11-ac, and SO11-ad.

Excess Se was observed as an impurity only in the SO11-ad sample when the XRD peaks shown in Figure 3.18 were investigated. Although all of the other peaks belong to the ZnSe phase, the Se peak disappeared after calcining the SO11-ad sample at 400°C in a tube furnace. All peaks in the SO11-aSPS sample are ZnSe peaks. Additionally, it is seen that the XRD peaks are noticeably narrowed when the FWHM values are considered. This compression suggests an increase in the size of the crystallites. Table 3.8 contains the crystallite size calculated using the Scherrer formula.

**Table 3. 8** Crystalllite sizes of the ZnSe synthesized by co-precipitation method.

| Sample name | Crsytallite size (nm) |
|---|---|
| SO11-ad | 3.6 |
| SO11-ac | 12 |
| SO11-aSPS | 66 |

SEM images were taken to examine the microstructure of the SO11-aSPS sample sintered at 1000 °C. Figure 3.19a gives the surface view and Figure 3.19b, c and d fracture.

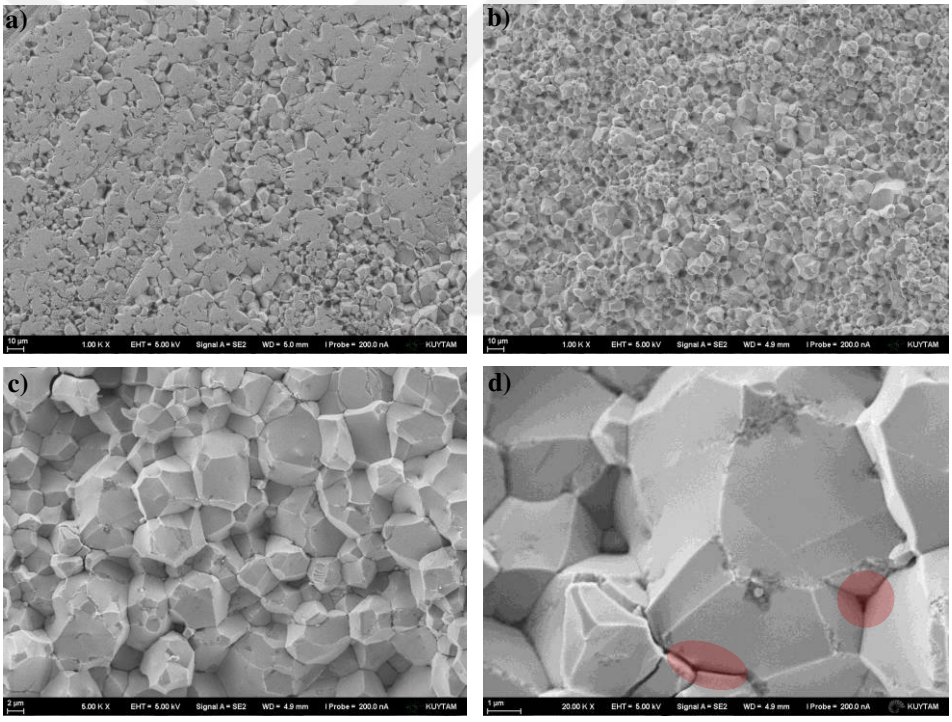


**Figure 3. 19** a) Surface SEM image, b, c and d) fractures SEM image of the SO11-aSPS.

As seen in Figure 3.19b, the average grain size of the sintered bulk material is below 10 µm. This value is below the 60–70 µm grain size value in commercial ZnSe windows. As seen in Figure 3.19d, a porous structure is observed between the grains and the gaps between the grain boundaries are high. It is known that such cavities work as scattering points in optical materials and adversely affect transparency values.

### *3.4.3 SPS of Polycrystalline ZnSe Synthesized by Solid State Method*

In this section, polycrystalline ZnSe material obtained as a result of solid state synthesis was brought into powder form with the help of a mortar in the glove box and SPS was applied. Among the samples given in Table 3.2, homogeneous ones were selected and it was ensured by XRD that the samples did not contain excess zinc or excess Se before sintering. The sintered samples selected were 2SO19, 2SO22, 2SO29, 2SO24-c. Although these samples are free of excess elements, they were subjected to purification at 750 °C for 24 hours after grinding. The reason for this is that the powder ZnSe to be sintered with SPS should have as large grains as possible. SPS conditions applied forthese samples are given in Table 3.9.

**Table 3. 9** SPS conditions of polycrystalline ZnSe synthesized via solid state method.

| Sample name | Heating rate (°C/min) | Cooling rate (°C/min) | Annealing Temperature (°C) | Dwelling duration (min) | Pressure (MPa) | Color of the pellet | Transmittance of white light |
|---|---|---|---|---|---|---|---|
| 2SO19-aSPS | 20 | 50 | 1000 | 30 | 70 | Brown | + |
| 2SO22-aSPS | 40 | 50 | 900 | 30 | 60 | Dark gray | + |
| 2SO22-$aSPS_2$ | 50 | 50 | 1000 | 30 | 90 | Black | + |
| 2SO29-aSPS | 10 | 20 | 1000 | 90 | 90 | Yellowish orange | + |
| 2SO24-aSPS | 7 | 20 | 1200 | 120 | 90 | Orange | + |
| 2SO24-$aSPS_2$ | 10 | 20 | 1100 | 90 | 90 | Dark orange | + |

Figure 3.20 illustrates the images of the samples whose SPS ocnditions are listed in Table 3.9. To make a proper comparison, each pellet was polished to obtain an equal thickness of 1mm.


**Figure 3. 20** Solid state ZnSe materials synthesized via solid state and sintered to form pellets by SPS.

It was previously stated in section 1.4.3 that one of the most important problems in material sintering with SPS is the possibility of carbon diffusing from the graphite die to the sample during the sintering process. Thus, the heating rate is reduced to prevent carbon diffusing. As can be clearly seen in Figure 3.20, 2SO19-aSPS, 2SO22-aSPS, and 2SO22-aSPS$_2$ samples sintered with high heating rate (20-50 °C/min) are in black, gray and brown tones, while when using a low heating rate (10 °C/min and 7 °C/min) the resulting samples (2SO29-aSPS, 2SO24a-SPS2 and 2SO24-aSPS) are yellow in color. The reason for this situation is attributed to the carbon diffusing.

Besides, to understand the effect of carbon diffusing during sintering, additional SPS expeirments were performed on 2SO22 whose details are provided in Table 3.10. The resulting samples by applying various SPS conditions to 2SO22 are illustrated in Figure 3.21. The significantly lower heating rate in 2SO22-O sample (10 °C/min) compared to 2SO22-G sample (50 °C/min) was chosen to see the effect of heating rate on carbon diffusing.

The resulting dark-colored pellets were used to perform EDX and CHSN-O analysis, which however did not provide satisfying results to comment on the existence of carbon in the pellets.

**Table 3. 10** Sintering conditions of 2SO22.

| Sample name | Heating rate (°C/min) | Cooling rate (°C/min) | Sintering temperature (°C) | Dwelling duration (min) | Pressure (MPa) | Color |
|---|---|---|---|---|---|---|
| 2SO22-G | 50 | 50 | 1000 | 15 | 60 | Dark gray |
| 2SO22-O | 10 | 50 | 1000 | 15 | 60 | Dark orange |

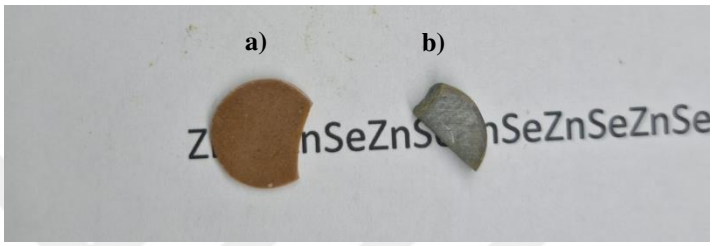


**Figure 3. 21** Image of a) 2SO22-O and b) 2SO22-G.

According to Figure 3.21, by only changing the sintering heating rate of the same starting powder material, the color of the pellet is significantly affected. Accordingly, the color of the sample sintered with low heating rate is yellow (2SO22-O), and the color of the sample sintered with high heating rate is black (2SO22-G). Besies, the heating duration is also an important factor. The image of 2SO22-a$SPS_2$ iluustrated in Figure 3.20 has a higher heating duration (30 min) than those shown in Figure 3.21, which results in an even darker color. Another factor is that 2SO22-a$SPS_2$ was sintered at 900 °C, which seem to decrease the grain growth, which is another factor decreasing the tranparancy as discussed already above.

After some of these samples were broken and ground in the glovebox to perform XPS to 2SO22-O and 2SO22-G in order to comment on their carbon content. XPS of the C 1s, O 1s, Zn 2p, and Se 3d regions are given in Figure 3.22.

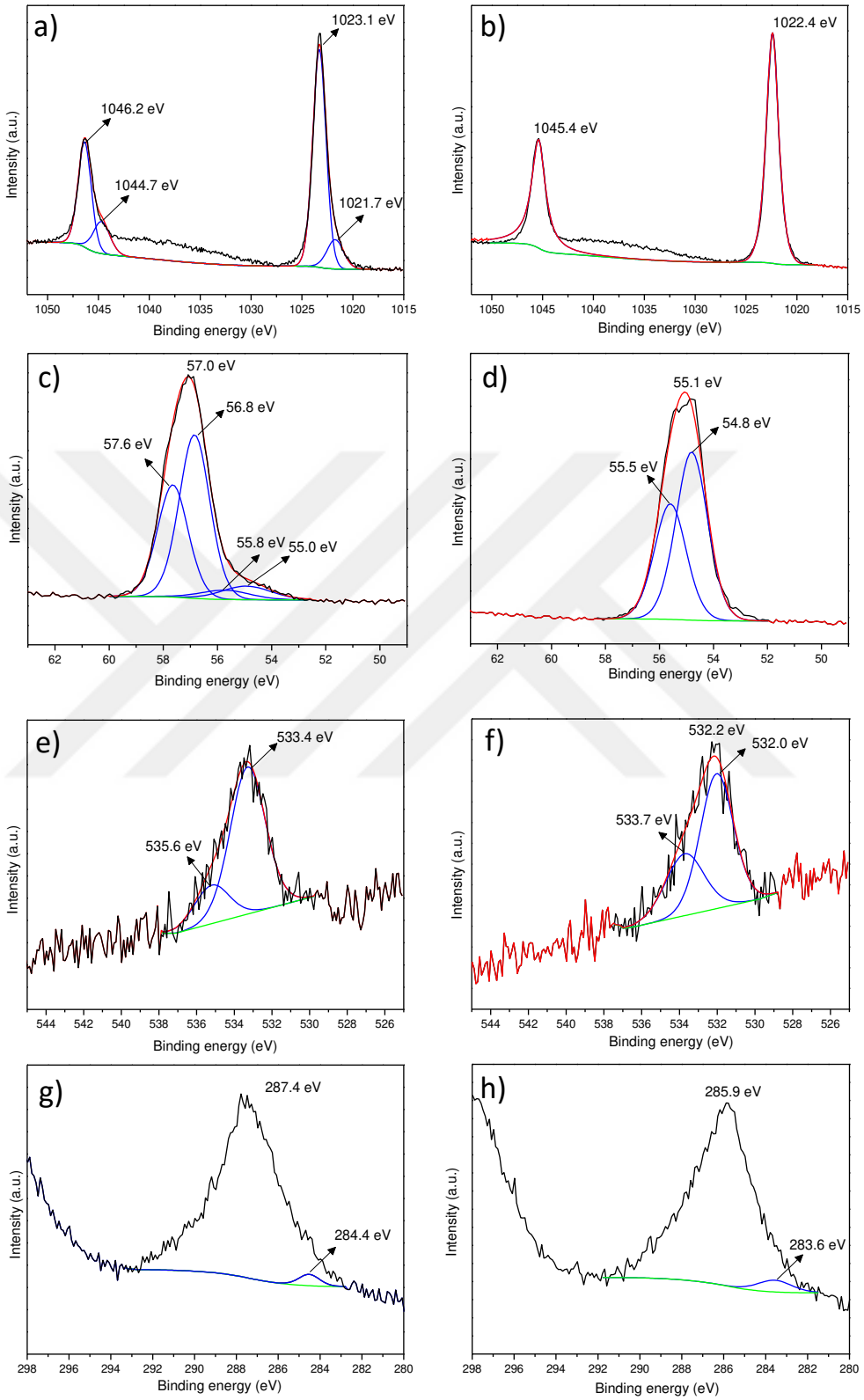


**Figure 3. 22** XPS spectra in the a) Zn 2p, c) Se 3d, e) O 1s, g) C 1s regions of 2SO22-O and b) Zn 2p, d) Se 3d, f) O 1s, h) C 1s regions of 2SO22-G.

Peaks at 1023.1 and 1046.2 eV in 2SO22-O (Figure 3.22a) and peaks at 1022.4 and 1045.4 eV in 2SO22-G (Figure 3.22b) are attributed to the Zn $2p_{3/2}$ and Zn $2p_{1/2}$ which corresponds to $Zn^{2+}$ in ZnSe [96]. The Zn 2p region of 2SO22-O was deconvoluted into two main features (Figure 3.22a). One possibility might be the presence of Zn oxides. However, as the $Zn^{2+}$ of ZnSe and ZnO provide peaks at almost the same binding energies [96, 97], it was not possible to comment on the peaks at 1044.7 and 1021.7 eV.

Deconvolution of the Se 3d region resulted in two features in Figure 3.22c for 2SO22-O while only one feature appears for 2SO22-G (Figure 3.22d). The absence of peaks in the region of 58–61 eV in both samples Se 3d region confirms the absence of $SeO_2$ [98]. The peaks at 55.8 and 55.0 eV in 2SO22-O and 55.5 and 54.8 eV in 2SO22-G in the Se 3d region is attributed to the Se 3d doublets of ZnSe [98, 99]. It is known that the Se 3d doublets of bulk selenium ($Se^0$) is at a higher binding energy than the Se in ZnSe. Thus, the intense peaks at 57.6 and 56.8 eV in the Se 3d region of 2SO22-O are assigned to $Se^0$ (Figure 3.22c), which are similar to those obtained by Chaparro et al. [98] and Deng et al. [99]. This shows that in 2SO22-O some excess Se is remained in the sample.

The absence of the formation of metal oxides could be also confirmed by investigating the O 1s spectra of 2SO22-O and 2SO22-G (Figure 3.22 e and f). The peaks located at relatively high binding energies, such as 535.6 and 533.4 eV, in 2SO22-O was attributed to adsorbed $H_2O$ an surface OH groups [98, 100], while no metal–O feature could be found which is expected to be located at around 530.0 eV [100]. This finding is in alignment with the O 1s region of 2SO22-G, as well. It can be concluded that, according to O1s spectra of both samples, no metal oxide formation took place.

The broad peak in the C 1s region of 2SO22-G and 2SO22-O which are located at 287.4 and 285.9 eV, respectively, were deconvoluted for both samples (Figure 3.22 g an h). However, one important point is that this region is dominated by the peaks of Se and the peaks of C and Se overlap. Therefore, to clarify the deconcoluted peak belonging to carbon in our samples (284.4 eV for 2SO22-O and 283.6 eV for 2SO22-G), the deconvoluted Se peaks in the C 1s spectra were not shown. Furthermore, the most important reason for the XPS analysis was to investigate the effect of carbon presence on the color of the samples. Thus by using the area of the deconvoluted peaks, the

carbon content could be determined. So that the Se peaks in the C 1s region do not contribute to the overall peak area, the C 1s region's Se peaks were not considered.

Accordingly, by taking into account all deconvoluted peaks the carbon content of 2SO22-O (which was yellow/orange in color) was 2.5 at.% whereas that of 2SO22-G (which was dark gay in color) was 3.6 at.%. This suggests that, the pellet which is dark gray in color has a higher carbon content, which seems to be the reason for its darker color, which aligns well with previous data [91]. Even though the 2SO22-O had excess Se, it did not had any affect on the dark coloring of the sample.

The structural characterization by XRD of the samples for which their SPS conditions were provided in Table 3.9 are given in Figure 3.23. No pure Zn or Se impuritiues was observed in the XRD spectra of the samples and only ZnSe was observed (Figure 3.23)

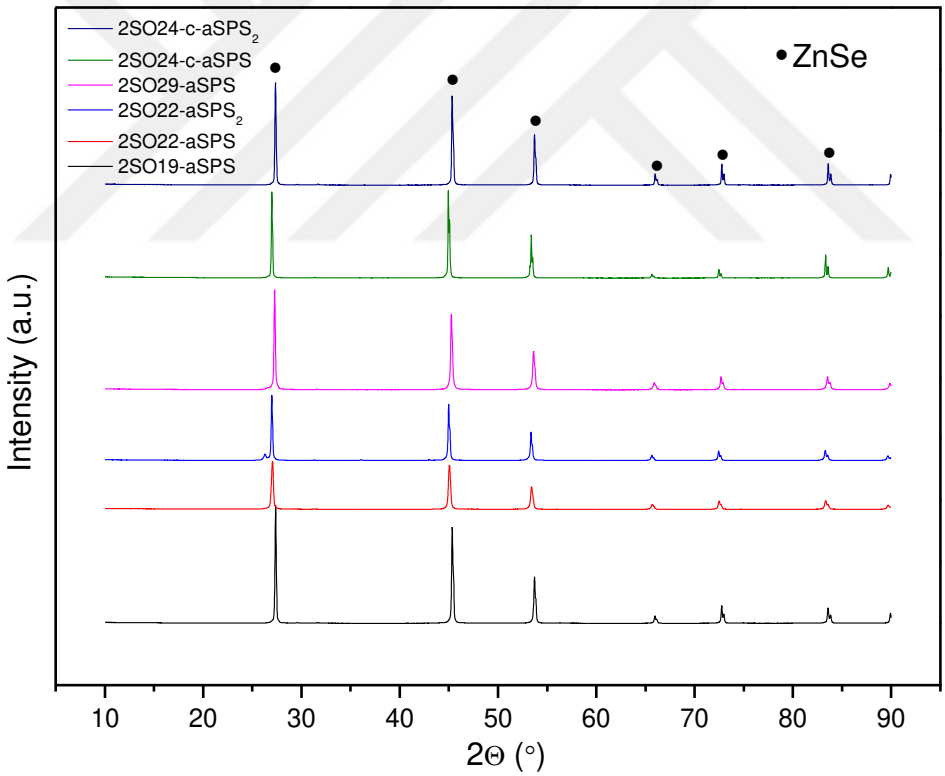


**Figure 3. 23** XRD measurements of the sintered ZnSe powder samples synthesized via solid state.

To analyze the microstructure of the fracture of the pellets, broken pellet pieces were analyzed by SEM which are provided in Figure 3.24.

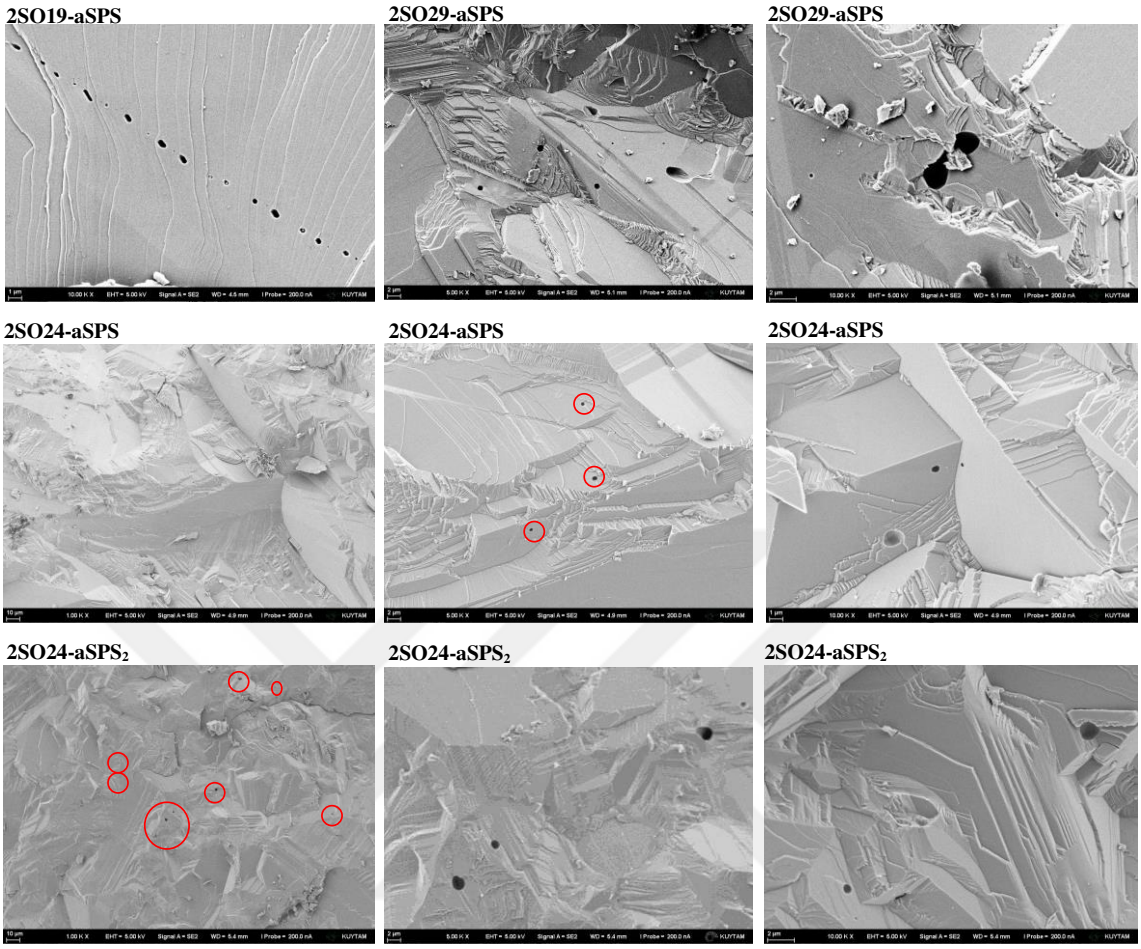


**Figure 3. 24.** SEM images of the pellet samples whose sintering parameters were provided in Table 3.9.

Among the samples analyzed in Figure 3.24, the most porous sample was found to be 2SO19-aSPS followed by 2SO29-aSPS. Furthermore, 2SO29-aSPS exhibits reltively large pores. On the other hand, the SEM images with the lowest porosity belong to 2SO24-aSPS and 2SO24-aSPS$_2$ The samples with the largest pores are 2SO24-aSPS$_2$ and 2SO29-aSPS. On the other hand, it was observed that fusing took place and there were no granular grains in all samples given in Figure 3.24. Considering the sintering conditions given in Table 3.9, it is seen that the pore density is inversely proportional to the temperature. For example, when 2SO24-aSPS made with SPS at 1200°C, 2SO24-aSPS$_2$ with SPS at 1100°C, and 2SO29-aSPS with SPS at 1000°C are compared, it is seen that both pore density and pore sizes decrease with increasing temperature.

In order to determine the transmission, FTIR measurements of 2SO24-aSPS2, 2SO24-aSPS, 2SO29-aSPS, 2SO19-aSPS samples were measured (Figure 3.25).

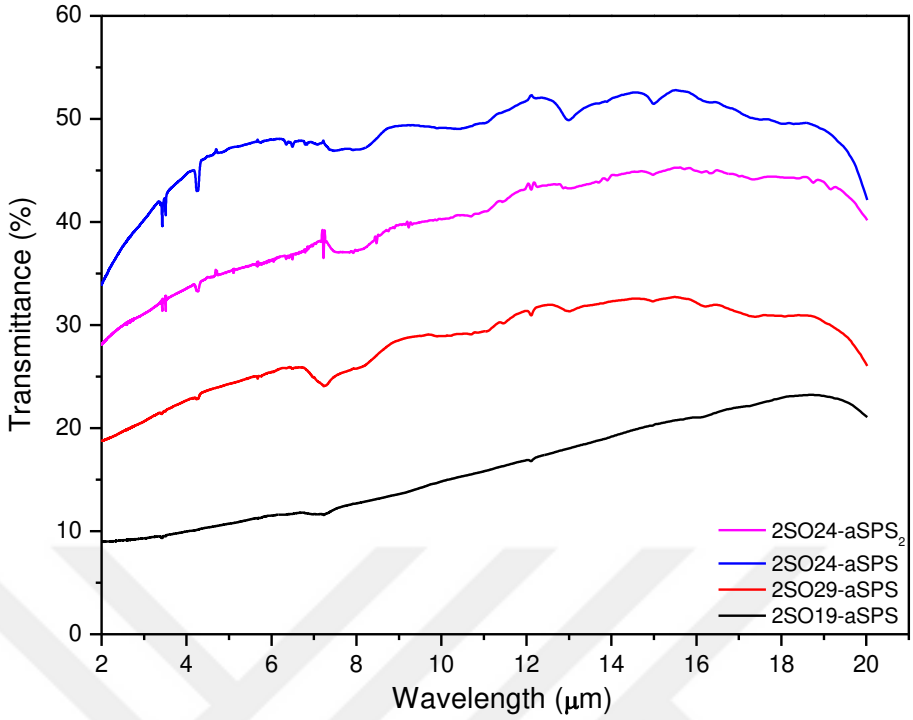


**Figure 3. 25** FTIR spectra of sintered ZnSe synthesized via solid state method

In homogeneous ceramic materials, transmission (T) can be expressed as given in Equation 8, depending on the thickness of the material.

$$T = exp^{-\alpha\chi} \qquad \text{Eq 8}$$

Here, α is the linear attenuation coefficient and χ is the thickness of the material. In this thesis, χ=1mm for the transmission values of all samples measured with FTIR.

The sample with the highest transmission according to the FTIR spectrum is 2SO24-aSPS2. Considering Figure 3.24, it is noteworthy to mention that the number of pores contained in the bulk ZnSe material is inversely proportional to the transmission. On the other hand, the increase in the frequency of large pores in the material affects the transmission negatively. Considering Table 3.9, the highest transmission values in Figure 3.25 were obtained in the 2SO24a-SPS sample, which was sintered at 1200 °C temperature and 90Mpa pressure, at 7 °C/min heating rate for 120 min.

## *3.5 Single Crystalline ZnSe Synthesis by Chemical Vapor Transport*

Two-zone furnaces were used to grow single-crystal ZnSe with the CVT method, the details of which are given in sections 1.4.4 and 2.1.6. No seed crystal was used to grow the crystals on it. Polycrystalline ZnSe synthesized by solid state method was used as source material in the CVT method.

ZnSe bulk material synthesized with solid state, which was turned into powder in the glove box by hand grinding method, was loaded in a quartz tube in the glove box. $ZnCl_2$ used as a transport agent was loaded into a thinner and shorter quartz tube. The aim here was to hinder the contact between the transport agent and the source material. Quartz loaded with $ZnCl_2$ was placed into the quartz loaded with ZnSe as presented in Figure 3.26.


**Figure 3. 26** Quartz tube prepared to be placed in a two zone furnace.

The quartz illustrated in Figure 3.26 was sealed in a sealing station to be placed in a two-zone furnace under $10^{-2}$ Torr pressure. The heat profile of the two zone furnace used was determined for different heat gradients. While deciding the heat profile, temperature data was recorded every 0.5 cm by using a 150 cm long thermocouple (Figure 3.27).

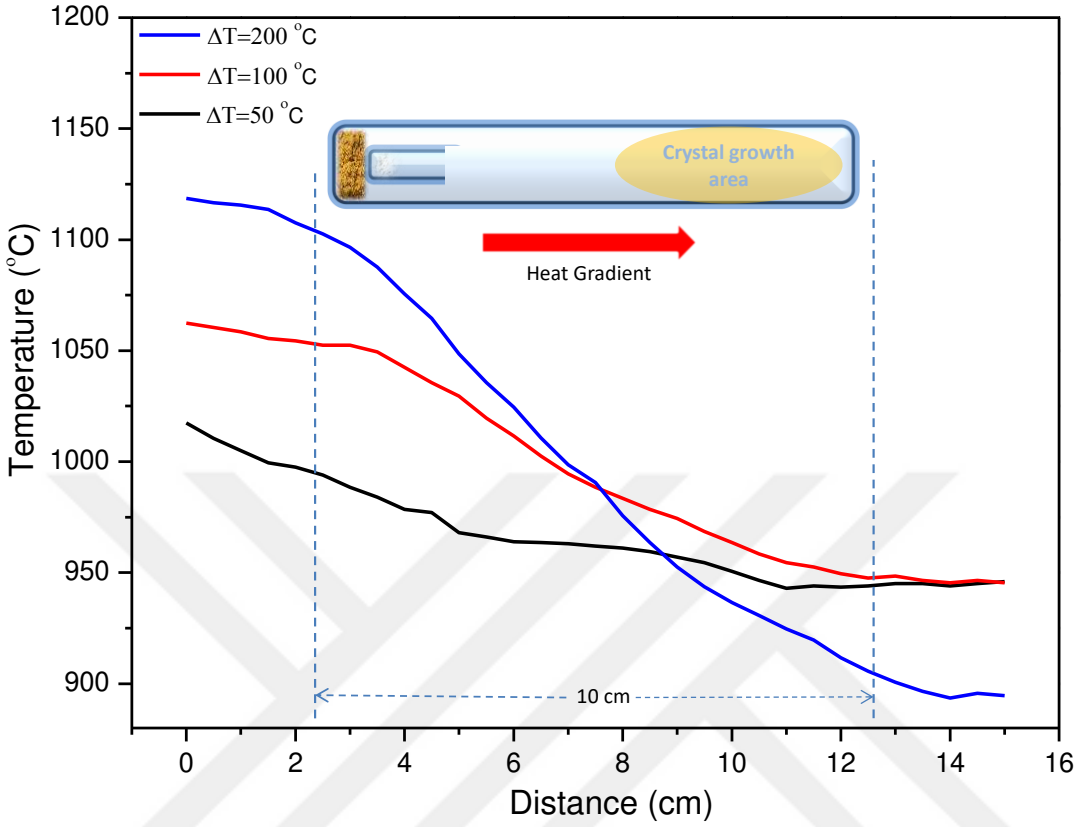


**Figure 3. 27** Heat profile of two zone furnace at three different heat gradients having various ΔT values, where ΔT corresponds to the temperature difference between the starting point and end point of the quartz tube.

In Figure 3.27, heat gradient was given in the area where the sealed 10 cm long quartz tube was placed, and single-crystal growth experiments were carried out using different amounts of transport agents under three different heat gradients. Since the mass of transport agent/volume of quartz tube (MoTA/VoQ) ratio is important in single-crystal growth, they are listed in Table 3.11 together with the experimental conditions.

**Table 3. 11** Single-crystal growth conditions.

| Sample name | Source material (g) | Heat gradient (°C) | Amount of transport agent (mg) | MoTA/VoQ (mg/cm$^3$) | Transport |
|---|---|---|---|---|---|
| 2SO27 | 1 | 50 | 25 | 2.21 | - |
| 2SO31 | 1 | 100 | 50 | 4.42 | + |
| 2SO32 | 1 | 100 | 75 | 6.63 | + |
| 2SO33 | 1 | 100 | 100 | 8.84 | + |
| 2SO35 | 1 | 200 | 50 | 4.42 | + |
| 2SO38 | 1 | 200 | 75 | 6.63 | + |
| 2SO39 | 1 | 200 | 100 | 8.84 | + |
| 2SO40 | 1 | 200 | 200 | 17.69 | + |

For all of the trials listed in Table 3.11, a 10 cm long quartz tube with a 12 mm inner diameter was used. The synthesis duration was set as 7 days in all of the trials. The heating and cooling rates were both set to 5 °C/min.

Although the formation of ZnSe single-crystals of different sizes was observed in all samples except for the 2SO27 sample, the size of the crystals increased with increasing heat gradient and increasing amount of transport agent. Photographs and images of the synthesized samples under optical microscope are given in Figure 3.28.

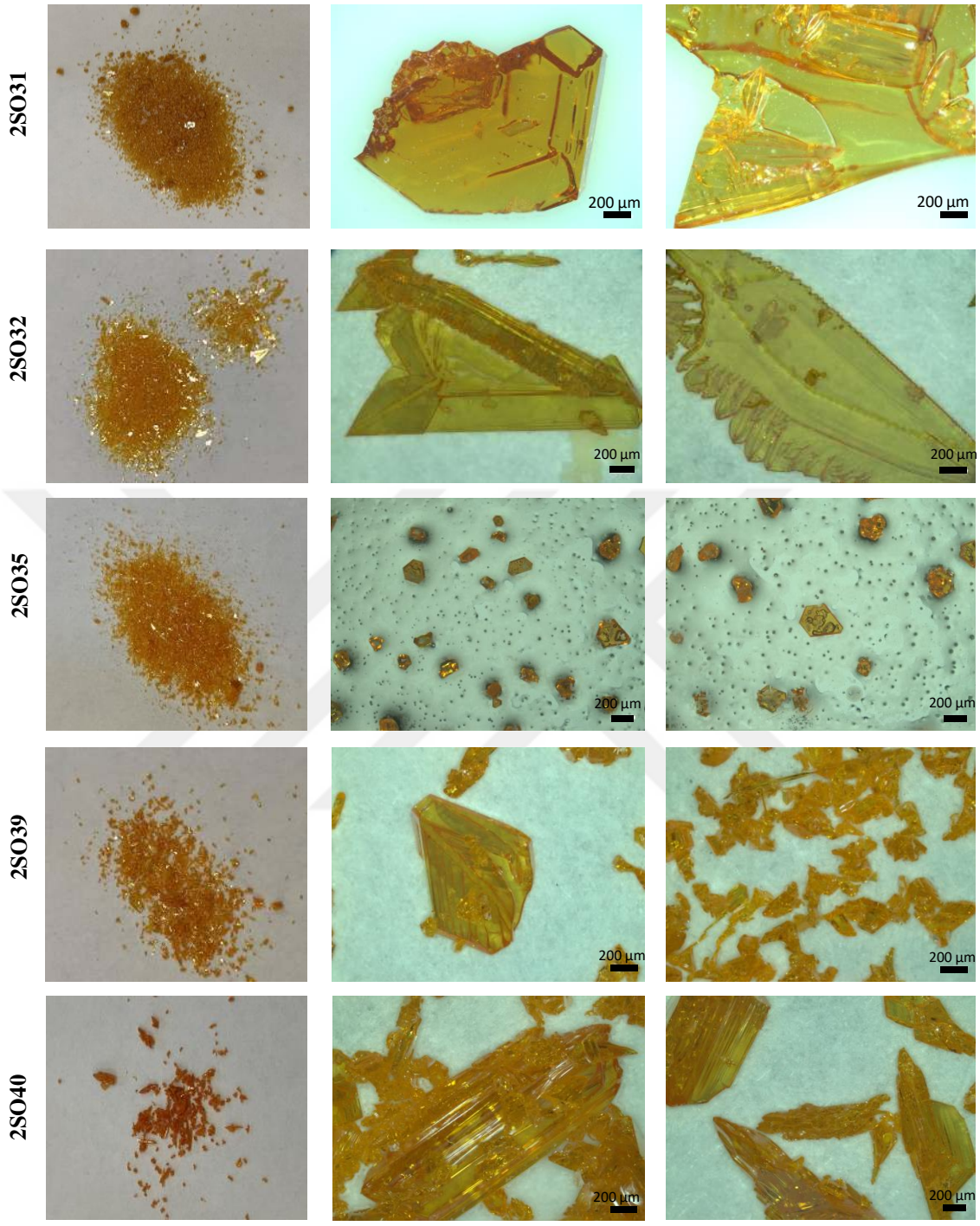


**Figure 3. 28** Photographs and optical images of representative samples synthesized by CVT method.

As can be seen from the optical microscope images given in Figure 3.28, single-crystals are formed in various directions. These single-crystals growing in various directions combine to form the bulk pieces imaged in Figure 3.28. This phenomenon can be observed by the layered structure these samples display.

According to the optical microscope images, the most uniformly grown single-crystals were observed in the 2SO35 sample. Although increasing the amount of $ZnCl_2$ used as a transport agent helps to obtain larger crystals, it prevents the more regular growth of single-crystals. For example, although each of the crystals obtained in the 2SO40 sample are approximately 1 mm in length, a layered structure is observed in all of them.

Except for the 2SO35 sample, it was observed that the grown crystals were distributed over a wide area of the quartz tube in all experiments. This situation can be attributed to not using a seed crystal, as well as the inappropriate transport parameters. On the other hand, for 2SO35, the more regular growth of the small crsytals took place in a more narrow region of the quartz tube (between the 7–7.5 cm of the quartz tube). Considering that the single-crystals in the 2SO35 sample are both quite smooth and grown in a narrow region, it can be inferred that the most suitable transport parameters are heat gradient of 200 °C and a transport agent ($ZnCl_2$) amount of 25 mg.

Considering the above-mentioned points, using a seed crystal grown in (111) direction using 25 mg $ZnCl_2$ transport agent under 200 °C heat gradient is expected to lead to larger and more regular single-crystals. The ZnSe single-crystals growing in the 2SO35 sample were mostly collected in the 7-7.5 cm region o the quartz tube, making it reasonable to position the aforementioned seed crystal at 7 cm. Two-zone furnace experiments will be carried out with seed crystal in future studies.

### *3.5.1 XRD analysis crystals growth by CVT*

XRD measurements were performed after the crystals were ground with the help of mortar in order to control the crystal growth directions and the presence of impurities. (Figure 3.29).

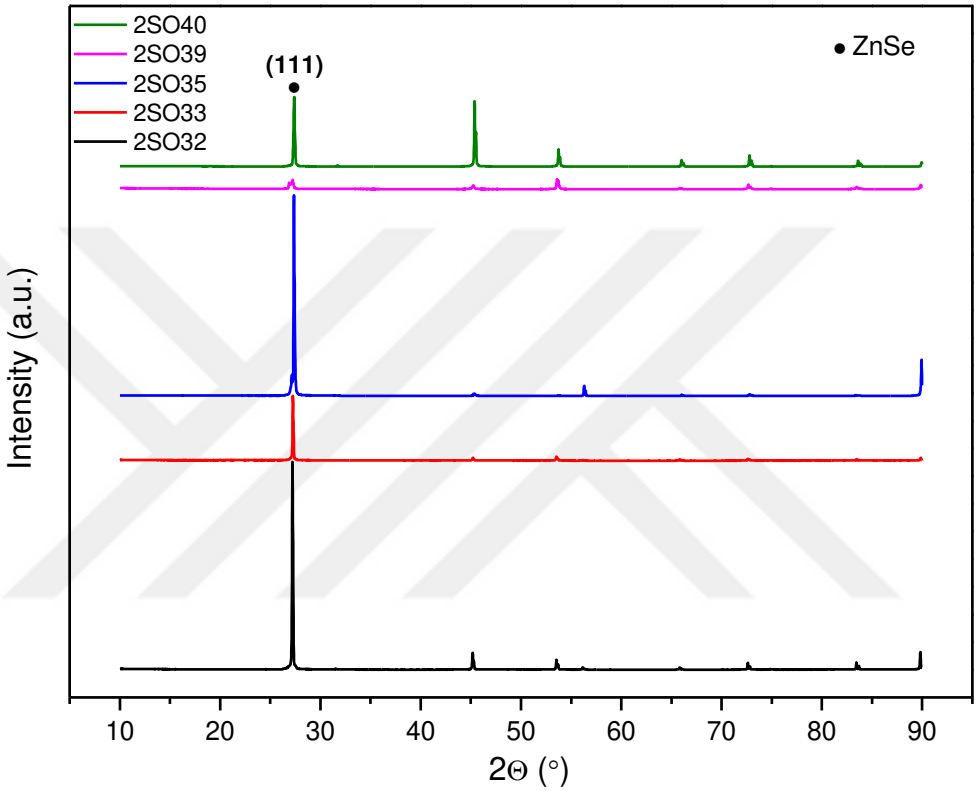


**Figure 3. 29** XRD patterns of ZnSe single-crystals.

According to the XRD data given in Figure 3.29, there is no impurity in any of the single-crystals grown by the CVT method. All peaks belong to ZnSe crystals. When the peak intensities are compared, it is seen that the single-crystals grow predominantly in the (111) direction in the 2SO32, 2SO33, and 2SO35 samples. When the peak intensities of 2SO39 and 2SO40 samples are compared, it is observed that there are single-crystals growing also in different orientations than (111). As discussed in Section 3.5.1, the crystals observed to be in a layered structure are thought to be formed by the merging of single-crystals of different orientations, which seem to cause the presence of various peaks indicating various directions. Also, in Section 3.5.1, it was mentioned that the reason for this was the increase in the amount of transport agent.

When the XRD patterns given in Figure 3.29 are examined together with Table 3.11, it is clear that the increase in the amount of transport agent encourages single-crystal growth in various directions. When the 2SO33 and 2SO39 samples, which were preapared both by using 100 mg of $ZnCl_2$, are compared, 2SO33 is growing predominantly in the (111) direction while 2SO39 grows in various direction. Furthermore 2SO39 forms larger crystals. This difference is attributed to the higher heat gradiant applied to 2SO39. It can be concluded that a higher heating gradient with a high (100 mg) amount of transport agent results in the growth in various directions and in the formation of larger crystals.

In general, to obtain crystals growing in single direction, either a high heat gradient and a low amount of transport agent (such as in 2SO35) or a low heating rate accompanied by a high amount of transport agent (such as in 2SO32) should be used. This can be confirmed by the XRD data of 2SO35 and 2SO32 (Figure 3.29).

### *3.5.2 WDXS Analyses of 2SO40*

For a more detailed composition analysis, WDXS analysis of the 2SO40 sample was performed. The reason for choosing the 2SO40 sample for WDXS analysis is that it is the sample with the highest probability of having a distorted stoichiometry. Because 2SO40 is the sample that has the largest growth rate and hosts the most crystals of different orientations. WDXS analyses are given in Figure 3.30.

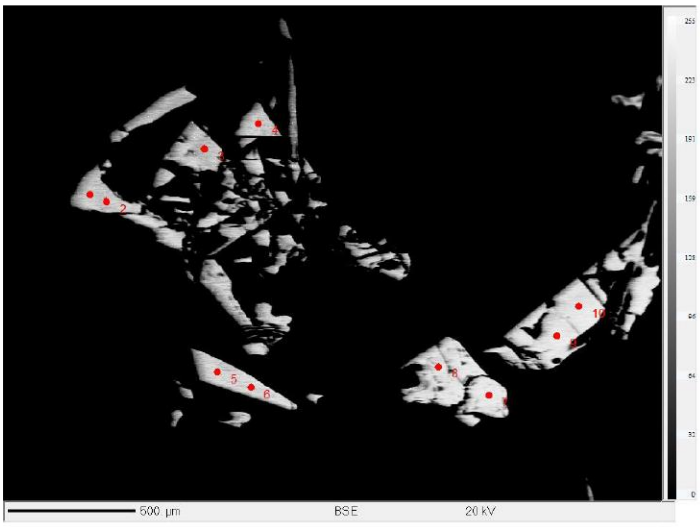


**Figure 3. 30** Different locations were WDXS analysis was performed on the sample 2SO40.

**Table 3. 12** Average composition of Zn and Se of 2SO40 obtained by WDXS analysis.

| | Norm Weight ratio (wt.%) | Atomic ratio (at.%) | Standart Deviation (wt.%) |
|---|---|---|---|
| Zn (avg.) | 45.25 | 50.00 | 0.10 |
| Se (avg.) | 54.75 | 50.00 | 0.10 |
| Total (avg.) | 100.00 | 100.00 | |

The average of the results of the measurements taken from 10 different points is given in Table 3.12. The Zn and Se stoichiometry were in a perfect ratio of 1:1 (Zn:Se).

### *3.5.3 SEM/EDX Measurements*

SEM images were taken in order to examine the effect of the amount of $ZnCl_2$ used in the 2SO31, 2SO32 and 2SO33 samples with a heat gradient of 100 °C on the crystal sizes (Figure 3.31).

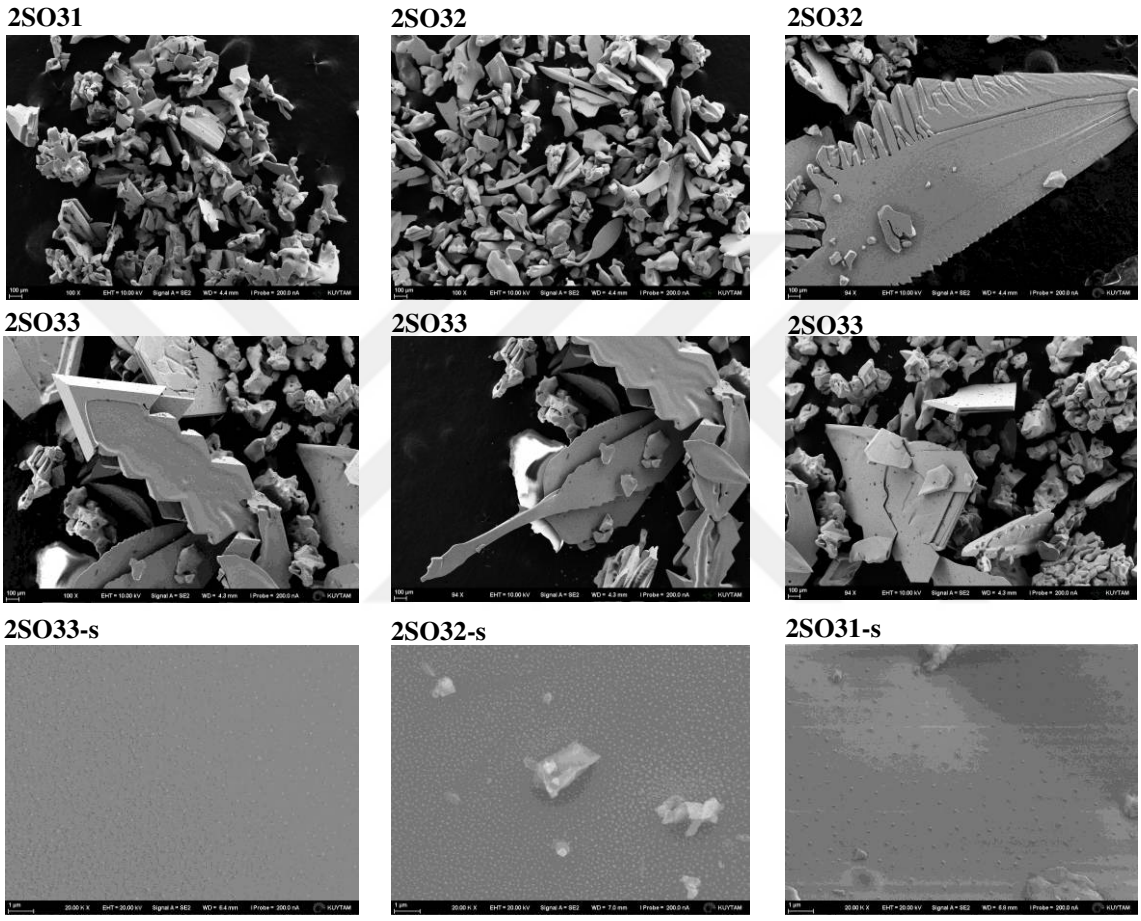


**Figure 3. 31** SEM images of representative samples synthesized by CVT method.

According to Figure 3.31, ZnSe crystals grown in the presence of a heat gradient of 100 °C can be divided into two main groups. The first of these is the crystals that are in the size of 100–200 microns and do not grow further, and the second is the crystals that grow up to 1 mm. The increase in the amount of $ZnCl_2$ does not affect the size of the crystals in the first group. However, the number of crystals around 1 mm increased in direct proportion to the amount of transport agent. For example, while more than one crystal of 1 mm in size was observed in the 2SO33 sample, for 2SO32 and 2SO31 almost all crystals were below 1 mm. It is obvious that increasing the amount of

transport agent when the heat gradient is at 100 °C encourages the growth of larger crystals.

2SO31-s, 2SO32-s, and 2SO33-s images are the images taken from the surface of the large crystals contained in the aforementioned samples. Spherical structures were observed on the surface of all crystals, and it was determined that their number increased in direct proportion to the increasing amount of $ZnCl_2$. The diameters of these spherical structures are around 100 nm and they show a fairly homogeneous distribution. Although the exact cause of this formation has not been determined, it has been found that it is proportional to the amount of transport agent and does not disturb the stoichiometry according to EDX-mapping measurements.

EDX measurements were performed to support the findings of WDXS. 2SO40 crystals, which were determined to be in perfect stoichiometry according to WDXS measurements, were measured by EDX from different locations of the crystal (Figure 3.32).

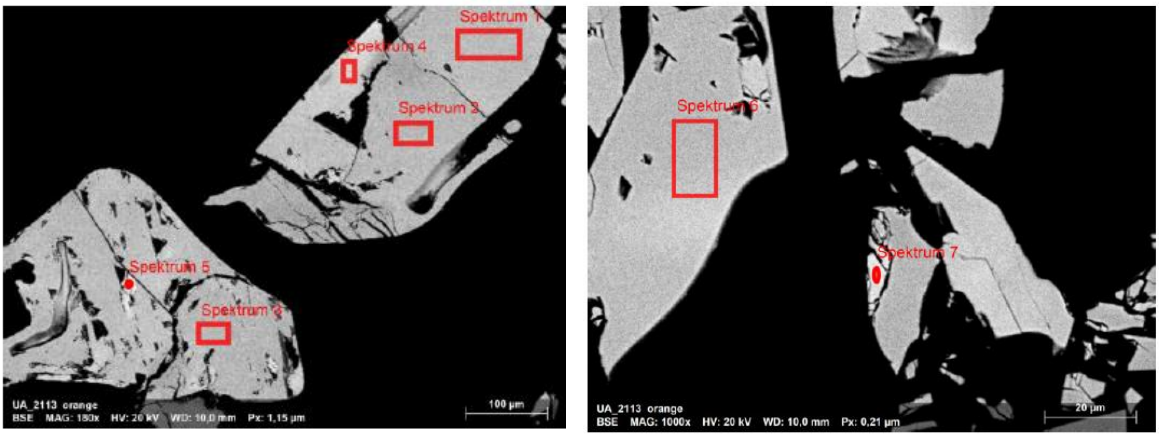


**Figure 3. 32** EDX regions for the crystals collected from 2SO40.

**Table 3. 13** Atomic concentrations of various points presented in figure 3.32 of 2SO40.

| Spectrum | C (at.%) | O (at.%) | Zn (at.%) | Se (at.%) |
|---|---|---|---|---|
| Spectrum 1 | 0.00 | 0.00 | 50.47 | 49.53 |
| Spectrum 2 | 0.00 | 0.00 | 50.18 | 49.82 |
| Spectrum 3 | 0.00 | 0.00 | 50.52 | 49.48 |
| Spectrum 4 | 0.00 | 0.00 | 49.62 | 50.38 |
| Spectrum 5 | 0.00 | 0.00 | 49.79 | 50.21 |
| Spectrum 6 | 0.00 | 0.00 | 50.08 | 49.92 |
| Spectrum 7 | 0.00 | 0.00 | 51.04 | 48.96 |
| Mean | 0.00 | 0.00 | 50.24 | 49.75 |

According to the EDX results from 7 different regions, the 2SO40 sample does not contain C or O. The average of the atomic ratios of Zn and Se atoms for 7 different regions is very close to the 1:1 stoichiometry. WDXS, XRD, and EDX results show that the crystals grown by the CVT method is very succesfull in obaining ZnSe crystals in 1:1 Zn:Se stocihiometry without the presence of any impurities.

# Chapter 4:

# CONCLUSION

Polycrystalline ZnSe powder was synthesized in high purity by co-precipitation, solid-state, and ball milling methods. These ZnSe samples were pressed into pellets via sintering with SPS under different conditions. Microstructure and composition analyses of the as-synthesized ZnSe materials were performed. According to these characterizations, it was determined that the materials synthesized by the ball milling method contained excess Zn and Se. The mentioned elemental impurities were removed by applying heat treatment at 750 °C. This purification method was applied to all ZnSe powders to be sintered with SPS because it enlarges the grains and purifies the material.

It was determined that the crystallite sizes of the samples synthesized by solid-state method were larger than those synthesized by ball milling. The heterogeneous structure that could be observed in the synthesized bulk ZnSe material, which was dependent on the pre-synthesis process, was removed by optimizing the pre-synthesis conditions, such as increasing the hand-grinding before solid-state synthesis. Among the polycrystalline ZnSe samples obtained by the solid-state method, the highest transmission value was observed in the 2SO24c-aSPS sample as a result of sintering with SPS, and its transmittance value is around 50% between 5-18 μm wavelengths. To the best of our knowledge, transparent ZnSe has not been obtained before by sintering polycrystalline ZnSe material, synthesized using the solid-state method followed by SPS. In this sense, although the optical properties of the 2SO24c-aSPS sample still need to be improved for laser applications, it makes an essential contribution to the literature in terms of being a transparent ZnSe ceramic synthesized by the solid-state method.

After sintering polycrystalline ZnSe powder synthesized by co-precipitation method and sintered by SPS, the expected transmittance values could not be reached. Although the 2SO11-ac sample is pure according to the XRD results, it has approximately the same crystallite dimensions (12 nm) as the powder ZnSe samples synthesized by ball milling, which is among the reasons why the sintered material does not have good optical properties. In addition, the fracture SEM images of SO11-aSPS sample obtained after SPS show that the grains do not fuse sufficiently and the grain

size is around 5-6 μm on average. These grain sizes are well below the required size (60-70 μm). Considering all these, changing the co-precipitation synthesis parameters to obtain powder ZnSe with larger crystal sizes and applying heat treatment to the SO11-ac sample to be sintered with SPS before SPS to enlarge its grains are among the plans for future studies.

According to the results obtained in single-crystal growth experiments, it is clearly seen that $ZnCl_2$ is a promising transport agent in growing single crystalline ZnSe. Accordingly, the grown crystals have a very precise Zn:Se stoichiometry of 1:1 according to XRD, EDX, and WDXS results and do not contain any impurities. In addition, the XRD patterns of 2SO32, 2SO33, and 2SO35 samples confirm that the crystals grow more in the (111) direction. It has been observed in the experiments that the grown crystals can be in a layered structure and in some cases contain different orientations. The common feature of the crystals in which different orientations emerge is to have a high growth rate. Considering that the two parameters that determine the growth rate are the amount of the transport agent and the size of the heat gradient, this situation can be controlled by optimizing the synthesis conditions. In the experiments, it was observed that the most smoothly growing single-crystals were the 2SO35 sample made with 25 mg $ZnCl_2$ under a 200 °C heat gradient. In future studies, we plan to place a seed crystal in the region where single crystals in this 2SO35 sample grow.

# BIBLIOGRAPHY

[1] S. Bandyopadhyay, R. Halder, Transparent ceramics, Science and culture, 81 (2015).

[2] M. Fox, Optical properties of solids, American Association of Physics Teachers, 2002.

[3] R.L. Coble, Transparent alumina and method of preparation, Google Patents, 1962.

[4] R. Coble, Sintering alumina: effect of atmospheres, Journal of the American Ceramic Society, 45 (1962) 123-127.

[5] R. Lefever, J. Matsko, Transparent yttrium oxide ceramics, Materials Research Bulletin, 2 (1967) 865-869.

[6] R. Bratton, Translucent sintered $MgAl_2O_4$, Journal of the American Ceramic Society, 57 (1974) 283-286.

[7] G. Haertling, Improved hot-pressed electrooptic ceramics in the (Pb, La)(Zr, Ti) O3 system, Journal of the American Ceramic Society, 54 (1971) 303-309.

[8] H. Van Dijk, Translucent $Y_3Al_5O_{12}$ ceramics, Materials research bulletin, 19 (1984) 1669-1674.

[9] S. Hatch, W. Parsons, R. Weagley, Hot-pressed polycrystalline $CaF_2$: $Dy^{2+}$ laser, Applied Physics Letters, 5 (1964) 153-154.

[10] N. Kuramoto, H. Taniguchi, Transparent AIN ceramics, Journal of materials science letters, 3 (1984) 471-474.

[11] H.J. McQueen, G. Kuczynski, Sintering of zinc sulfide, Journal of the American Ceramic Society, 45 (1962) 343-346.

[12] W. Parsons, Optical materials research, Applied optics, 11 (1972) 43-49.

[13] A.K. Abbas, K. Heimann, V. Blazek, T. Orlikowsky, S. Leonhardt, Neonatal infrared thermography imaging: Analysis of heat flux during different clinical scenarios, Infrared Physics & Technology, 55 (2012) 538–548.

[14] I. Rosenthal, Electromagnetic radiations in food science, (2012).

[15] B.B. Lahiri, S. Bagavathiappan, T. Jayakumar, J. Philip, Medical applications of infrared thermography: A review, Infrared Physics & Technology, 55 (2012) 221-235.

[16] M. Sillero-Quintana, T. Fernández-Jaén, I. Fernández-Cuevas, P.M. Gómez-Carmona, J. Arnaiz-Lastras, M.-D. Pérez, P. Guillén, Infrared thermography as a

support tool for screening and early diagnosis in emergencies, Journal of Medical Imaging and Health Informatics, 5 (2015) 1223-1228.

[17] J.R. Howell, M.P. Mengüç, K. Daun, R. Siegel, Thermal radiation heat transfer, CRC press2020.

[18] C. Brierley, C. Beck, G. Kennedy, J. Metcalfe, D. Wheatley, The potential of CVD diamond as a replacement to ZnSe in $CO_2$ laser optics, Diamond and related materials, 8 (1999) 1759-1764.

[19] K. Ebata, M. Shiozaki, T. Okada, K. Fuse, H. Nanba, Characteristics of ZnSe aspheric beam shaper for $CO_2$ laser, Laser Beam Shaping II, International Society for Optics and Photonics, 2001, pp. 125-134.

[20] N.J. Mohammed, Effect of laser fluence on structural transformations and photoluminescence quenching of Zinc Selenide nanoparticles thin films, Al-Mustansiriyah Journal of Science, 29 (2019) 122-127.

[21] Y. Leung, W.C. Choy, I. Markov, G. Pang, H. Ong, T. Yuk, Synthesis of wurtzite ZnSe nanorings by thermal evaporation, Applied physics letters, 88 (2006) 183110.

[22] C. Shan, Z. Liu, X. Zhang, C. Wong, S. Hark, Wurtzite ZnSe nanowires: growth, photoluminescence, and single-wire Raman properties, Nanotechnology, 17 (2006) 5561.

[23] L. Jin, W.C. Choy, Y.P. Leung, T.I. Yuk, H.C. Ong, J.-b. Wang, Synthesis and analysis of abnormal wurtzite ZnSe nanowheels, Journal of Applied Physics, 102 (2007) 044302.

[24] E. Gavrushchuk, Polycrystalline zinc selenide for IR optical applications, Inorganic Materials, 39 (2003) 883-899.

[25] A.A.e. Voronov, V.I. Kozlovskii, Y.V. Korostelin, A.I. Landman, Y.P. Podmar'Kov, Y.K. Skasyrskii, M.P. Frolov, A continuous-wave $Fe^{2+}$: ZnSe laser, Quantum Electronics, 38 (2008) 1113.

[26] N. Il'ichev, S. Kazantsev, V. Kalinushkin, K. Firsov, $Fe^{2+}$: ZnSe laser pumped by a nonchain electric-discharge HF laser at room temperature, Quantum Electronics, 44 (2014) 141-144.

[27] A. Podlipensky, V. Shcherbitsky, N. Kuleshov, V. Levchenko, V. Yakimovich, M. Mond, E. Heumann, G. Huber, H. Kretschmann, S. Kück, Efficient laser operation and continuous-wave diode pumping of $Cr^{2+}$: ZnSe single crystals, Applied Physics B, 72 (2001) 253-255.

[28] K. Firsov, E. Gavrishchuk, V. Ikonnikov, S.Y. Kazantsev, I. Kononov, S. Rodin, D. Savin, A. Sirotkin, N. Timofeeva, CVD-grown $Fe^{2+}$: ZnSe polycrystals for laser applications, Laser Physics Letters, 14 (2017) 055805.

[29] H. Li, W. Jie, Growth and characterizations of bulk ZnSe single crystal by chemical vapor transport, Journal of Crystal Growth, 257 (2003) 110-115.

[30] J. Wang, A. Omino, M. Isshiki, Bridgman growth of twin-free ZnSe single crystals, Materials Science and Engineering: B, 83 (2001) 185-191.

[31] C. Liu, T. Wang, G. Zha, Z. Gu, W. Jie, ZnCl2-assisted Synthesis of ZnSe Polycrystal, Journal of Materials Science & Technology, 28 (2012) 373-378.

[32] A.J. Ahamed, K. Ramar, P.V. Kumar, Synthesis and characterization of ZnSe nanoparticles by Co-precipitation method, Journal of nanoscience and technology, (2016) 148-150.

[33] S. Yu, Y. Wu, Synthesis of Fe: ZnSe nanopowders via the co-precipitation method for processing transparent ceramics, Journal of the American Ceramic Society, 102 (2019) 7089-7097.

[34] M. Achimovičová, P. Baláž, T. Ohtani, N. Kostova, G. Tyuliev, A. Feldhoff, V. Šepelák, Characterization of mechanochemically synthesized ZnSe in a laboratory and an industrial mill, Solid State Ionics, 192 (2011) 632-637.

[35] R. Avetisov, S. Balabanov, K. Firsov, E. Gavrishchuk, A. Gladilin, V. Ikonnikov, V. Kalinushkin, S.Y. Kazantsev, I. Kononov, M. Zykova, Hot-pressed production and laser properties of ZnSe: $Fe^{2+}$, Journal of Crystal Growth, 491 (2018) 36-41.

[36] N. Wei, L. Jiang, D. Li, H. Yang, X. Zhang, Z. Tian, L. Guo, X. Liu, Z. Song, J. Yang, A hot isostatic pressing strategy for improving the optical transmission of polycrystalline cvd znse, Applied Physics A, 125 (2019) 1-6.

[37] S. Yu, D. Carloni, Y. Wu, Microstructure development and optical properties of Fe: ZnSe transparent ceramics sintered by spark plasma sintering, Journal of the American Ceramic Society, 103 (2020) 4159-4166.

[38] J.-H. Park, T. Sudarshan, Chemical vapor deposition, ASM international2001.

[39] A. Reina, X. Jia, J. Ho, D. Nezich, H. Son, V. Bulovic, M.S. Dresselhaus, J. Kong, Large area, few-layer graphene films on arbitrary substrates by chemical vapor deposition, Nano letters, 9 (2009) 30-35.

[40] M. Kumar, Y. Ando, Chemical vapor deposition of carbon nanotubes: a review on growth mechanism and mass production, Journal of nanoscience and nanotechnology, 10 (2010) 3739-3758.

[41] J. Zhu, Y. Koltypin, A. Gedanken, General sonochemical method for the preparation of nanophasic selenides: synthesis of ZnSe nanoparticles, Chemistry of Materials, 12 (2000) 73-78.

[42] A. Sanchez-Martinez, J. Ortiz-Beas, A. Huerta-Flores, E.R. López-Mena, J. Pérez-Álvarez, O. Ceballos-Sanchez, ZnSe nanoparticles prepared by coprecipitation method for photocatalytic applications, Materials Letters, 282 (2021) 128702.

[43] F. Mollaamin, S. Gharibe, M. Monajjemi, Synthesis of various nano and micro ZnSe morphologies by using hydrothermal method, International Journal of Physical Sciences, 6 (2011) 1496-1500.

[44] A. Bertrand, J. Carreaud, G. Delaizir, J.R. Duclère, M. Colas, J. Cornette, M. Vandenhende, V. Couderc, P. Thomas, A comprehensive study of the carbon contamination in tellurite glasses and glass-ceramics sintered by spark plasma sintering (SPS), Journal of the American Ceramic Society, 97 (2014) 163-172.

[45] A. Miriyev, A. Stern, E. Tuval, S. Kalabukhov, Z. Hooper, N. Frage, Titanium to steel joining by spark plasma sintering (SPS) technology, Journal of Materials Processing Technology, 213 (2013) 161-166.

[46] K. Morita, B.-N. Kim, H. Yoshida, K. Hiraga, Y. Sakka, Distribution of carbon contamination in oxide ceramics occurring during spark-plasma-sintering (SPS) processing: II-Effect of SPS and loading temperatures, Journal of the European Ceramic Society, 38 (2018) 2596-2604.

[47] K. Morita, B.-N. Kim, H. Yoshida, K. Hiraga, Y. Sakka, Assessment of carbon contamination in $MgAl_2O_4$ spinel during spark-plasma-sintering (SPS) processing, Journal of the Ceramic Society of Japan, 123 (2015) 983-988.

[48] N. Kwak, G. Min, Y. Oh, D.-W. Suh, H.C. Kim, S.-g. Kang, H.N. Han, Tantalum and molybdenum barriers to prevent carbon diffusion in spark plasma sintered tungsten, Scripta Materialia, 196 (2021) 113759.

[49] L. Yu, K. Khor, H. Li, K. Pay, T. Yip, P. Cheang, Restoring WC in plasma sprayed WC–Co coatings through spark plasma sintering (SPS), Surface and Coatings Technology, 182 (2004) 308-317.

[50] A. Gallian, V. Fedorov, S.B. Mirov, V. Badikov, S. Galkin, E. Voronkin, A. Lalayants, Hot-pressed ceramic Cr $^{2+}$: ZnSe gain-switched laser, Optics express, 14 (2006) 11694-11701.

[51] Y. Luo, M. Yin, L. Chen, B. Kang, S. Yu, Hot-pressed $Fe^{2+}$: ZnSe transparent ceramics with different doping concentrations, Ceramics International, (2021).

[52] J.W. Evans, R.W. Stites, T.R. Harris, Increasing the performance of an Fe: ZnSe laser using a hot isostatic press, Optical Materials Express, 7 (2017) 4296-4303.

[53] W.G. Lee, Y.K. Kim, J.K. Kim, N. Starzhinskiy, V. Ryzhikov, B. Grinyov, Growth and properties of new ZnSe(Al,O,Te) semiconductor scintillator, Radiation Measurements, 43 (2008) 502-505.

[54] H. Yoshida, T. Fujii, A. Kamata, Y. Nakata, Undoped ZnSe single crystal growth by the vertical Bridgman method, Journal of Crystal Growth, 117 (1992) 75-79.

[55] J.F. Wang, A. Omino, M. Isshiki, Bridgman growth of twin-free ZnSe single crystals, Materials Science and Engineering: B, 83 (2001) 185-191.

[56] H.J. Scheel, P. Capper, P. Rudolph, Crystal growth technology: semiconductors and dielectrics, John Wiley & Sons2011.

[57] C.S. Fang, Q.T. Gu, J.Q. Wei, Q.W. Pan, W. Shi, J.Y. Wang, Growth of ZnSe single crystals, Journal of Crystal Growth, 209 (2000) 542-546.

[58] H. Li, W. Jie, Growth and characterizations of bulk ZnSe single crystal by chemical vapor transport, Journal of Crystal Growth, 257 (2003) 110-115.

[59] O. Senthil Kumar, S. Soundeswaran, R. Dhanasekaran, Thermodynamic Calculations and Growth of ZnSe Single Crystals by Chemical Vapor Transport Technique, Crystal Growth & Design, 2 (2002) 585-589.

[60] S. Fujiwara, Y. Namikawa, T. Nakamura, M. Tatsumi, Growth of large ZnSe single crystal by R-CVT method, Journal of Crystal Growth, 275 (2005) e415-e419.

[61] S. Fujiwara, Y. Namikawa, M. Irikura, K. Matsumoto, T. Kotani, T. Nakamura, Growth of dislocation-free ZnSe single crystal by CVT method, Journal of Crystal Growth, 219 (2000) 353-360.

[62] S. Fujiwara, Y. Namikawa, T. Kotani, Growth of 1″ diameter ZnSe single crystal by the rotational chemical vapor transport method, Journal of Crystal Growth, 205 (1999) 43-49.

[63] K. Matsumoto, K. Konemura, G. Shimaoka, Crystal growth of ZnO by vapor transport in a closed tube using Zn and $ZnCl_2$ as transport agents, Journal of crystal growth, 71 (1985) 99-103.

[64] A. Muti, M. Tonelli, V. Petrov, A. Sennaroglu, Continuous-wave mid-infrared laser operation of $Tm^{3+}$: $KY_3F_{10}$ at 2.3 μm, Optics letters, 44 (2019) 3242-3245.

[65] T.H. Maiman, Stimulated Optical Radiation in Ruby, Nature, 187 (1960) 493-494.

[66] T. Sasano, I. Nakajima, N. Shoji, S. Kuriwada, D. Sanjo, H. Ogino, T. Miyahara, Possible application of transmitted laser light for the assessment of human pulpal vitality, Endodontics & dental traumatology, 13 (1997) 88-91.

[67] A. Einstein, Zur Quantentheorie der Strahlung, Physikalische Zeitschrift, 18 121-128.

[68] M. Chu, Y. Shao, J. Peng, X. Dai, H. Li, Q. Wu, D. Shi, Near-infrared laser light mediated cancer therapy by photothermal effect of $Fe_3O_4$ magnetic nanoparticles, Biomaterials, 34 (2013) 4078-4088.

[69] K. Scholle, S. Lamrini, P. Koopmann, P. Fuhrberg, 2 μm laser sources and their possible applications, Frontiers in guided wave optics and optoelectronics, IntechOpen2010.

[70] T. Bilici, H.Ö. Tabakoglu, N. Topaloglu, H. Kalaycioglu, A. Kurt, A. Sennaroglu, M. Gülsoy, Modulated and continuous-wave operations of low-power thulium (Tm: YAP) laser in tissue welding, Journal of biomedical optics, 15 (2010) 038001.

[71] D. Huang, E.A. Swanson, C.P. Lin, J.S. Schuman, W.G. Stinson, W. Chang, M.R. Hee, T. Flotte, K. Gregory, C.A. Puliafito, Optical coherence tomography, science, 254 (1991) 1178-1181.

[72] U. Demirbas, A. Sennaroglu, F.X. Kärtner, J.G. Fujimoto, Highly efficient, low-cost femtosecond $Cr^{3+}$: LiCAF laser pumped by single-mode diodes, Optics letters, 33 (2008) 590-592.

[73] H. Kukimoto, S. Shionoya, T. Koda, R. Hioki, Infrared absorption due to donor states in ZnS crystals, Journal of Physics and Chemistry of Solids, 29 (1968) 935-944.

[74] M. Kautzky, M. Susani, M. Steurer, P. Schenk, Soft-tissue effects of the holmium: YAG laser: An ultrastructural study on oral mucosa, Lasers in Surgery and Medicine: The Official Journal of the American Society for Laser Medicine and Surgery, 20 (1997) 265-271.

[75] B.H. Hendler, J. Gateno, P. Mooar, H.H. Sherk, Holmium: YAG laser arthroscopy of the temporomandibular joint, Journal of oral and maxillofacial surgery, 50 (1992) 931-934.

[76] H. TOKONABE, R. Kouji, H. WATANABE, Y. NAKAMURA, K. MATSUMOTO, Morphological changes of human teeth with Er: YAG laser irradiation, Journal of clinical laser medicine & surgery, 17 (1999) 7-12.

[77] G. van As, Erbium lasers in dentistry, Dental Clinics, 48 (2004) 1017-1059.

[78] U. Keller, R. Hibst, Effects of Er: YAG laser in caries treatment: a clinical pilot study, Lasers in Surgery and Medicine: The Official Journal of the American Society for Laser Medicine and Surgery, 20 (1997) 32-38.

[79] A. Martínez-Insua, L. da Silva Dominguez, F.G. Rivera, U.A. Santana-Penín, Differences in bonding to acid-etched or Er: YAG-laser–treated enamel and dentin surfaces, The Journal of prosthetic dentistry, 84 (2000) 280-288.

[80] K.U. Lewandrowski, C. Lorente, K.T. Schomacker, T.J. Fiotte, J.W. Wilkes, T.F. Deutsch, Use of the Er: YAG laser for improved plating in maxillofacial surgery: comparison of bone healing in laser and drill osteotomies, Lasers in Surgery and Medicine: The Official Journal of the American Society for Laser Medicine and Surgery, 19 (1996) 40-45.

[81] P. Budni, L. Pomeranz, M. Lemons, C. Miller, J. Mosto, E. Chicklis, Efficient mid-infrared laser using 1.9-μm-pumped Ho: YAG and ZnGeP 2 optical parametric oscillators, JOSA B, 17 (2000) 723-728.

[82] T.M. Taczak, D.K. Killinger, Development of a tunable, narrow-linewidth, cw 2.066-μm Ho: YLF laser for remote sensing of atmospheric $CO_2$ and $H_2O$, Applied optics, 37 (1998) 8460-8476.

[83] R. Targ, B.C. Steakley, J.G. Hawley, L.L. Ames, P. Forney, D. Swanson, R. Stone, R.G. Otto, V. Zarifis, P. Brockman, Coherent lidar airborne wind sensor II: flight-test results at 2 and 10 μm, Applied optics, 35 (1996) 7117-7127.

[84] A. Gordon, F.X. Kärtner, Scaling of keV HHG photon yield with drive wavelength, Optics Express, 13 (2005) 2941-2947.

[85] A. Sennaroglu, Photonics and laser engineering : principles, devices, and applications, McGraw-Hill, New York, 2010.

[86] M. Binnewies, R. Glaum, M. Schmidt, P. Schmidt, Chemical vapor transport reactions, de Gruyter2012.

[87] Y. Waseda, E. Matsubara, K. Shinoda, X-ray diffraction crystallography: introduction, examples and solved problems, Springer Science & Business Media2011.

[88] M. Che, J.C. Védrine, Characterization of solid materials and heterogeneous catalysts: from structure to surface reactivity, John Wiley & Sons2012.

[89] T. Theophile, Infrared spectroscopy: Materials science, engineering and technology, BoD–Books on Demand2012.

[90] J.F. Watts, J. Wolstenholme, An introduction to surface analysis by XPS and AES, John Wiley & Sons2019.

[91] S. Wei, L. Zhang, H. Yang, T. Zhou, C. Wong, Q. Zhang, H. Chen, Preliminary study of 3D ball-milled powder processing and SPS-accelerated densification of ZnSe ceramics, Optical Materials Express, 7 (2017) 1131-1140.

[92] R. Castro, K. Van Benthem, Sintering: mechanisms of convention nanodensification and field assisted processes, Springer Science & Business Media2012.

[93] V. Skorokhod, Rapid rate sintering of dispersed systems: theory, processing, and problems, Powder Metallurgy and Metal Ceramics, 38 (1999) 350-357.

[94] B.T. Huy, M.-H. Seo, A.P. Kumar, H. Jeong, Y.-I. Lee, Synthesis and photoluminescence of Cr-, Ni-, Co-, and Ti-doped ZnSe nanoparticles, Journal of alloys and compounds, 588 (2014) 127-132.

[95] K. Karki, S. Yu, V. Fedorov, Y. Wu, S. Mirov, Fe: ZnSe hot-pressed ceramic laser, 2020 Conference on Lasers and Electro-Optics (CLEO), IEEE, 2020, pp. 1-2.

[96] Z. Li, H. Chen, W. Liu, Full-spectrum photocatalytic activity of ZnO/CuO/$ZnFe_2O_4$ nanocomposite as a PhotoFenton-like catalyst, Catalysts, 8 (2018) 557.

[97] M.A. Bhide, C.J. Carmalt, C.E. Knapp, A novel precursor towards buffer layer materials: the first solution based CVD of zinc oxysulfide, Journal of Materials Chemistry C, 8 (2020) 5501-5508.

[98] A. Chaparro, C. Maffiotte, M. Gutierrez, J. Herrero, Morphological and compositional study of CBD-ZnSe thin films by microscopy techniques and angle resolved XPS, Thin solid films, 358 (2000) 22-29.

[99] Z. Deng, F.L. Lie, S. Shen, I. Ghosh, M. Mansuripur, A.J. Muscat, Water-based route to ligand-selective synthesis of ZnSe and Cd-doped ZnSe quantum dots with tunable ultraviolet A to blue photoluminescence, Langmuir, 25 (2009) 434-442.

[100] P.T. Hsieh, Y.C. Chen, K.S. Kao, C.M. Wang, Luminescence mechanism of ZnO thin film investigated by XPS measurement, Applied Physics A, 90 (2007) 317-321.

[101] J. Zhang, L. Fan, Y. Zhu, Y. Xu, J. Liang, D. Wei, Y. Qian, Selenium/interconnected porous hollow carbon bubbles composites as the cathodes of Li–Se batteries with high performance, Nanoscale, 6 (2014) 12952-12957.